

**SUBSURFACE AND TRANSCUTANEOUS RAMAN  
SPECTROSCOPY, IMAGING, AND TOMOGRAPHY**

by

**Matthew V. Schulmerich**

A dissertation submitted in partial fulfillment  
of the requirements for the degree of  
Doctor of Philosophy  
(Chemistry)  
in The University of Michigan  
2008

Doctoral Committee:

Professor Michael D. Morris, Chair  
Professor Steven A. Goldstein  
Professor Robert T. Kennedy  
Assistant Professor Kevin J. Kubarych

© Matthew V. Schulmerich

---

All rights reserved  
2008

To my wife, Michelle

Happy Retirement!

## ACKNOWLEDGMENTS

This work was the result of contributions from several excellent scientists. Among them, I would like to thank my advisor Michael Morris. Professor Morris's enthusiasm, encouragement, and guidance has made my graduate experience a great one. As a mentor, he showed incredible patience, foresight, and optimism. His quick witted sense of humor and laid-back manner made each day enjoyable. I feel very fortunate to have been a part of his lab and am truly grateful for the experience.

I would also like to thank my committee members and Professor Theodore Goodson for suggestions, advice, and contributions to this work. Thank you to the members of the Morris lab who have been invaluable throughout my graduate career, many of whom served as co-authors on the work presented in this dissertation. I owe a special thank you to Bill Finney and Kurt Golcuk who were among the first to introduce me to Raman spectroscopy and spectral data processing. Thank you to the members of the Goldstein lab, especially Tom Vanasse and Jaclynn Kreider, and the members of Brian Pogue's lab, especially Subhadra Srinivasan for their collaboration and the extremely useful discussions.

I am grateful to the members of the machine shop and electrical shop for their expertise and assistance in building instrumentation. Finally, I would like to thank the Chemistry Department along with Margaret and Herman Sokol for financial support.

## TABLE OF CONTENTS

<b>DEDICATION.....</b>	<b>ii</b>
<b>ACKNOWLEDGMENTS .....</b>	<b>iii</b>
<b>LIST OF FIGURES .....</b>	<b>vii</b>
<b>LIST OF TABLES .....</b>	<b>xiv</b>
<b>LIST OF APPENDICES .....</b>	<b>xv</b>
<b>ABSTRACT.....</b>	<b>xvi</b>

### CHAPTER

<b>I.</b>	<b>INTRODUCTION TO RAMAN SPECTROSCOPY THROUGH LIGHT SCATTERING MATERIALS WITH BONE AS A TARGET .....</b>	<b>1</b>
	Introduction.....	1
	Light Scattering.....	2
	Diagnostic Window .....	5
	Optical Clearing of Tissue .....	6
	Transcutaneous Raman Measurements.....	7
	Data Analysis .....	8
	Applications to Bone.....	9
	References.....	12
<b>II.</b>	<b>SUBSURFACE RAMAN SPECTROSCOPY AND MAPPING USING A GLOBALLY ILLUMINATED NON-CONFOCAL FIBER OPTIC PROBE IN THE PRESENCE OF RAMAN PHOTON MIGRATION .....</b>	<b>16</b>
	Introduction.....	16
	Experimental .....	19
	Data Treatment.....	21
	Results and Discussion .....	22
	Conclusions.....	25
	References.....	35

<b>III.</b>	<b>TRANSCUTANEOUS RAMAN SPECTROSCOPY OF BONE TISSUE USING A NON-CONFOCAL FIBER OPTIC ARRAY PROBE .....</b>	<b>38</b>
	Introduction.....	38
	Experimental.....	39
	Data Analysis.....	41
	Results and Discussion .....	41
	Conclusions.....	43
	References.....	49
<b>IV.</b>	<b>TRANSCUTANEOUS RAMAN SPECTROSCOPY OF BONE: GLOBAL SAMPLING VS. RING/DISK FIBER OPTIC PROBES .....</b>	<b>52</b>
	Introduction.....	52
	Preliminary measurements using the Ring/disk probe .....	54
	Experimental Method and Data Treatment.....	57
	Results and Discussion .....	59
	Conclusions.....	61
	References.....	71
<b>V.</b>	<b>SUBSURFACE AND TRANSCUTANEOUS RAMAN SPECTROSCOPY AND MAPPING USING CONCENTRIC ILLUMINATION RINGS AND COLLECTION WITH A CIRCULAR FIBER OPTIC ARRAY .....</b>	<b>74</b>
	Introduction.....	74
	Experimental.....	78
	Data Treatment.....	81
	Results and Discussion .....	82
	Conclusions.....	87
	References.....	100
<b>VI.</b>	<b>OPTICAL CLEARING IN TRANSCUTANEOUS RAMAN SPECTROSCOPY OF MURINE CORTICAL BONE TISSUE .....</b>	<b>104</b>
	Introduction.....	104
	Materials and Methods.....	106
	Results and Discussion .....	111
	Conclusions.....	114
	References.....	122
<b>VII.</b>	<b>TRANSCUTANEOUS RAMAN SPECTROSCOPY OF MURINE BONE <i>IN VIVO</i> .....</b>	<b>127</b>
	Introduction.....	127
	Experimental.....	128

Data Treatment.....	131
Results and Discussion .....	135
Conclusions.....	140
References.....	151
<b>VIII. RAMAN TOMOGRAPHY IN TISSUE PHANTOMS</b>	
<b>AND CANINE TISSUE.....</b>	<b>153</b>
Introduction.....	153
Materials and Methods.....	155
Raman probes, materials and experimental methods .....	155
Tissue phantom .....	157
Canine limb.....	158
Spectral data reduction methodology.....	159
Raman tomographic reconstruction .....	161
Tomographic reconstruction using spatial priors.....	162
Results and Discussion .....	165
Tissue phantom .....	165
Canine tibia.....	166
Reconstruction Using Spatial Priors .....	166
Tissue phantom .....	166
Canine tibia.....	167
Conclusions.....	169
References.....	181
<b>IX. CONCLUSIONS AND FUTURE DIRECTIONS.....</b>	<b>187</b>
References .....	191
<b>APPENDICES.....</b>	<b>192</b>

## LIST OF FIGURES

### **Figure**

2.1	Cross-sectional schematic of the photon diffusion effects on light injected at a single point and asymmetric collection efficiency of two fibers located at different distances from the injection point.....	27
2.2	Schematic of the experimental apparatus. Components are labeled. Probe is a globally illuminated fiber optic probe with fifty collection fibers in a closely packed circle .....	28
2.3	Configuration of test systems. Light is incident on the surface of the top layer (shaded circle). (a) system I, three layers (2mm polyethylene, 2mm Delrin, and 13mm Teflon) (b) system II, 5.2 mm polyethylene, 13mm thick block Teflon (c) system III, 5.2 mm thick Delrin, 5.2 mm thick polyethylene, 13mm thick Teflon (d) system IV, subsurface interface, 13mm block of Teflon over 5.2mm thick polyethylene and 5.2mm thick Delrin, illumination centered over boundary .....	29
2.4	Raman spectra of Delrin (top), polyethylene (middle), and Teflon (bottom).....	30
2.5	(a) averaged Raman spectra of system I (b) recovered BTEM factors of the three components (Top: polyethylene; Middle: Delrin; Bottom: Teflon) (c) Raman spectra of the three components in model system. ....	31
2.6	(a) BTEM Teflon spectrum (solid line) system II, Teflon spectrum (dashed line) (b) BTEM polyethylene spectrum, reference polyethylene spectrum (dashed line) (c) 8 level gray-scale map. Darker circles represent greater Raman contribution from the surface layers (polyethylene) and the lighter circles represent greater Raman contribution from the subsurface layers (Teflon) (d) 2 level gray-scale map, black circles represent greater Raman contribution from the surface layer (polyethylene) and white circles represent greater Raman contribution from the subsurface layer (Teflon) .....	32
2.7	(a) solid line the averaged spectrum collected from system III, dashed line a reference spectrum of Delrin (b) detailed image of the	



	circled region in a. (c) solid line BTEM factor for Teflon, dashed line, reference Teflon spectrum (d) solid line the BTEM factor for polyethylene, dashed line polyethylene reference spectrum.....	33
2.8	(a) solid line BTEM factor for Delrin, dashed line, Delrin reference spectrum (b) solid line BTEM factor for polyethylene dashed line, polyethylene reference spectrum (c) subsurface 8 level gray scale map of polyethylene-Delrin interface beneath 13mm of Teflon, lighter circles contain a greater Delrin Raman contribution, darker circles contain a greater polyethylene Raman contribution (d) subsurface 2 level gray scale map of polyethylene-Delrin interface below 13mm of Teflon. Lighter circles contain a greater Delrin Raman contribution, darker circles contain a greater polyethylene Raman contribution (e) relative intensity surface histogram of the subsurface map.....	34
3.1	Schematic of the experimental apparatus. Components are labeled. The probe is a globally illuminated fiber-optic probe with 50 collection fibers in a closely packed circle .....	45
3.2	Raman spectra of chicken tibia (distal-diaphysis). (a) The spectrum collected by the fiber probe averaged over all 50 collection fibers. The solid line trace is the transcutaneous spectrum and the dotted line is the exposed bone spectrum. (b) Recovered bone tissue factor transcutaneous measurement (solid line) and the exposed bone spectrum (dashed line). .....	46
3.3	Raman spectra of chicken tibia with the averaged spectrum from the 50 probe collection fibers. Transcutaneous spectrum (dashed line), exposed bone (dotted line), and bone spectrum recovered from transcutaneous measurements (solid line). .....	47
3.4	Raman spectra of the lateral epicondyle at the humerus. (a) the spectrum collected by the fiber probe averaged over all 50 collection fibers. The solid line trace is the transcutaneous spectrum and the dotted line is the exposed bone spectrum. (b) Recovered bone tissue factor transcutaneous measurement (solid line) and the exposed bone spectrum (dashed line). .....	48
4.1	Schematic of fiber optic Raman system. The components are as marked in the figure. Lenses of different focal lengths were used to adjust dimensions of illuminating annulus as needed. The drawing is not to scale. ....	63
4.2	Transcutaneous Raman spectra of rat tibia. The spectrum integration times are shown on the figure. The bands are: phosphate, 958 cm <sup>-1</sup> ;	

carbonate, 1070 cm <sup>-1</sup> ; amide III, 1240-1270 cm <sup>-1</sup> ; matrix CH <sub>2</sub> deformation, 1446 cm <sup>-1</sup> .....	64
4.3 Measurements made through 4mm of overlying tissue on a chicken tibia at the mid diaphysis. Transcutaneous (dotted), recovered bone factor (gray), exposed bone (black). (a) recovered bone factor using data from all 50 collection fibers. (b) recovered bone factor using data from the 32 innermost collection fibers .....	65
4.4 Subsurface mapping performance for each probe: Subsurface maps of polyethylene/Delrin interface acquired from global illumination/collection probe (top row) and ring/disk illumination/collection (bottom row) at different overlying Teflon thicknesses. The Polymer model system is shown in the upper left corner .....	66
4.5 Raman spectra of chicken tibia (distal-diaphysis). (a) The mean spectra acquired by the global illumination/collection probe and the ring/disk probe operated at five different ring/disk separations (traces labeled). (b) The average background resulting from the different illumination/collection geometries for each probe. (c) The normalized and baselined mean transcutaneous spectra for each probe configuration .....	67
4.6 Recovered (BTEM) bone factor for the global illumination/collection probe (top trace), ring/disk probe using a combined data set (middle trace), and averaged exposed bone measurement (bottom trace) .....	68
5.1 Schematic of the experimental apparatus. Probe generates a single ring that can be varied in diameter, light is collected from the center of the ring .....	89
5.2 Configuration of polymer test systems. Light is incident on the surface of the top layer (shaded circle). (a) subsurface interface between polyethylene (4mm thick) and Delrin (4mm thick) under Teflon (b) Delrin target under Teflon. Teflon layer was systematically varied.....	90
5.3 Schematic of ring illumination/disk collection. Center diameter is defined as the diameter of the illumination ring measured from the center of the laser beam .....	91
5.4 Raman spectra of ( <i>top</i> ) polyethylene, ( <i>middle</i> ) Delrin, and ( <i>bottom</i> ) Teflon.....	92
5.5 Raman spectra of subsurface interface (a) polyethylene and Delrin contributions to the mixed component spectra at four different	

ring/disk spacings, with 5.6mm of overlying Teflon ( <b>b</b> ) averaged (n=200) spectra of all four ring/disk spacings combined (rings equally weighted) into a single data set with varying amounts of overlying Teflon.....	93
5.6 Fiber maps of subsurface interface at different ring/disk spacings.....	94
5.7 Varying amounts of Teflon over Delrin ( <b>a</b> ) averaged (n=200) mixed component spectra. The insert shows the 800 to 1200 cm <sup>-1</sup> region magnified to emphasize the subsurface contribution ( <b>b</b> ) BTEM recovered Delrin factors.....	95
5.8 Transcutaneous Raman spectra of dog tibia positioned at the medial side of the left tibia at the dyaphysis, 2mm of overlying tissue ( <b>a</b> ) averaged (n=500) transcutaneous, spectrum (gray) and exposed bone spectra (n=100) (black) ( <b>b</b> ) recovered bone spectrum for each ring/disk spacing ( <b>c</b> ) carbonate/phosphate band area ratio; comparison of the recovered bone spectra for each ring to the exposed bone measurement ( <b>d</b> ) carbonate/phosphate band height ratio; comparison of the recovered bone spectra for each ring to the exposed bone measurement .....	96
5.9 Phosphate $\nu_1$ /phenylalanine ring breathing band height and area ratios as functions of ring diameter.....	97
5.10 Transcutaneous Raman spectra of dog tibia at the medial side of the right tibia at the dyaphysis, 5mm of overlying tissue ( <b>a</b> ) averaged (n=250) transcutaneous spectrum (dashed), exposed bone spectra (n=100) (black), and recovered bone spectra (gray) ( <b>b</b> ) Phosphate $\nu_1$ /phenylalanine ring breathing band height ratio as functions of ring diameter (circles), approximation of expected function (line) ( <b>c</b> ) carbonate/phosphate band area and height ratios for the recovered and exposed bone spectra.....	98
6.1 Schematic of experimental apparatus .....	116
6.2 Raman spectra of a murine tibia (distal diaphysis). The bone tissue is approximately 1 mm below the skin. The gray traces are raw spectra obtained without optical clearing, and the black traces are spectra obtained after glycerol application (a) Transcutaneous Raman spectra (b) Power spectra.....	117
6.3 rms intensity for power spectra in high transform frequency region (mean + standard deviation) (a) Results for measurements made on six different tibiae (b) Results across tibiae from all mice .....	118

6.4	Effect of not centering the illumination line in the center of the collection fibers (a) Correct alignment of illumination line and collection disk with respect to the bone (b) Field of view of the collection fibers for proper alignment (c) Field of view of the collection fibers for improper alignment (d) Resulting noise levels in measurements made with improper alignment (compare to Fig. 3) (e) Mean transcutaneous spectra, after baselining and normalizing, for a measurement before and after glycerol application .....	119
6.5	(a) Typical mean transcutaneous spectrum (gray) and typical mean exposed bone spectrum (black) (b) Recovered bone factor without an optical clearing agent (gray), recovered bone factor after glycerol application (black), and exposed bone measurement (dotted).....	120
6.6	Cross-correlation coefficient between the exposed bone measurement and the recovered bone factor (mean + standard deviation) (a) Results for measurements made on six different tibiae (b) Results across tibiae from all mice.....	121
7.1	(a) Schematic of Raman spectroscopy system for <i>in vivo</i> measurements on mice. (b) Photograph of mouse restraint, showing water cooling and anesthesia delivery subsystems .....	142
7.2	Schematic of a mouse tibia with five different illumination (striped) and collection (solid) optical configurations.....	143
7.3	Schematic of probe alignment on a left mouse tibia.....	144
7.4	(a) Average transcutaneous signal for the five different Raman probe configurations of Fig. 2. (b) Superimposed standardized spectra from each of the fifty collection fibers for each probe configuration. ....	145
7.5	Representative recovered bone factor for the <i>in vivo</i> transcutaneous measurements (a) compared to the individual exposed bone spectra and (b) the average exposed bone spectrum of specimen 19. (c) The correlation coefficient results for all specimens .....	146
7.6	(a) Average carbonate-to-phosphate ratio for all mice. (b) Average carbonate-to-phosphate ratio by mouse showing the standard deviation of the exposed bone measurements and of the recovered bone factors .....	147
7.7	(a) Correlation coefficient and (b) coefficient of variation over the correlation coefficients, grouped by coat color.....	148

7.8	Average phosphate-to-phenylalanine height ratio taken from the transcutaneous signal collected by each fiber for each of the probe alignments .....	149
7.9	(a) Difference in the carbonate-to-phosphate ratio between the recovered bone factor and the exposed bone spectrum for each specimen and average difference over all four mice (dashed line) for each probe alignment (b) Coefficient of variation between the carbonate-to-phosphate ratios for each of the probe alignments .....	150
8.1	(a) Reflectance mode instrumentation for Raman measurements is shown using a ring/disk geometry. The ring diameters can be varied to sample multiple depths for tomographic reconstruction. (b) Transmission mode configuration is shown using a rectangular array of collection fibers at 180 degrees from the line source illumination. Multiple projections across the tissue can be obtained by rotating the sample with respect to the source-collection fiber setup .....	171
8.2	(a) Schematic of the tissue phantom (b) Average Raman spectra from one tissue phantom acquisition .....	172
8.3	(a) Phosphate to phenylalanine ratio for determining the ring/disk separations for optimal signal recovery (b) Mean transcutaneous (gray), recovered bone factor (black), and exposed bone Raman spectrum (dashed) .....	173
8.4	(a) five level fiber maps of the Raman Teflon® signal for each fiber (b) slice of the Raman tomographic reconstruction of the Teflon sphere .....	174
8.5	(a) ring/disk bone factor score plot (b) slice of the ring/disk Raman tomographic reconstruction of the canine tibia with the true location of the bone outlined in dark red .....	175
8.6	(a) transmission probe bone factor score plot (b) slice of the transmission probe Raman tomographic reconstruction of the canine tibia with the true location of the bone outlined in white .....	176
8.7	Cross-section of the reconstructed volume showing IG-RS estimates of the tissue phantom imaged using the ring/disk probe. The Teflon® inclusion was recovered with a contrast of 460:1 with respect to the background agar/1% Intralipid® gel.....	177
8.8	Development of mesh for tomographic reconstruction. a) Micro-CT image of canine hind limb section. c) Geometric image of tissues from micro-CT data .....	178

8.9 A cross-section of the reconstructed IG-RS estimates using (a) reflectance measurements from the ring/disk configuration and (b) transmission measurements using the rectangular array of collection fibers. Recovered contrast between the bone and background skin was more than 100-fold higher using transmission measurements than using reflectance data, as seen from the scale for reconstructed Raman yield..... 179

## LIST OF TABLES

### **Tables**

4.1	Carbonate/Phosphate ratios measured transcutaneously and on exposed bone.....	69
4.2	Illumination ring geometry and disk offsets .....	70
5.1	Ring/disk spacings .....	99
8.1	Illumination ring geometries.....	180

## LIST OF APPENDICES

Appendix 1: Publications.....	192
Appendix 2: Matlab scripts and functions .....	194



## **ABSTRACT**

Light scattering prevents the direct chemical monitoring of tissue and turbid materials, making it difficult to obtain accurate chemical information. We have developed novel fiber optic Raman probes for biomedical applications that are capable of recovering Raman spectra through several millimeters of overlying turbid materials such as skin, muscle, and adipose tissue. This is accomplished by spatially separating the region that is illuminated from the collection fields of view. In light scattering systems, this spatial separation emphasizes signal originating from below the surface of the scattering material. Engineering polymers and animal models have been used to investigate the depths at which accurate Raman spectrum recovery is achievable and to demonstrate the preservation of spatial information. Using these novel fiber optic probe configurations we have recovered accurate Raman spectra of bone tissue through 5 mm of overlying tissue; we have validated our measurements in vivo and demonstrated Raman tomography for the first time.

# **CHAPTER I**

## **INTRODUCTION TO RAMAN SPECTROSCOPY THROUGH LIGHT SCATTERING MATERIALS WITH BONE AS A TARGET**

### **Introduction**

The ability to make transcutaneous measurements would greatly expand the role of Raman spectroscopy as a tool for basic biomedical studies and clinical diagnostics. For example, it could reduce the number of animals sacrificed in longitudinal studies and it could supplement or replace some diagnostics that are known to have important limitations. However, transcutaneous measurements are complicated by the optical properties of tissue. Animal tissue is a highly scattering material with complex optical properties that limit the depths at which signal recovery is achievable. In this dissertation research, we have developed new Raman methodology for the recovery of bone spectrum through skin and other overlying tissue. Bone is an ideal target because the mineral spectrum does not resemble the spectrum of overlying soft tissue components. As a result, multivariate data reduction methods are well suited to separate out a bone spectrum as a component of transcutaneously acquired spectra.

Raman spectroscopy, like infrared spectroscopy, is a form of vibrational spectroscopy. Infrared spectroscopy is a direct absorption method and consequently, in

tissue, water absorption limits the infrared depth of penetration to a few tens of microns. Alternatively, Raman spectroscopy is based on light scattering rather than absorption. Raman has the advantage that spectra are excited with visible or near-infrared lasers. As a result water absorption in tissue is less of a problem than in infrared spectroscopy. Also, Raman spectroscopy is compatible with glass and fused silica optics, including standard optical fibers.

### **Light Scattering**

It is useful to briefly review the interaction of light with tissue in order to make clear what is meant by the term light scattering as opposed to Raman scattering. When a photon of wavelength different than the wavelengths at which it absorbs interacts with a molecule, it excites an electron into a virtual excited state. Most of the time the electron (instantaneously) decays back to its ground state emitting a photon of the identical wavelength as the incident photon. This is called Rayleigh scattering. However, for a small fraction of the incident photons ( $\sim 1$  in  $10^7$  photons) the excited virtual state decays to an excited vibrational level, (instantaneously) emitting photons at longer wavelengths. The scattered light is the Stokes shifted Raman spectrum and is usually just called the Raman spectrum. Less frequently, because there is an excited vibrational population at room temperature, some scattering occurs to lower wavelengths. Because the signal is very weak this spectrum is rarely used, except as a measure of temperature. The Raman spectrum is usually reported as wavenumber ( $\text{cm}^{-1}$ ) shifts from the wavenumber of the

exciting light. In this format, the spectrum is independent of the wavelength of the exciting light.

The Raman bands result from molecular vibrations that are characteristic of the chemical units present in the molecule. Each has its own modes of vibration, and so there is chemical composition information in the Raman spectrum. In the case of tissue or any other material that has more than one component, Raman spectrum is a linear superposition of all the pure component spectra. These scale according to their proportions in the tissue.

Because of the weakness of the water Raman spectrum, Raman spectroscopy is especially suitable for use with water-rich systems such as tissue. In many cases fresh tissue or tissues that have been fixed and embedded for microscopy can be used with little preparation. Because of these strengths, Raman spectroscopy is under extensive investigation for biomedical applications.<sup>1-4</sup>

While modern Raman spectroscopic instruments can generate spectra rapidly, tissue components are not intense Raman scatterers and can not be subjected to high laser powers. In many cases, Raman spectroscopy is not yet fast enough for use as a non-invasive clinical diagnostic. Also, Raman spectroscopy in tissue remains limited: optical properties of the tissue limit depth of light penetration and signal collection efficiency.

Soft tissue is a highly scattering material because of the refractive index mismatches at the interfaces between cellular organelles, cell membranes, cell nuclei, intracellular fluids, lipids, and collagen that make up tissue. Here it is important to distinguish between the elastic scattering that occurs as a photon migrates through tissue and the inelastic scattering that is the Raman effect. Light propagation through tissue is

termed photon migration (also referred to throughout the remainder of this dissertation as light scattering) because it is the resultant of straight line travel and multiple scattering events. Most tissue components are larger than a wavelength of light so tissue scattering is mostly Mie scattering. Mie scattering efficiency is wavelength independent. A textbook example of Mie scattering is the grayish white color of a cloudy sky, observed because sunlight is scattered by relatively large water particles. In the absence of clouds a blue color is observed. This blue color is a result of Rayleigh scattering, which is wavelength dependent ( $1/\lambda^4$ ) and is the form of elastic scattering for particles (including molecules) that are much smaller than the wavelength of light. Rayleigh scattering is essentially the small-size limiting case of Mie scattering.<sup>5</sup> When light propagates through tissue it will encounter particles that are smaller than the wavelength of light (Rayleigh scattering intensity  $\sim 1/\lambda^4$ ), others with dimensions similar to the wavelength of light (scattering intensity  $\sim 1/\lambda^0$  to  $\sim 1/\lambda^4$ ), and larger than the wavelength of light (Mie scattering intensity  $\sim 1/\lambda^0$ ). As light travels through the many tissue components, it changes velocities and directions many times. A light beam will spread out as it travels through tissue.

Because tissue contains particles that span the size range between the limiting cases of Mie scattering and Rayleigh scattering the behavior is too complicated for exact theoretical treatments. Instead, empirical random walk models are used. Qualitatively, light propagation is said to proceed by three different mechanisms: straight line travel, few scattering events, and many scattering events. Photons are said to be ballistic, snake-like, and diffusive, depending on how many scattering events they undergo. Ballistic photons will travel the deepest into the tissue because of minimal interaction with the

surrounding material. The number of ballistic photons decreases exponentially as a function of depth and the scattering properties of the material. Snake-like photons move in a snake-like motion changing direction several times as a result of the changes in refractive index. Snake-like photons travel the second deepest into the tissue. Diffusive photons travel randomly through the tissue because they undergo many scattering events. Tissue is such a highly scattering material that in many experiments all of the recovered photons can be considered diffusive.<sup>6, 7</sup> Of course attenuation by light absorption is superimposed on attenuation by scattering.

### **Diagnostic Window**

The percentage of light that migrates through the tissue is dependent on the wavelength of light because of light absorption by endogenous components. To reach the greatest depths possible in soft tissue, it is necessary to use NIR light. For Raman spectroscopy either a 785 nm or an 830 nm diode laser is typically used.

There is extensive absorption from melanin and hemoglobin at wavelengths lower than 600 nm. At wavelengths higher than 1200 nm the absorption from water increases rapidly. Photon migration (light scattering) is the dominant source of attenuation in the spectral region in which absorption from water, hemoglobin, lipids, and melanin are minimal. For this reason, the 600-1200 nm range of wavelengths has been called the diagnostic or therapeutic window.<sup>8</sup>

In transcutaneous Raman measurements it is advantageous to minimize the light that is absorbed. Absorbed light is dissipated in the tissue as either heat or fluorescence.

Heat can cause discomfort or tissue damage if high laser power is used. Fluorescence becomes a large background signal that can be difficult to subtract accurately and that contributes shot noise to the measured Raman spectrum. Selection of the longest feasible NIR wavelength within the diagnostic window will minimize the melanin and hemoglobin absorption fluorescence component without incurring too much water absorption. Though the diagnostic window extends to 1200 nm, silicon photon detectors have low sensitivity/quantum efficiency at wavelengths greater than 1000 nm. As a result wavelengths higher than 830nm are not commonly used.

### **Optical Clearing of Tissue**

Even with the appropriate excitation wavelength, photon diffusion obscures the deep penetration of light into tissue. There are several known techniques to minimize scattering and increase the depth of light penetration in tissue.<sup>9</sup> These techniques include mechanically compressing or stretching the skin, thermally heating or cooling the skin, and optical clearing. Although the techniques are different, the optical effect is similar. All operate by reducing the number or magnitude of sudden changes in refractive index. By mechanically stretching or compressing the skin the tissue homogeneity is increased by the removal of blood and interstitial fluids. This effectively causes closer packing of the tissue. Light scattering is reduced because there is less variation in the index of refraction because of the increased homogeneity

Thermally heating and cooling the skin has similar effects, but with less predictable results because of the variability of underlying fat layers, especially in

humans. At higher temperatures, lipids become more fluid, thereby decreasing the scattering coefficients. At the same time there is an increase in the tissue hydration in the dermis, causing greater tissue scattering. Cooling has the opposite effect and in less fatty tissue may be used to constrict blood vessels and decrease tissue hydration.

Optical clearing is the procedure of adding a liquid to the tissue that replaces water and has a refractive index that is closer to those of proteins and lipids. Commonly, a clearing agent is rubbed on the skin to displace the water in the skin, replacing it with a material of higher refractive index. Ordinary skin lotions or moisturizers can be used, as can compounds such as glycerol. The thickness of the tissue that exhibits decreased scattering is greatly influenced by how well the clearing agent is absorbed into the skin and how well its components match the refractive index of collagen and other skin components. Optical clearing can offer a marked improvement in the signal/noise ratio of the recovered Raman spectrum of bone.<sup>10</sup>

### **Transcutaneous Raman Measurements**

There are two reported Raman methods for obtaining transcutaneous Raman spectrum of bone: picosecond Kerr-gating<sup>11, 12</sup> and spatially separating the illumination from the collection field of view, termed spatially offset Raman spectroscopy (SORS).<sup>13</sup> Though both techniques have been shown to recover bone spectrum through the skin, picosecond Kerr gating uses bulky and expensive instrumentation that is only available in a few laboratories worldwide. However, signal recovery by SORS can be performed with commercially available Raman instrumentation.



In the SORS fiber optic collection techniques, subsurface and spatial information is obtainable by using an array of collection fibers some of which are spatially offset from the center of illumination.<sup>14</sup> This family of techniques is well documented in the biomedical optics literature,<sup>15-17</sup> but has only recently been reported for Raman.

Obtaining subsurface information through SORS signal collection is based on the properties of photon migration. Incident NIR photons diffuse through soft tissue. The Raman scattered photons continue to diffuse on the path back to the specimen surface. Compared to Raman scatter collected directly below the point of illumination, Raman scatter collected away from the center of illumination will contain a larger proportion of Raman photons that originate from below the surface. The ratio is dependent on the distance from the center of illumination. By varying the distance of the collection fibers from the center of illumination, a variation in the proportion of surface to subsurface Raman signal results. Using this technique, we have generated coarse subsurface Raman maps<sup>18-20</sup> and three dimensional tomographic reconstructions<sup>21,22</sup>.

Subsurface component recovery is an ill-posed inverse problem. It is solved using an algorithm in which the known subsurface spectrum of interest is treated as a component. We do not know the number of components, but we do know what the spectrum of the combination of components looks like. Well known algorithms that fit this purpose include BTEM,<sup>23,24</sup> SIMPLISMA,<sup>25</sup> IPCA,<sup>26</sup> and OPA-ALS.<sup>27</sup>

## **Data Analysis**

Band target entropy minimization (BTEM) is the algorithm in use in our laboratory. It has previously been applied to hyperspectral Raman imaging and has been shown to recover components that are missed by other multivariate data reduction methods.<sup>28</sup> In Raman spectroscopy a mixed component spectrum is a linear superposition of pure component spectra which scale according to their concentration. Singular value decomposition is used to calculate eigenvectors of the mixed component spectrum; the sum of all the eigenvectors will reproduce the mixed component spectrum. The first eigenvector will contain a spectrum that describes the greatest amount of variance in the dataset and the last eigenvector will contain a spectrum that describes the least amount of variance in the dataset, typically almost all noise. The BTEM method looks at the information dispersion across the dataset with the objective of minimizing the dispersion. Unlike other algorithms BTEM utilizes the small amount of signal in eigenvectors that are usually rejected as noise. The spectral recovery for a component of interest is accomplished by choosing a spectral region where the component of interest has a visible band in the mixed component spectrum. The entropy at the region of interest is calculated for a predetermined number of eigenvectors. The entropy calculation is then used as a weight to rotate the determined number of eigenvectors into each other, resulting in a spectrum of minimum entropy for the band that was chosen.

### **Applications to bone**

Bone is a living tissue. It is a highly organized, dynamic composite material comprised of mineral, organic matrix, cells, and water. On a macroscopic scale bone is

composed of cortical bone and trabecular bone (cancellous bone). Cortical bone makes up 80% of the skeletal bone mass while trabecular bone is the remaining 20%. Cortical bone is much denser (5-10% porosity) than trabecular bone (50-90% porosity) and is found in the shafts of long bones and as an outer shell around the trabecular bone. At the chemical composition level bone is a composite of a protein matrix, which is about 85% type I collagen, and a carbonated apatitic mineral. The mineral resembles hydroxyapatite  $[\text{Ca}_{10}(\text{PO}_4)_6(\text{OH})_2]$ , but in mature bone about a quarter of the phosphate is replaced by carbonate. The apatitic crystals are nanometer sized and are present in spaces between and around collagen fibrils that make up the organic matrix. A collagen fibril consists of type I collagen triple helical structures that are interconnected by short cross-links. Other cross-links connect the three strands of the triple helix. There are correlations between the mechanical properties of bone and its chemical structure. Roughly, the mineral contributes stiffness and the collagen contributes flexibility. The mechanical properties of bone result from the interplay of bone architecture, bone composition, bone turnover, and damage accumulation. These complex contributions to bone strength are described as bone quality.<sup>29</sup>

Our group has shown that Raman spectroscopy gives some insight into bone quality. Present and former group members have shown measurable spectral changes in both the mineral and matrix bands when bone is permanently or elastically deformed.<sup>30-32</sup> In these studies band area and height ratios were used as Raman spectroscopic signatures to characterize mineral carbonation, and matrix cross-linking. There are also characteristic differences in the spectra of wild type mice and *Brtl* mice, a model for osteogenesis imperfecta Type IV.<sup>33</sup>

More recently, McCreadie et al. have shown that there are differences between the Raman spectra of osteoporotic bones that have undergone fracture and matched tissue from donors who died without suffering fracture.<sup>34</sup> Among the results reported, the carbonate-to-phosphate band ratio was approximately 20% higher in the bone that had undergone fracture. These and other studies suggest that transcutaneous Raman spectroscopy can play an important role in the study of bone tissue.

## References

1. A. S. Haka, Z. Volynskaya, J. A. Gardecki, J. Nazemi, J. Lyons, D. Hicks, M. Fitzmaurice, R. R. Dasari, J. P. Crowe and M. S. Feld, "In vivo Margin Assessment during Partial Mastectomy Breast Surgery Using Raman Spectroscopy," *Cancer Res.* 66(6), 3317-3322 (2006)
2. C. L. Evans, E. O. Potma, M. Puoris'haag, D. Côte', C. P. Lin and X. S. Xie, "Chemical imaging of tissue in vivo with video-rate coherent anti-Stokes Raman scattering microscopy," *PNAS USA* 102(46), 16807-16812 (2005)
3. B. R. Hammond and B. R. Wooten, "Resonance Raman spectroscopic measurement of carotenoids in the skin and retina.," *J. Biomed. Opt.* 10(5), 054002 (2005)
4. I. P. Torres Filho, J. Turner, R. N. Pittman, L.G. Somera 3rd and K. R. Ward, "Hemoglobin oxygen saturation measurements using resonance Raman intravital microscopy," *Am. J. Physiol. Heart Circ. Physiol.* 289(1), 488-495 (2005)
5. E. Hecht, "Optics", Addison Wesley, 4th edition ,New York, (2002)
6. V. Tuchin, *Tissue Optics Light Scattering Methods and Instruments for Medical Diagnosis*, SPIE Press, Bellingham, (2000).
7. T. Vo-Dinh, *Biomedical Photonics Handbook*, CRC Press, Boca Raton (2003).
8. R. Richards-Kortum and E. Sevick-Muraca, "Quantitative Optical Spectroscopy for Tissue Disagnosis," *An. Rev. Phys. Chem.* 47, 555-606 (1996)
9. V. Tuchin, *Optical Clearing of Tissue and Blood*, SPIE Press, Bellingham, (2006).
10. M. V. Schulmerich, J. H. Cole, K. A. Dooley, J. M. Kreider, S. A. Goldstein and M. D. Morris, "Optical clearing in transcutaneous Raman spectroscopy of murine cortical bone tissue," *J. Biomed. Optics* 13(2), 021108 (2008)

11. E. Draper, M. D. Morris, N. P. Camacho, P. Matousek, M. Towrie, A. W. Parker and A. E. Goodship, "Novel Assessment of Bone Using Time-Resolved Transcutaneous Raman Spectroscopy," *J. Bone Miner. Res.* 20(11), 1968-1972 (2005)
12. M. D. Morris, P. Matousek, M. Towrie, A. W. Parker, A. E. Goodship and E. R. C. Draper, "Kerr-gated time-resolved Raman spectroscopy of equine cortical bone tissue," *J. Biomed. Opt.* 10, 014014 (2005)
13. P. Matousek, "Deep non-invasive Raman spectroscopy of living tissue and powders," *Chem. Soc. Rev.* 36(8), 1292-1304 (2007)
14. P. Matousek, M. D. Morris, N. Everall, I. P. Clark, M. Towrie, E. Draper, A. Goodship and A. W. Parker, "Numerical Simulations of Subsurface Probing in Diffusely Scattering Media Using Spatially Offset Raman Spectroscopy " *Appl. Spectrosc.* 59(12), 1485-1492 (2005)
15. T. J. Pfefer, K. T. Schomacker, M. N. Ediger and N. S. Nishioka, "Multiple-fiber probe design for fluorescence spectroscopy in tissue," *Appl. Opt.* 41(22), 4712-4721 (2002)
16. J. R. Mourant, J. Boyer, A. H. Hielscher and I. J. Bigio, "Influence of the scattering phase function on light transport measurements in turbid media performed with small source-detector separations," *Opt. Lett.* 21(7), 546-548 (1996)
17. U. Utzinger and R. R. Richards-Kortum, "Fiber optic probes for biomedical optical spectroscopy," *J. Biomed. Opt.* 8(1), 121-147 (2003)
18. M. V. Schulmerich, K. A. Dooley, T. M. Vanasse, S. A. Goldstein and M. D. Morris, "Subsurface and Transcutaneous Raman Spectroscopy and Mapping Using Concentric Illumination Rings and Collection with a Circular Fiber-Optic Array," *Appl. Spectrosc.* 61(7), 671-678 (2007)
19. M. V. Schulmerich, W. F. Finney, R. A. Fredricks and M. D. Morris, "Subsurface Raman Spectroscopy and Mapping Using a Globally Illuminated Non-Confocal Fiber-Optic Array Probe in the Presence of Raman Photon Migration," *Appl. Spectrosc.* 60(2), 109-114 (2006)
20. M. V. Schulmerich, M. D. Morris, T. M. Vanasse and S. A. Goldstein, "Transcutaneous Raman spectroscopy of bone: global sampling and ring/disk fiber optic probes," *Proc. SPIE* 6430(643009), 1-8 (2007)

21. M. V. Schulmerich, S. Srinivasan, J. Kreider, J. H. Cole, K. A. Dooley, S. A. Goldstein, B. W. Pogue and M. D. Morris, "Raman tomography of tissue phantoms and bone tissue," Proc. SPIE 6853, 68530V (2008)
22. M. V. Schulmerich, S. Srinivasan, J. H. Cole, J. Kreider, K. A. Dooley, S. A. Goldstein, B. W. Pogue and M. D. Morris, "Non-invasive Raman tomographic imaging of canine cortical bone tissue," J. Biomed. Optics 13, 020506 (2008)
23. W. Chew, E. Widjaja and M. Garland, "Band-Target Entropy Minimization (BTEM): An Advanced Method for Recovering Unknown Pure Component Spectra. Application to the FTIR Spectra of Unstable Organometallic Mixtures," Organometallics 21, 1982-1990 (2002)
24. E. Widjaja, C. Li and M. Garland, "Semi-Batch Homogeneous Catalytic In-Situ Spectroscopic Data. FTIR Spectral Reconstructions Using Band-Target Entropy Minimization (BTEM) without Spectral Preconditioning," Organometallics 21, 1991-1997 (2002)
25. W. Windig and J. Guilment, "Interactive Self-Modeling Mixture Analysis," Anal. Chem. 63, 1425-1432 (1991)
26. D. Bu and C. W. Brown, "Self-Modeling Mixture Analysis by Interactive Principal Component Analysis," Appl. Spectrosc. 54(8), 1214-1221 (2000)
27. A. Garrido Frenich, M. Martinez Galera, J. L. Martinez Vidal, D. L. Massart, J. R. Torres-Lapasió, K. De Braekeleer, J.-H. Wang and P. K. Hopke, "Resolution of multicomponent peaks by orthogonal projection approach, positive matrix factorization and alternating least squares," Anal. Chim. Acta 411, 145-155 (2000)
28. E. Widjaja, N. Crane, T.-C. Chen, M. D. Morris, M. A. Ignelzi and B. R. McCreadie, "Band-Target Entropy Minimization (BTEM) Applied to Hyperspectral Raman Image Data," Appl. Spectrosc. 57(11), 1353-1362 (2003)
29. M. Stauber and R. Müller, "Volumetric spatial decomposition of trabecular bone into rods and plates—A new method for local bone morphometry," Bone 38, 475-484 (2006)
30. A. Carden and M. D. Morris, "Application of vibrational spectroscopy to the study of mineralized tissues (review)," J. Biomed. Opt. 5(3), 259-268 (2000)

31. A. Carden, R. M. Rajachar, M. D. Morris and D. H. Kohn, "Ultrastructural Changes Accompanying the Mechanical Deformation of Bone Tissue: A Raman Imaging Study," *Calcif. Tissue Int.* 72, 166-175 (2003)
32. M. D. Morris, W. F. Finney, R. M. Rajacharb and D. H. Kohn, "Bone tissue ultrastructural response to elastic deformation probed by Raman spectroscopy," *Faraday Discuss.* 126, 159-168 (2004)
33. K. M. Kozloff, A. Carden, C. Bergwitz, A. Forlino, T. E. Uveges, M. D. Morris, J. C. Marini and S. A. Goldstein, "Brittle IV Mouse Model for Osteogenesis Imperfecta IV Demonstrates Postpubertal Adaptations to Improve Whole Bone Strength," *J. Bone Miner. Res.* 19(4), 614-622 (2004)
34. B. R. McCreadie, M. D. Morris, T.-C. Chen, D.S.Rao, W. F. Finney, E. Widjaja and S. A. Goldstein, "Bone Extracellular Matrix Compositional Differences in Women with and without Osteoporotic Fracture," *Bone* 39, 1190-1195 (2006)



## **CHAPTER II**

# **SUBSURFACE RAMAN SPECTROSCOPY AN MAPPING USING A GLOBALLY ILLUMINATED NON-CONFOCAL FIBER OPTIC PROBE IN THE PRESENCE OF RAMAN PHOTON MIGRATION**

### **Introduction**

The ability to rapidly obtain subsurface Raman spectra is a topic of considerable interest to both the biomedical and pharmaceutical fields. The development of a globally illuminated fiber optic probe is one of the recent technological advances that mark the first steps in realizing the potential of collecting subsurface chemical information by Raman spectroscopy. This type of fiber optic probe takes advantage of the efficient signal collection resulting from a non-confocal global illumination while binning and co-addition of signals from individual fibers are used to minimize collection time. A globally illuminated fiber optic probe with an array of collection fibers was first reported by Ma and Ben-Amotz to perform rapid Raman imaging.<sup>1</sup> An optically similar probe has been employed by Wikström et al. for pharmaceutical process analysis.<sup>2</sup> We exploit the advantages of a globally illuminated fiber optic probe to perform spatially offset Raman spectroscopy (SORS), and report the rapid collection of Raman spectra from subsurface

components. We also report the generation of low definition Raman maps of subsurface components in the presence of strong Raman photon migration.

The principle of collecting signal (typically fluorescence or absorption) from subsurface components is widely used throughout the biomedical optics field. In biological tissue optics the term photon migration is used to describe the effects of multiple scattering.<sup>3,4</sup> In most tissue types, elastic scattering contributes as much or more to light attenuation in the near-infrared, as absorption. As a consequence, theoretical treatments and methods for recovering spatial information have been extensively investigated by the tissue optics community.<sup>3,4</sup>

Although multiple scattering has long been known in Raman spectroscopy, detailed study of its effects have accelerated since the pioneering time-resolved work of Overall et al.<sup>5-7</sup> Our research group has applied the time-resolved methodology to recovery of subsurface signals in bone tissue.<sup>8,9</sup> While the time-resolved method is powerful the instrumentation required is expensive and available only in a few laboratories.<sup>10</sup> In collaboration with several other groups we have recently demonstrated that information from diffusive photons can be recovered with a simple probe geometry.<sup>11</sup> Spatially offsetting the point of signal collection from the point of laser delivery allows discrimination against signals from surface layers and enables collection of spectra from subsurface components. Spatially offset Raman spectroscopy (SORS) can be implemented in most Raman spectroscopy systems and is well suited for implementation with fiber optic probes. However, in its simplest form, SORS provides no information about spatial distribution of subsurface components. If multiple collection fibers are used, arranged in a circle or circles around the delivery fiber, as in the classic

N-around-1 probe, some spatial information may be recoverable. Because a tightly focused laser beam is delivered at a single point, the possibility of damage to delicate samples is much greater than in global illumination.

The non-confocality of global illumination Raman imaging is widely understood. Markwort and co-workers showed that multiple scattering can degrade global illumination Raman images.<sup>12</sup> As a result, Markwort et al. did not attempt to separate surface and subsurface signals. In this communication we demonstrate that subsurface Raman maps can be generated using global illumination and an array of collection fibers. Recovery of spectra depends upon the positional asymmetry of collection of diffusive photons arising from a single subsurface point. The basic principle of diffusional photon migration is illustrated in figure 2.1.

Excitation photons entering at a single point diffuse (are scattered) into a wide distribution as they propagate. Similarly, Raman-scattered photons originating at a single sub-surface point also diffuse and exit the sample not at a single point but distributed over a relatively wide area. Collection fibers located at different distances from the point of injection will therefore collect different numbers of Raman photons from subsurface regions directly below. The closer a fiber is to the injection point, the greater the contribution from the surface components and the further the fiber is from the injection point the greater the contribution from subsurface Raman photons. The same principle applies to an array of many fibers where each fiber collects signal from a subsurface component in proportions to its distance from the exiting photon's point of entrance to the sample and the depth of the component. The positional asymmetry means that subsurface spectral and spatial information is available from the ensemble of fibers.

Due to the large amount of collected data, the separation of Raman signal from noise or fluorescence is possible by using multivariate data reduction techniques, provided that the number of collection fibers equals or exceeds the number of spectroscopically distinguishable components. In order to recover spectral factors from the data an ill-posed inverse algorithm is especially useful. Well known algorithms that fit this purpose include SIMPLISMA, IPCA, and OPA-ALS.<sup>13-15</sup> Here we use band target entropy minimization (BTEM), a recently developed technique that has proven capable of extraction of weak infrared and Raman signals at better signal/noise ratio than several more familiar methods.<sup>16-20</sup> We have previously applied this method to hyperspectral Raman imaging and have demonstrated in that application that BTEM has the ability to recover components that are missed by other multivariate data reduction methods.<sup>21</sup>

In this paper we employ a global illumination 50 element fiber optic probe to investigate subsurface Raman spectroscopy and mapping. We use blocks of engineering polymers that have been chosen because they have spectra with some bands unique to each and other bands that strongly overlap.

## **Experimental**

The Raman system (figure 2.2) was comprised of a 400 mW 785 nm external cavity diode laser (Invictus, Kaiser Optical Systems, Ann Arbor, MI), an NIR-optimized imaging spectrograph (HoloSpec, f/1.8i, Kaiser Optical Systems) fitted with a 50  $\mu\text{m}$  slit to provide 6-8  $\text{cm}^{-1}$  spectral resolution. The detector was a thermoelectrically cooled

deep-depletion 1024x256 pixel CCD (Model DU420-BR-DD, Andor Technology, Belfast, Northern Ireland) operated at -70 °C with no binning. The sampling system was a filtered fiber optic probe with uniform global illumination and a bundle of fifty 100  $\mu\text{m}$  core, collection fibers arranged in a close-packed circle to collect light from the illuminated region (PhAT probe, Kaiser Optical Systems). At the spectrograph end the collection fibers were arranged in a linear array for coupling into the spectrograph. The probe was fitted with a 250 mm focal length fused silica lens that focused the laser beam to a 7mm diameter spot. The laser power available at the probe head was 285 mW.

The dispersion axis of the spectrograph was calibrated against the neon discharge lamp of a Kaiser Optical Systems Raman Calibration Accessory. The diffused quartz-halogen lamp light of the Calibration Accessory was used to flat-field the CCD. The integration time was 170 seconds, except for experiments using a stack of three polymers with polyethylene as the top polymer (Configuration 2.3a, as seen below).

The positional correspondence between fibers at the linear array end of the fiber bundle and the circular array end was measured by stepwise illumination using white light and a video camera. The focusing lens was removed from the PhAT probe and a video camera (TMC 7DSP, JAI Pulnix, Inc., San Jose, CA) fitted with a 35 mm focal length lens. The linear end of the fiber bundle was illuminated with a quartz-halogen lamp. The array was viewed with the video camera while an opaque block was translated across the line of fibers, extinguishing them one by one. As each fiber was extinguished, a video frame was captured with a frame grabber (PXC200AL, ImageNation, Beaverton, OR), establishing its location on the circular array.

The model systems were polyethylene, Delrin, and Teflon. These polymers were machined into 51 mm x 51 mm blocks of different thicknesses. These were arranged in two and three component systems of different scattering geometries, as described below. A 225 g brass block, with a hole cut through the center, was placed on top of an assembly of polymer blocks to minimize voids between them.

The test configurations are illustrated in figure 2.3. In figure 2.3a, 2.3b, and 2.3c slabs of two or three polymers were stacked. In the two layer configuration only polyethylene and Teflon were used. In the three layer configuration the upper and middle layers were 2.0 or 5.2 mm thick. The Teflon layer was 13 mm thick. The second configuration (Figure 2.3d) was used to illustrate recovery of spatially resolved spectra of subsurface components below a scattering layer. Blocks 5.2 mm thick of Delrin and polyethylene were butted against each other. A 13 mm thick Teflon block was placed over the interface. The fiber optic probe was centered over the boundary between the polyethylene and Delrin and incident on the Teflon block.

### **Data Treatment**

All data reduction was performed in Matlab 6.1 (The Mathworks Inc., Natick, MA) using locally written and vendor supplied scripts. The data for each experiment were arrays of 256 Raman spectra collected as single CCD images. Initial preprocessing included dark current subtraction, correction for pixel-pixel response variations, and correction for wavelength response dependence. The response-corrected images were then corrected for slit image curvature caused by the large gathering angle of the

spectrograph. A wavenumber region of interest (ROI) was then selected and the covariance matrix was calculated for data in this ROI. BTEM was used to obtain the spectral factors of interest. Typically a 3 pixel (approximately  $5\text{ cm}^{-1}$ ) interval including the most intense band in the ROI for a given polymer was chosen for targeting. The first fifty to seventy eigenvectors were used for the calculations of spectral factors and scores. The scores of the recovered polymer factors were used to construct score plots for all components for which light was collected at each fiber. The factors were normalized so that the sum of all the score plots for a polymer equaled the total light intensity collected by each fiber. The relative intensities were then calculated and mapped onto an image of the collection fibers.

## **Results and Discussion**

Reference spectra for Delrin, polyethylene, and Teflon were obtained with the PhAT probe and are shown on the same Raman signal intensity scale in figure 2.4. The top spectrum is of Delrin and is of the average from 256 spectra. The strongest band is at  $918\text{ cm}^{-1}$ . The middle spectrum is polyethylene (256 spectra averaged). The strongest Raman band is at  $808\text{ cm}^{-1}$ . The bottom spectrum is of Teflon (256 spectra averaged). The strongest band is found at  $732\text{ cm}^{-1}$ .

Figure 2.5 shows results obtained for a three layer system (figure 2.3a) consisting of a 2.1mm thick polyethylene block (top), a 2.1mm thick Delrin block (middle), and a 13mm thick Teflon block (bottom). Figure 2.5a is the spectrum averaged over the 256 CCD rows. Figure 2.5b shows the factors recovered by BTEM. The upper spectrum in

figure 2.5b is the polyethylene factor, the middle spectrum is the Delrin factor, and the lower spectrum is the Teflon factor. Each factor was recovered using 70 eigenvectors and targeting the wavenumber location at which the highest intensity Raman signal for the given polymer was expected. Figure 2.5c shows the reference Raman spectrum for each of the polymers in the same ROI.

Figure 2.6 shows results for a two layer system (figure 2.3b) consisting of a 5.2 mm thick polyethylene block over a 13 mm thick Teflon block. In figures 2.6a and 2.6b the spectra of the individual polymers (dotted lines) and recovered factors (solid lines) are shown. In figures 2.6c and 2.6d the relative intensities contributed by polyethylene and Teflon are mapped onto images of the collection fibers. The relative intensities were calculated by using reference Teflon and polyethylene spectra to calculate the score plot for each component. The contributions from each component were then calculated. In figure 2.6c the relative intensities were mapped on to an eight level gray scale in which black represents polyethylene and white represents Teflon. In figure 2.6d the difference in the collection efficiency at each fiber from the subsurface layer is emphasized by use of a two level gray scale.

The ability to recover subsurface information was further tested on a three layer system (figure 2.3c) consisting of a 5.2 mm upper Delrin layer, a 5.2 mm polyethylene middle layer and a 13 mm lower Teflon layer. The solid line spectrum in figure 2.7a is the average of 256 spectra. The averaged spectrum is dominated by the Delrin spectrum (dotted line) because the top layer is the major intensity contributor. The ROI used for BTEM recovery of subsurface spectra is circled in figure 2.7a. An enlarged view of the ROI is shown in figure 2.7b. In the ROI the polyethylene bands at  $810\text{ cm}^{-1}$  and  $842\text{ cm}^{-1}$



and a Teflon band at  $732\text{ cm}^{-1}$  are visible, although with very low intensity. BTEM recovers noisy spectra of polyethylene (figure 2.7c) below 5.2mm of Delrin. The spectrum of Teflon is recovered from below 5.2mm of Delrin and an additional 5.2mm of polyethylene (figure 2.7d). For comparison the spectra of Teflon and polyethylene in the ROI are shown (dotted lines) above the recovered spectra in figure 2.7c and figure 2.7d.

To test the spatial recovery capabilities of the method, the region around the linear boundary between 5.2 mm thick blocks of polyethylene and Delrin below a 13 mm layer of Teflon was mapped. Figure 2.8a and figure 2.8b shows factors for Delrin and polyethylene. These factors were used to calculate the contributing signal intensities for each of the subsurface components.

Figure 2.8c shows the relative intensities mapped (8 gray levels) onto an image of the fiber bundle (figure 2.8c). The darker the circle the greater the Raman signal contribution from the left side of the subsurface interface (polyethylene). The lighter the circle the greater the Raman contribution from the right side of the subsurface interface (Delrin). In figure 2.8d a two level gray scale is used to emphasize contributions from the right and left side of the subsurface interface. The black circles represent polyethylene and the white circles represent predominantly Delrin. Curiously, while Delrin gives a stronger Raman signal than polyethylene, it also scatters Raman light more strongly. The collection efficiency is reduced as the depths of the subsurface increases because of the greater scattering effect. As a result the recovered Raman signal for Delrin is less than the recovered Raman signal for polyethylene.

The histogram, shown in figure 2.8e, further illustrates the intensity contributions from the two subsurface polymers and is useful in understanding the source of apparent

anomalies in the images of figure 2.8c and 8d. The histogram was created by dividing the collection fiber map into nine vertical bins and averaging the intensity contributions of the two polymers for each bin. It becomes clear from the histogram that the fiber to fiber differences in intensities, which arise from multiple scattering effects, are actually quite small. Under these conditions small errors in measurement can result in positional errors, especially in a binary image such as figure 2.8d.

### **Conclusions**

The two- and three-component model systems employed here illustrate that a global illumination/multifiber collection bundle can recover subsurface spectra and provide maps of the component distribution. Global illumination reduces local power density and should prove especially useful in mapping delicate samples. The spatial resolution is governed by the number of fibers in the bundle, the dynamic range of the detector and ultimately by the inevitable scrambling of spatial information caused by the multiple scattering effect.

A particularly interesting challenge is to recover detailed spatial and spectral information in less contrived systems than assemblies of blocks of materials. For example, collection of spectra from a thin film sandwiched between two thicker layers would be more difficult because the film would be a minor contributor to the total signal at every fiber. Recovery of spectral information for systems with more complex geometries would also be more challenging and could benefit by use of probes that contain a greater number of collection fibers, by advances in data reduction algorithms,

and by modifications to the probe geometry itself. Experiments towards realization of these goals and applications to other materials are described in the following chapters.

## Figures

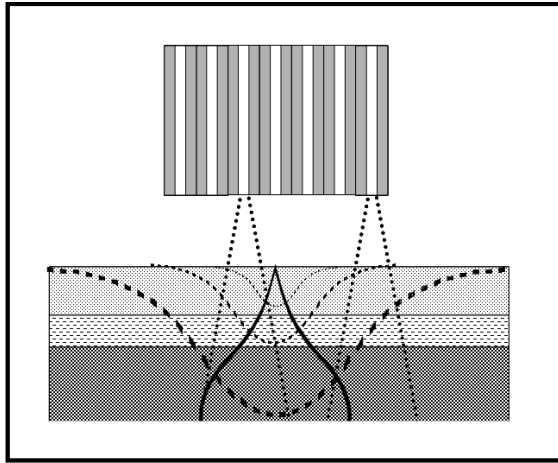


Figure 2.1: Cross-sectional schematic of the photon diffusion effects on light injected at a single point and asymmetric collection efficiency of two fibers located at different distances from the injection point.

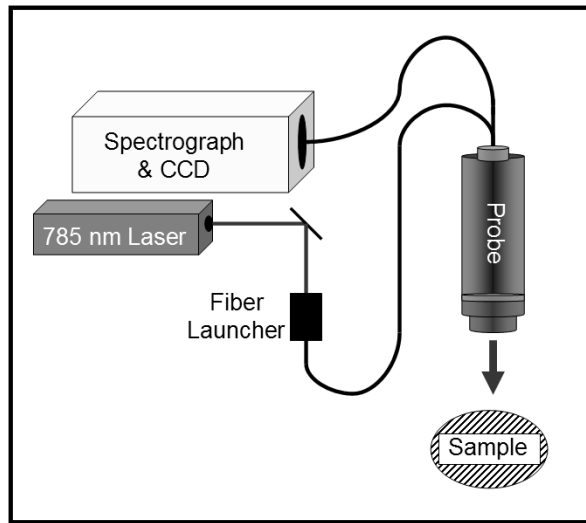


Figure 2.2: Schematic of the experimental apparatus. Components are labeled. Probe is a globally illuminated fiber optic probe with fifty collection fibers in a closely packed circle.

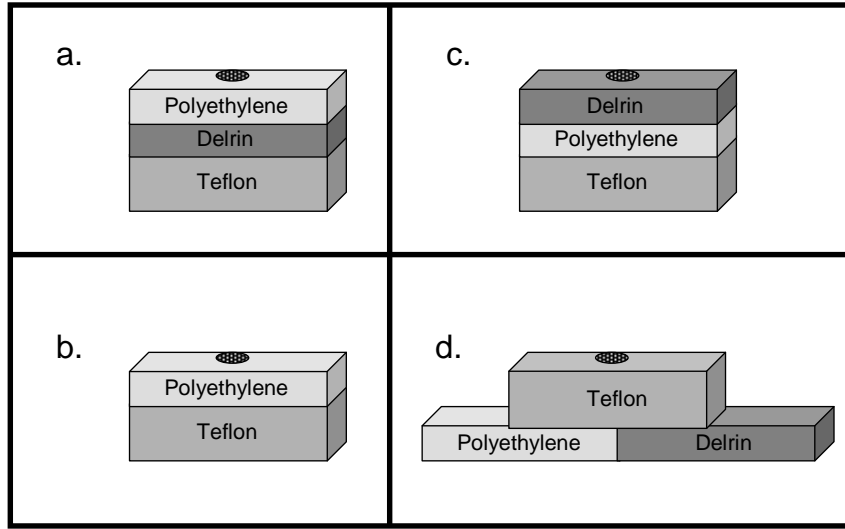


Figure 2.3: Configuration of test systems. Light is incident on the surface of the top layer (shaded circle). (a) system I, three layers (2mm polyethylene, 2mm Delrin, and 13mm Teflon) (b) system II, 5.2 mm polyethylene, 13mm thick block Teflon (c) system III, 5.2 mm thick Delrin, 5.2 mm thick polyethylene, 13mm thick Teflon (d) system IV, subsurface interface, 13mm block of Teflon over 5.2mm thick polyethylene and 5.2mm thick Delrin, illumination centered over boundary.

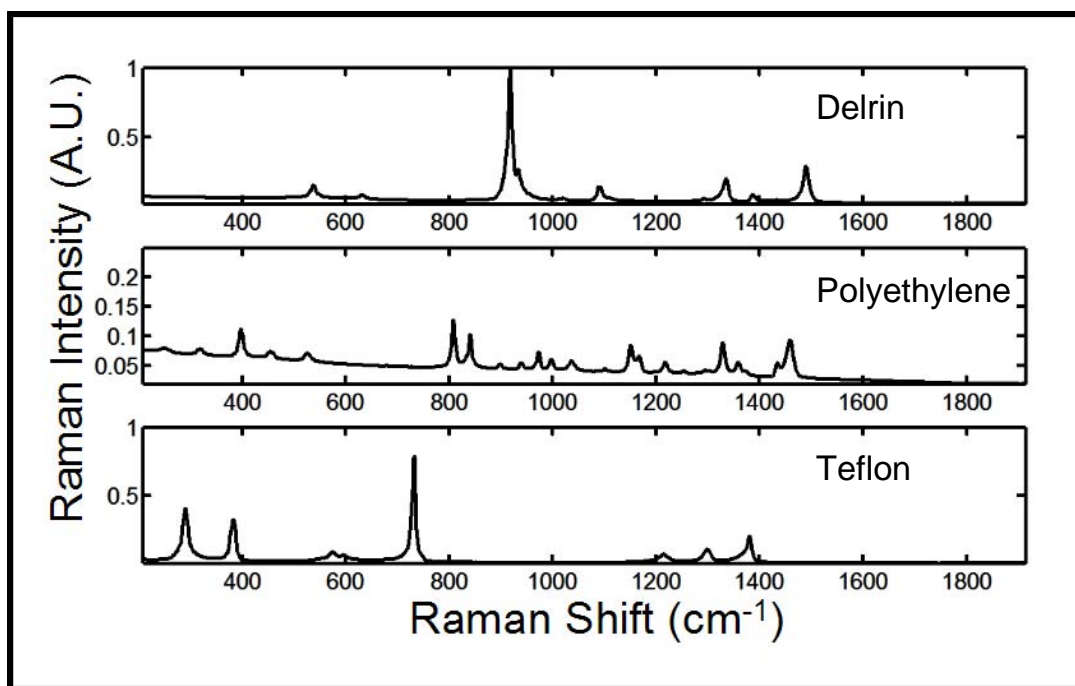


Figure 2.4: Raman spectra of Delrin (top), polyethylene (middle), and Teflon (bottom).

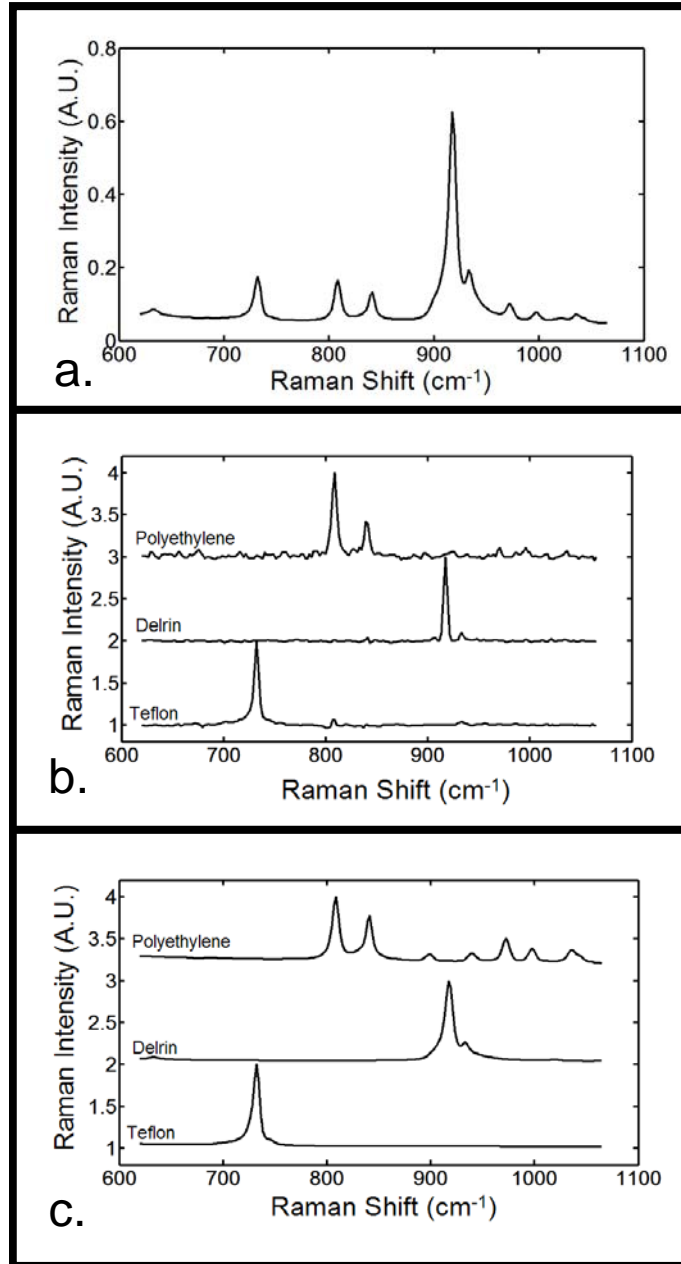


Figure 2.5: (a) averaged Raman spectra of system I (b) recovered BTEM factors of the three components (Top: polyethylene; Middle: Delrin; Bottom: Teflon) (c) Raman spectra of the three components in model system I.



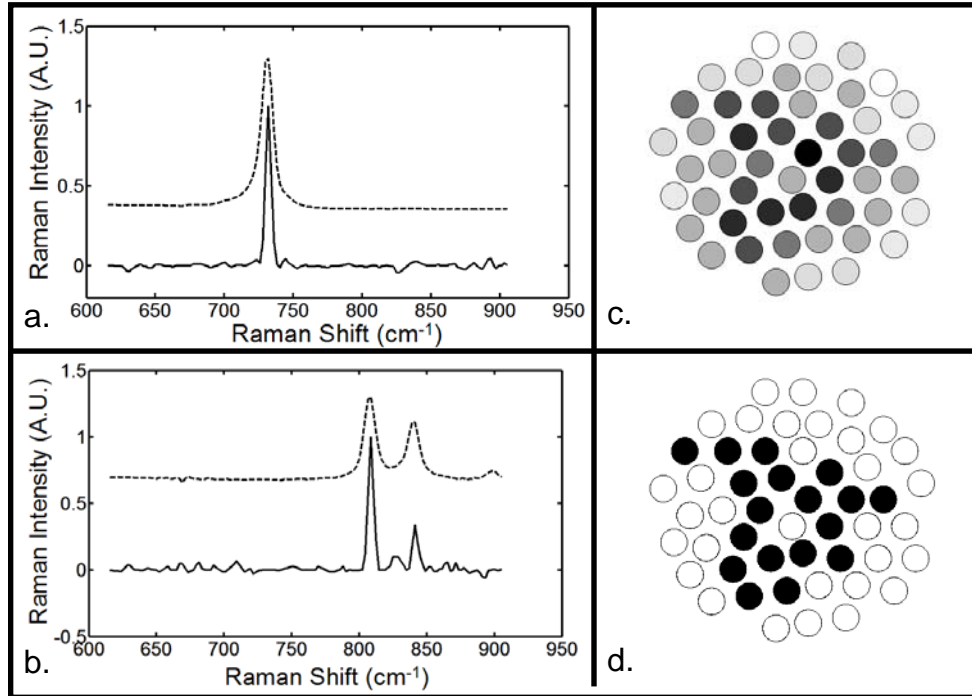


Figure 2.6: (a) BTEM Teflon spectrum (solid line) system II, Teflon spectrum (dashed line) (b) BTEM polyethylene spectrum, reference polyethylene spectrum (dashed line) (c) 8 level gray-scale map. Darker circles represent greater Raman contribution from the surface layers (polyethylene) and the lighter circles represent greater Raman contribution from the subsurface layers (Teflon) (d) 2 level gray-scale map, black circles represent greater Raman contribution from the surface layer (polyethylene) and white circles represent greater Raman contribution from the subsurface layer (Teflon)

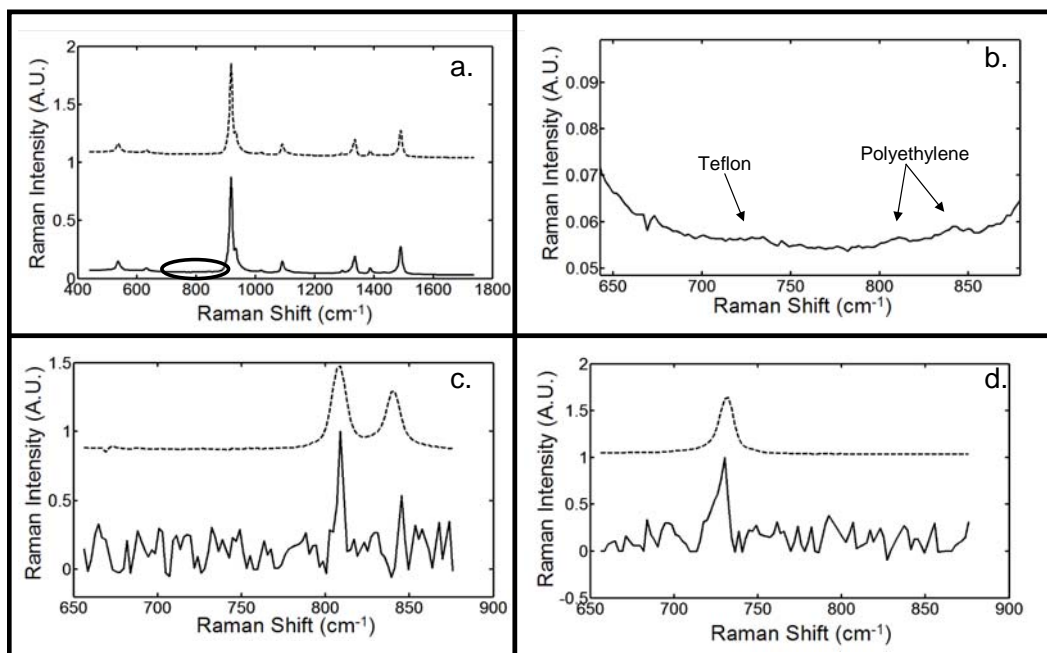


Figure 2.7: (a) solid line the averaged spectrum collected from system III, dashed line a reference spectrum of Delrin (b) detailed image of the circled region in a. (c) solid line BTEM factor for Teflon, dashed line, reference Teflon spectrum (d) solid line the BTEM factor for polyethylene, dashed line polyethylene reference spectrum.

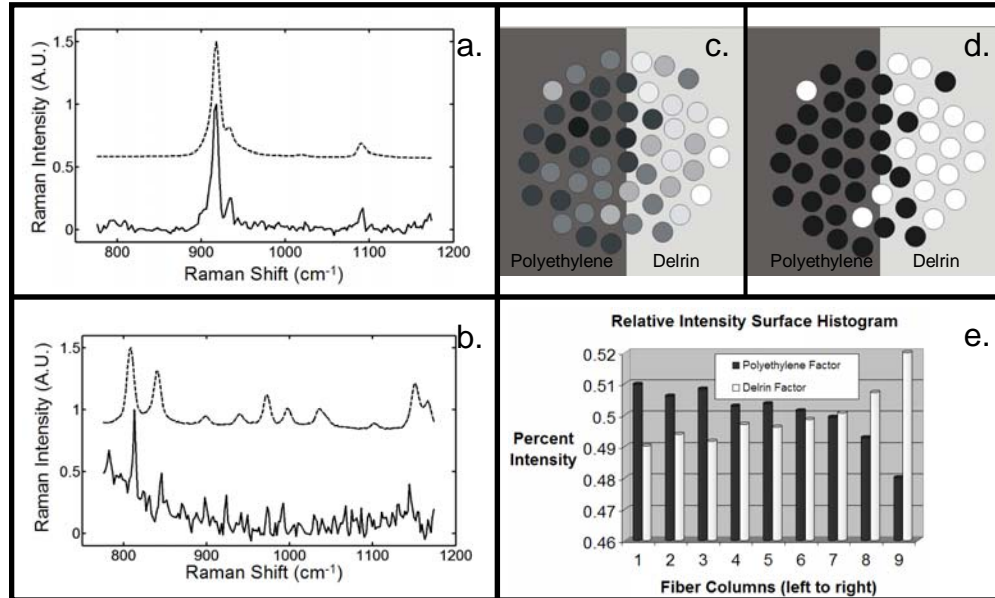


Figure 2.8: (a) solid line BTEM factor for Delrin, dashed line, Delrin reference spectrum (b) solid line BTEM factor for polyethylene dashed line, polyethylene reference spectrum (c) subsurface 8 level gray scale map of polyethylene-Delrin interface beneath 13mm of Teflon, lighter circles contain a greater Delrin Raman contribution, darker circles contain a greater polyethylene Raman contribution (d) subsurface 2 level gray scale map of polyethylene-Delrin interface below 13mm of Teflon. Lighter circles contain a greater Delrin Raman contribution, darker circles contain a greater polyethylene Raman contribution (e) relative intensity surface histogram of the subsurface map.

## References

1. J. Ma and D. Ben-Amotz, "Rapid Micro-Raman Imaging Using Fiber-Bundle Image Compression " *Appl. Spectrosc.* 51(12), 1845-1848 (1997)
2. H. Wikström, I. R. Lewis and L. S. Taylor, "Comparison of Sampling Techniques for In-Line Monitoring Using Raman Spectroscopy," *Appl. Spectrosc.* 59(7), 934-941 (2005)
3. V. Tuchin, *Tissue Optics. Light Scattering Methods and Instruments for Medical Diagnosis*, SPIE Press, Bellingham (2000).
4. T. Vo-Dinh, *Biomedical Photonics Handbook*, CRC Press, Boca Raton (2003).
5. N. Everall, T. Hahn, P. Matousek, A. W. Parker and M. Towrie, "Picosecond time-resolved Raman spectroscopy of solids: Capabilities and limitations for fluorescence rejection and the influence of diffuse reflectance," *Appl. Spectrosc.* 55(12), 1701-1708 (2001)
6. N. Everall, T. Hahn, P. Matousek and A. W. Parker, "Photon migration in Raman spectroscopy," *Appl. Spectrosc.* 58, 591-597 (2004)
7. P. Matousek, N. Everall, M. Towrie and A. W. Parker, "Depth profiling in diffusely scattering media using Raman spectroscopy and picosecond Kerr gating," *Appl. Spectrosc.* 59(2), 200-205 (2005)
8. M. D. Morris, A. E. Goodship, E. R. C. Draper, P. Matousek, M. Towrie and A. W. Parker, "Kerr-gated picosecond Raman spectroscopy and Raman photon migration of equine bone tissue with 400-nm excitation," *Proc. SPIE* 5321, 164-169 (2004)
9. E. R. C. Draper, M. D. Morris, N. P. Camacho, P. Matousek, M. Towrie, A. W. Parker and A. E. Goodship, "Novel assessment of bone using time-resolved transcutaneous Raman spectroscopy," *J. Bone Miner Res.* 20(11), 1968-1972 (2005)
10. M. D. Morris, P. Matousek, M. Towrie, A. W. Parker, A. E. Goodship and E. R. C. Draper, "Kerr-gated Time-resolved Raman Spectroscopy of Equine Cortical Bone Tissue," *J. Biomed. Optics* 10(1), 014014 (2005)

11. P. Matousek, I. P. Clark, E. Draper, M. D. Morris, A. Goodship, N. Everall, M. Towrie, W. F. Finney and A. W. Parker, "Subsurface probing of diffusely scattering media using spatially offset Raman spectroscopy (SORS)," *Appl. Spectrosc.* 59(4), 393-400 (2005)
12. L. Markwort, B. KIp, E. Da Silva and Roussel, "Raman imaging of heterogeneous polymers: A comparison of global versus point illumination," *Appl. Spectrosc.* 49(10), 1411-1430 (1995)
13. W. Windig and J. Guilment, "Interactive self-modeling mixture analysis," *Anal. Chem.* 63(14), 1425 - 1432 (1991)
14. D. Bu and C. W. Brown, "Self-Modeling Mixture Analysis by Interactive Principal Component Analysis," *Appl. Spectrosc.* 54(8), 1214-1221 (2000)
15. A. Garrido Frenich, M. Martinez Galera, J. L. Martinez Vidal, D. L. Massart, J. R. Torres-Lapasió, K. De Braekeleer, J.-H. Wangc and P. K. Hopke, "Resolution of multicomponent peaks by orthogonal projection approach, positive matrix factorization and alternating least squares," *Anal. Chim. Acta* 411, 145-155 ( 2000)
16. E. Widjaja, C. Li and M. Garland, "Semi-Batch Homogeneous Catalytic In-Situ Spectroscopic Data. FTIR Spectral Reconstructions Using Band-Target Entropy Minimization (BTEM) without Spectral Preconditioning," *Organometallics* 21, 1991-1997 (2002)
17. S. Y. Sin, E. Widjaja, L. E. Yu and M. Garland, "Application of FT-Raman and FTIR measurements using a novel spectral reconstruction algorithm," *J. Raman Spectrosc.* 34, 795-805 (2003)
18. L. R. Ong, E. Widjaja, R. Stanforth and M. Garland, "Fourier transform Raman spectral reconstruction of inorganic lead mixtures using a novel band-target entropy minimization (BTEM) method," *J. Raman Spectrosc.* 34, 282-289 (2003)
19. W. Chew, E. Widjaja and M. Garland, "Band-Target Entropy Minimization (BTEM): An Advanced Method for Recovering Unknown Pure Component Spectra. Application to the FTIR Spectra of Unstable Organometallic Mixtures," *Organometallics* 21, 1982-1990 (2002)

20. E. Widjaja, C. Li, W. Chew and M. Garland, "Band-target entropy minimization. A robust algorithm for pure component spectral recovery. application to complex randomized mixtures of six components," *Anal. Chem.* 75(17), 4499-4507 (2003)
  
21. E. Widjaja, N. Crane, T.-C. Chen, M. D. Morris, M. A. Ignelzi and B. R. McCreadie, "Band-Target Entropy Minimization (BTEM) Applied to Hyperspectral Raman Image Data," *Appl. Spectrosc.* 57(11), 1353-1362 (2003)

# CHAPTER III

## TRANSCUTANEOUS RAMAN SPECTROSCOPY OF BONE TISSUE USING A NON-CONFOCAL FIBER OPTIC ARRAY PROBE

### Introduction

There is broad interest in application of Raman spectroscopy for characterization of tissue specimens.<sup>1</sup> For diagnostics and for basic biomedical scientific investigations, it is often desirable to make *in vivo* spectroscopic measurements.<sup>2-9</sup> Where possible these should be non-invasive. Towards this goal, we have demonstrated that transcutaneous bone tissue spectra are obtainable by picosecond time-resolved Raman spectroscopy. Using murine bone tissue specimens taken from sacrificed animals, we have shown that measurements can be made through 1 mm of overlying soft tissue.<sup>10, 11</sup> However, the time-resolved measurements require specialized high power lasers. The instrumentation is expensive and bulky and is available in only a few laboratories worldwide. Penel et. al. have performed *in vivo* Raman spectroscopic measurements in New Zealand rabbits with conventional Raman spectroscopic instrumentation.<sup>3</sup> Fused-silica optical windows were implanted over the calvaria of the rabbits. This methodology is applicable to longitudinal studies in laboratory animals, but is not suitable for measurements on human subjects.

An alternative is to use fiber optic Raman spectroscopy with probes designed to exploit the well-known diffusive effects in light propagation through tissue. One configuration that can be used is spatially offset Raman spectroscopy (SORS).<sup>12, 13</sup> In this configuration, the collection fiber or fibers are spatially offset from the illumination fiber in order to maximize the Raman signal from below the surface of a specimen. This and similar illumination/collection geometries are used in tissue fluorescence and near-infrared absorption spectroscopies.<sup>14, 15</sup>

Recently we have demonstrated that global illumination across the field of view of an array of 50 fibers enables subsurface Raman spectroscopy in highly scattering media.<sup>16</sup> This geometry has the dual advantages of minimizing local power density and generating subsurface Raman maps. We have demonstrated these properties with a commercially available nonconfocal fiber optic probe using blocks of standard engineering polymers as test systems. The employed probe was designed for pharmaceutical applications and has been applied by Wikström et al. to process analysis.<sup>17</sup> In this study we show that global illumination and collection with an array of fibers enables transcutaneous Raman spectroscopy of bone tissue.

## **Experimental**

The Raman system (figure 3.1), comprises a 400 mW 785 nm external cavity diode laser (Invictus, Kaiser Optical Systems, Ann Arbor, MI), a NIR-optimized imaging spectrograph (HoloSpec, f/1.8i, Kaiser Optical Systems) fitted with a 50  $\mu\text{m}$  slit to provide 6-8  $\text{cm}^{-1}$  resolution. The detector was a thermoelectrically cooled deep-depletion



1024x256 pixel CCD (Model DU420-BR-DD, Andor Technology, Belfast, Northern Ireland) operated at  $-75^{\circ}$  C with no binning. The sampling system was a filtered fiber optic probe with uniform global illumination and a bundle of fifty 100  $\mu$ m core collection fibers arranged in a close-packed circle to collect light from the illuminated region (PhAT probe, Kaiser Optical Systems). At the spectrograph end, the collection fibers were arranged in a linear array for coupling into the spectrograph. The probe was fitted with a 75 mm focal length fused silica lens that focused the laser beam to a 3 mm diameter spot. The laser power available at the probe head was 275 mW. The dispersion axis of the spectrograph was calibrated against the neon discharge lamp of a Raman Calibration Accessory (Kaiser Optical Systems). The diffused quartz-halogen lamp light of the Calibration Accessory was used to flat-field the CCD.

In vitro measurements were made on chicken tibia (drumstick) obtained from a local grocery store. The illumination beam from the probe was incident directly on the skin overlaying the distal part of the tibia diaphysis. The integration time was 300 sec. To obtain reference bone spectra, the overlying tissue was excised using a scalpel to expose the bone. An integration time of 50 sec was used to collect reference spectra.

Human tissue measurements were made on cadaveric tissue (Caucasian male, deceased at age 66) obtained through the University of Michigan Medical School Anatomic Donations Program. Measurements were made on the lateral epicondyle at the humerus (elbow). The excised arm was stored at  $-40^{\circ}$  C and allowed to thaw overnight before use. Hair in the area of interest was shaved away prior to collection of spectra. The integration time was 150 seconds. To obtain reference spectra the overlying soft

tissue was excised with a scalpel to expose the bone. No further preparation was employed. The integration time used for exposed bone measurements was 300 seconds.

### **Data Analysis**

All data reduction was performed in Matlab 6.1 (The Mathworks Inc., Natick, MA) using locally written and vendor supplied scripts. The data for each experiment were arrays of 256 Raman spectra collected as single CCD images. Initial preprocessing included dark current subtraction, correction for pixel-pixel response variations, and correction for wavelength response dependence. The response-corrected images were then corrected for slit image curvature caused by the large gathering angle of the spectrograph. An iterative baselining procedure was used to correct for the background fluorescence.<sup>18</sup> The wavenumber region of interest (ROI) was selected to be 500-1295  $\text{cm}^{-1}$  and the covariance matrix was calculated for data in this ROI. Band Target Entropy Minimization (BTEM) was used to obtain the spectral factors of interest. A 50 $\text{cm}^{-1}$  interval, 930-980 $\text{cm}^{-1}$ , was chosen for targeting. The first 65 eigenvectors of the data set were used for the calculation of Raman spectral factors.<sup>19-21</sup>

### **Results and Discussion**

Figure 3.2a shows the reference Raman spectrum exposed bone spectrum and the averaged transcutaneous Raman spectrum at the same location on the diaphysis. The phosphate  $\nu_1$  band at 959  $\text{cm}^{-1}$  is visible in the transcutaneous spectrum, as are collagen

and other protein bands of soft tissue. However, the carbonate band at ca.  $1070\text{ cm}^{-1}$  is not visible in the averaged spectrum. The thickness of the soft tissue at the measurement site was approximately 5 mm. Because the baseline-baseline extent of the phosphate  $\nu_1$  envelope is approximately  $50\text{ cm}^{-1}$  the spectral interval from  $930\text{ cm}^{-1}$  to  $980\text{ cm}^{-1}$  was targeted for BTEM bone spectrum recovery from transcutaneous data sets. The recovered spectrum (BTEM) from the row-by-row CCD data is shown in figure 3.2b. The spectrum reproduces the spectrum of the exposed bone well, even though the measurement is made through 5 mm of soft tissue.

In figure 3 the spectrum over the  $500\text{ -}1300\text{ cm}^{-1}$  region is shown. This region is important because it contains the phosphate  $\nu_4$  envelope centered at ca.  $583\text{ cm}^{-1}$ , proline and hydroxyproline bands in the  $850\text{ -}900\text{ cm}^{-1}$  and amide III in the  $1230\text{ -}1290\text{ cm}^{-1}$  region. Figure 3.3 offers further confirmation that the mineral spectrum is accurately recovered from the fiber optic probe data. However, the spectra also reveal that recovery of the matrix spectrum is more difficult through tissue this deep. Proline and hydroxyproline bands are just visible, but not quantifiable. Amide III is not reliably detected.

In figure 3.4 we show data obtained at the lateral epicondyle at the humerus of a human cadaver. Figure 3.4a shows an overlay of the reference exposed bone Raman spectrum (dotted line) with the average of the spectra collected transcutaneously by the 50 collection fibers. In the averaged transcutaneous spectrum the phosphate  $\nu_1$  band at  $960\text{ cm}^{-1}$  is visible, although obscured by the bands of the overlying tissue. At the measurement site the bone lies below about 3 mm of soft tissue. In the human tissue the tendons, which scatter light strongly, are thicker than in the chicken specimen.

Additionally, the human skin was visibly more heavily pigmented than the chicken skin, resulting in a higher melanin fluorescence background. Despite these complications, we were able to recover the bone spectrum from the transcutaneous measurements, as shown in figure 3.4b. The mineral component of transcutaneous spectrum accurately follows the exposed bone spectrum with the additional noise expected for the weaker bone signal. In the recovered spectrum even the proline, hydroxyproline and amide III bands are well-reproduced.

### **Conclusions**

We have shown that a probe design that utilizes global illumination and an array of collection fibers that interrogates the illuminated region can recover transcutaneous bone spectra. The probe design has the advantage of low power density. The 785 nm laser wavelength available to us is lower than the 830 nm wavelength more commonly used for tissue studies. We expect slightly increased penetration depth and reduced fluorescence background when we move to a longer wavelength.

Even at this early stage, it is clear that transcutaneous bone Raman spectroscopy can readily be adapted to use in living human and animal tissue. This development would enable longitudinal studies on living animals, thereby reducing the number of animals required for a study. We have recently proposed a candidate Raman biomarker for susceptibility to osteoporotic damage.<sup>22</sup> Upon validation of this biomarker, the potential exists for rapid Raman spectroscopic diagnosis of fracture susceptibility in osteoporosis

victims. Extension to this and other applications in musculoskeletal studies is an exciting prospect.

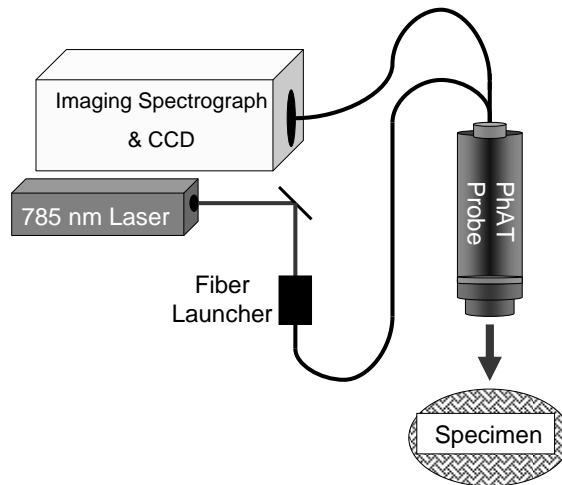


Figure 3.1: Schematic of the experimental apparatus. Components are labeled. The probe is a globally illuminated fiber-optic probe with 50 collection fibers in a closely packed circle.

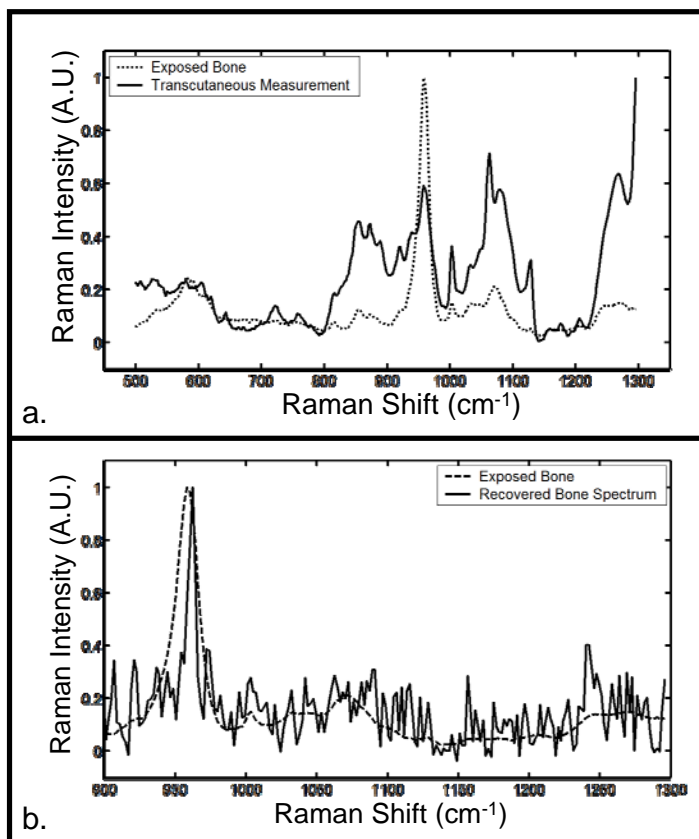


Figure 3.2: Raman spectra of chicken tibia (distal-diaphysis). (a) The spectrum collected by the fiber probe averaged over all 50 collection fibers. The solid line trace is the transcutaneous spectrum and the dotted line is the exposed bone spectrum. (b) Recovered bone tissue factor transcutaneous measurement (solid line) and the exposed bone spectrum (dashed line).

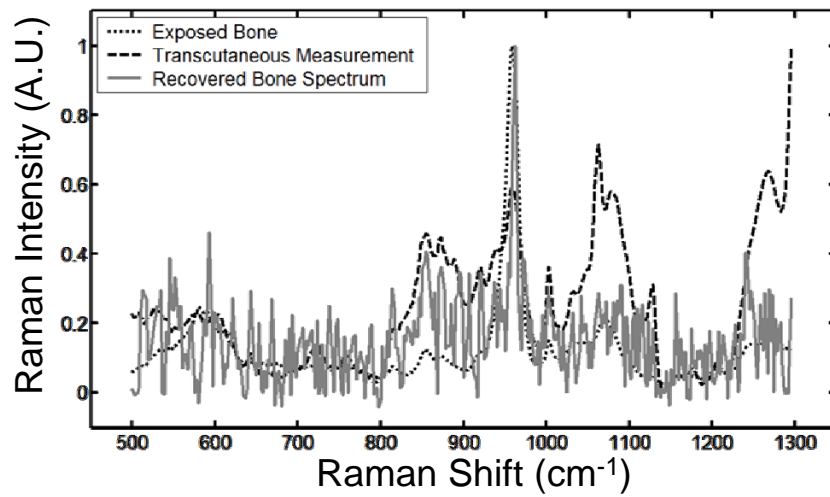


Figure 3.3: Raman spectra of chicken tibia with the averaged spectrum from the 50 probe collection fibers. Transcutaneous spectrum (dashed line), exposed bone (dotted line), and bone spectrum redovered from transcutaneous measurements (solid line).



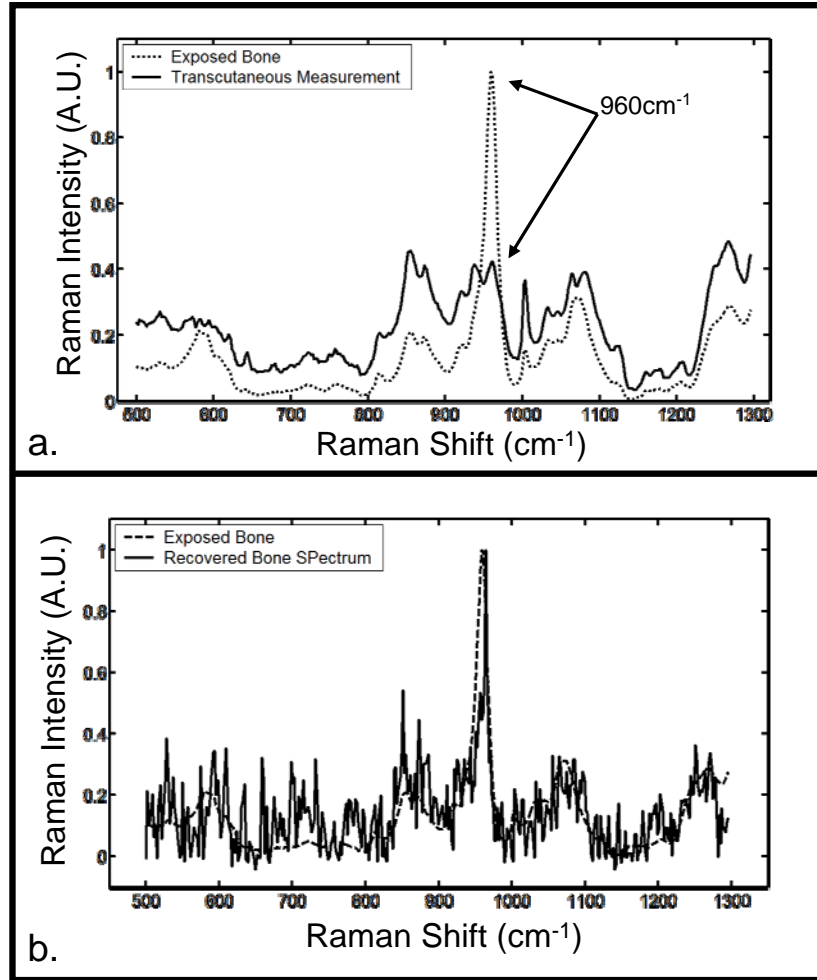


Figure 3.4: Raman spectra of the lateral epicondyle at the humerus. (a) the spectrum collected by the fiber probe averaged over all 50 collection fibers. The solid line trace is the transcutaneous spectrum and the dotted line is the exposed bone spectrum. (b) Recovered bone tissue factor transcutaneous measurement (solid line) and the exposed bone spectrum (dashed line).

## References

1. T. Vo-Dinh, Biomedical Photonics Handbook, CRC Press, Boca Raton (2003).
2. I. V. Ermakov, M. R. Ermakov and W. Gellermann, "Simple Raman Instrument for in Vivo Detection of Macular Pigments," Appl. Spectrosc. 59(7), (2005)
3. G. Penel, C. Delfosse, M. Descamps and G. Leroy, "Composition of bone and apatitic biomaterials as revealed by intravital Raman microspectroscopy," Bone 36(5), 893-901 (2005)
4. Z. Huang, H. Lui, D. McLean, Korbelik and H. Zeng, "Raman Spectroscopy in Combination with Background Near-infrared Autofluorescence Enhances the In Vivo Assessment of Malignant Tissue," Photochemistry and Photobiology 81, 1219-1226 (2005)
5. S. Kolijenic, T. Schut, A. Vincent, J. Kros and G. Puppels, "Detection of Meningioma in Dura Mater by Raman Spectroscopy," Anal. Chem. 77, 7958-7965 (2005)
6. L. Santos, R. Wolthuis, S. Kolijenic, R. Almeida and G. Puppels, "Fiber-Optic Probes for In-Vivo Raman Spectroscopy in the High-Wavenumber Region," Anal. Chem. 77, 6747-6752 (2005)
7. Z. Huang, H. Lui, X. K. Chen, A. alajilan, D. McLean and H. Zeng, "Raman spectroscopy of *in vivo* cutaneous melanin," J. Biomed. Optics 9(6), 1198-1205 (2004)
8. J. T. Motz, M. Hunter, L. H. Galindo, J. A. Gardecki, J. A. Kramer, R. R. Dasari and M. S. Feld, "Optical fiber probe for biomedical Raman spectroscopy," Appl. Optics 43(5), 542-554 (2004)
9. P. J. Caspers, G. W. Lucassen and G. J. Puppels, "Combined In Vivo Confocal Raman Spectroscopy and Confocal Microscopy of Human Skin," Biophysical Journal 85, 572-580 (2003).
10. E. R. C. Draper, M. D. Morris, N. P. Camacho, P. Matousek, M. Towrie, A. W. Parker and A. E. Goodship, "Novel assessment of bone using time-resolved transcutaneous Raman spectroscopy," J. Bone Miner Res. 20(11), 1968-1972 (2005)

11. M. D. Morris, E. Draper, A. E. Goodship, P. Matousek, M. Towrie, A. W. Parker and N. Camacho, "Picosecond time-gated Raman Spectroscopy for transcutaneous evaluation of bone composition," *Proc. SPIE* 5693, 344-350 (2005)
12. P. Matousek, I. P. Clark, E. R. C. Draper, M. D. Morris, A. E. Goodship, N. Everall, M. Towrie, W. F. Finney and A. W. Parker, "Subsurface Probing in Diffusely Scattering Media Using Spatially Offset Raman Spectroscopy," *Applied Spectroscopy* 59(4), 393-400 (2005)
13. P. Matousek, M. D. Morris, N. Everall, I. P. Clark, M. Towrie, E. Draper, A. Goodship and A. W. Parker, "Numerical Simulations of Subsurface Probing in Diffusely Scattering Media Using Spatially Offset Raman Spectroscopy," *Appl. Spectrosc.* 59(12), 1485-1492 (2005)
14. T. J. Pfefer, K. T. Schomacker, M. N. Ediger and N. S. Nishioka, "Multiple-fiber probe design for fluorescence spectroscopy in tissue," *Appl. Opt.* 41(22), 4712-4721 (2002)
15. E. L. Hull, M. G. Nichols and T. H. Foster, "Localization of luminescent inhomogeneities in turbid media with spatially resolved measurements of cw diffuse luminescence emittance," *Appl. Opt.* 37(13), 2755-2765 (1998)
16. M. V. Schulmerich, W. F. Finney, R. A. Fredericks and M. D. Morris, "Subsurface Raman Spectroscopy and Mapping Using a Globally Illuminated Non-Confocal Fiber-Optic Array Probe in the Presence of Raman Photon Migration," *Appl. Spectrosc.* 60(2), 109-114 (2006)
17. H. Wikström, I. R. Lewis and L. S. Taylor, "Comparison of Sampling Techniques for In-Line Monitoring Using Raman Spectroscopy," *Appl. Spectrosc.* 59(7), 934-941 (2005)
18. C. A. Lieber and A. Mahadevan-Jansen, "Automated method for subtraction of fluorescence from biological Raman spectra," *Appl. Spectrosc.* 57(11), 1363-1367 (2003)
19. E. Widjaja, N. Crane, T. Chen, M. D. Morris, M. A. Ignelzi Jr. and B. McCreadie, "Band-Target Entropy Minimization (BTEM) Applied to Hyperspectral Raman Image Data," *Appl Spectrosc.* 57(11), 1353-1362 (2003)
20. E. Widjaja, C. Li and M. Garland, "Semi-Batch Homogeneous Catalytic In-Situ Spectroscopic Data. FTIR Spectral Reconstructions Using Band-Target Entropy

Minimization (BTEM) without Spectral Preconditioning," *Organometallics* 21, 1991-1997 (2002)

21. W. Chew, E. Widjaja and M. Garland, "Band-Target Entropy Minimization (BTEM): An Advanced Method for Recovering Unknown Pure Component Spectra. Application to the FTIR Spectra of Unstable Organometallic Mixtures," *Organometallics* 21, 1982-1990 (2002)

22. B. R. McCreadie, M. D. Morris, T.-C. Chen, D.S.Rao, W. F. Finney, E. Widjaja and S. A. Goldstein, "Bone Extracellular Matrix Compositional Differences in Women with and without Osteoporotic Fracture," *Bone* 39, 1190-1195 (2006)

**CHAPTER IV**

**TRANSCUTANEOUS RAMAN SPECTROSCOPY OF BONE:  
GLOBAL SAMPLING VS. RING/DISK FIBER OPTIC PROBES**

**INTRODUCTION**

The role of diffusive light transport in highly scattering systems is widely applied to biomedical optics,<sup>1, 2</sup> but was not fully appreciated by the Raman community until recently.<sup>3-5</sup> Typically, strategies use geometries in which the detector is displaced from the direction of propagation of the source light, to account for the spreading of the light beam.<sup>6-8</sup> Similar configurations have only recently been used in Raman spectroscopy. This approach was first systematically studied by Matousek et. al. using layers of powdered materials as model systems, and Monte Carlo simulations with a simple diffusional model to explain the experimental results.<sup>9, 10</sup> A point illumination source and a point detector spatially offset from the source were used in the first experiments. Our group introduced illumination with a defocused laser beam and a circular array of collection fibers whose field of view matched the diameter of the beam incident on the specimen. A defocused laser beam, called global illumination in our earlier publications, reduced the possibility of thermal damage to the specimen while the coincident laser illumination area and collection fiber field of view were exploited to generate subsurface component maps.<sup>11</sup> Multivariate data analysis was used to extract the spectra of

subsurface components and to map their distribution. This was accomplished using blocks of polymers as model systems; mapping through several millimeters of Teflon was demonstrated. We later reported transcutaneous Raman spectroscopy of human cadaveric bone using the same experimental configuration.<sup>12</sup>

Here we describe a more efficient probe configuration. In order to distribute laser power and minimize both the skin Raman spectra and skin fluorescence, we have used annular illumination and collection with a circular array of fibers centered inside the annulus; an approach we now call ring/disk Raman spectroscopy.<sup>13</sup> A very similar optical configuration was independently demonstrated by Matousek.<sup>14</sup> To a good first approximation, the annulus can be treated as a line for heat dissipation purposes. It is known that for a given absolute laser power, line focus provides more efficient heat dissipation than either tight spot focus or a defocused circular beam.<sup>15</sup> Thus the ring/disk configuration provides the benefits of a relatively intense Raman spectrum from high laser power and selectivity towards the subsurface components because of the distance between the illumination region and the collection region. Ring illumination is easily implemented with an axial conical lens (axicon) and a converging lens. With inclusion of telephoto optics the distance between the illumination annulus and the light collection disk is easily varied, making ring illumination useful for subsurface Raman measurements in most light scattering systems.

Here we first demonstrate transcutaneous Raman spectroscopy on rat and chicken tissue using the ring/disk probe.<sup>16</sup> We then compare the strengths of global illumination/collection and ring/disk geometries. Polymer blocks are used as a model

system and transcutaneous performance with increasing ring/disk spacing is demonstrated using chicken tibiae.

### **Preliminary measurements using the Ring/disk probe**

Figure 4.1 is a schematic of the fiber probe. A 785 nm diode laser (Invictus, Kaiser Optical Systems, Ann Arbor) is focused into a 100  $\mu\text{m}$  core fused silica fiber, which is collimated at its distal end and focused into a fused silica axicon (cone angle 179.5°, Delmar Photonics, San Diego CA). A plano-convex fused silica singlet and a negative focal length fused silica meniscus or plano-concave singlet are used to focus the beam to an annulus. A dichroic mirror is used to align the annulus to the field of view of the collection fiber array (PhAT probe, Kaiser Optical Systems). The illumination assembly is mounted on the distal end of the PhAT probe using modular lens tubes and connectors (Thorlabs, Newton, NJ). The PhAT probe output is presented to an imaging spectrograph (HoloSpec, Kaiser Optical Systems). The dispersed Raman scatter is imaged onto a detector (Andor Classic, Andor Technologies, Belfast, UK) fitted with a 1024x256 back-illuminated deep depletion CCD and analyzed by band target entropy minimization (BTEM) as described previously.<sup>13</sup> Band heights and ratios were calculated in GRAMS/AI (Thermo Galactic, Madison, WI). At the probe head the laser beam was approximately 110 mW (chicken) and 170 mW (rat).

Three model tissues were employed. Sprague-Dawley rat tibiae and femora were used to study integration time dependence. Chicken tibiae from a local supermarket were used to study depth penetration. Depilatory lotion was used to remove hair from the rat

skin. Tissues were treated with an optical clearing agent, glycerol, for approximately 1 minute before the start of each experiment.

Rat tissue measurements were made at an overlying skin thickness of approximately 1 mm. Integration times between 5 sec and 120 sec were used for measurement time studies. Chicken tibia measurements were made with integration time 120 sec and with bone at depths of approximately 2 mm and 4 mm below the skin. For all tissue specimens, after a sequence of measurements was completed, the overlying tissue was removed with a scalpel and Raman spectra of the exposed bone were collected with the PhAT probe.

Figure 4.2 shows recovered rat tibia spectra as a function of integration time. The spectra are presented as recovered by BTEM without digital filtering or smoothing. The mineral spectrum recovery is good above about 30 sec. The intense phosphate  $\nu_1$  band is visible, though distorted, even at integration times as low as 5 sec. As table 4.1 shows, it is possible to obtain reasonable agreement of carbonate/phosphate ratios between measurements made on exposed bone and measurements through 1 mm of skin at integration times of 30 sec or longer. Best results are obtained at 120 sec integration time. However, as even visual inspection of the spectra shows, BTEM did not completely separate the skin spectrum from the bone spectrum. Amide III and the  $\text{CH}_2$  bending mode at ca.  $1446 \text{ cm}^{-1}$  are about four times larger in the recovered spectra than in the spectrum of exposed bone. The incomplete separation results from oversampling the skin spectrum. In these experiments the annulus outer and inner diameters were about 7 mm and 6 mm and the collection fiber field of view about 3 mm. It was not possible with the available optics to generate a collection fiber field diameter much below 3 mm. Increasing the



annulus i.d. to larger than 7 mm in order to reduce the contribution from skin caused a large fraction of the laser light to miss the tibia entirely.

We collected spectra of chicken tibiae using the same excitation annulus. Figure 4.3 shows the recovered spectra (120 sec integration time) together with the corresponding exposed bone spectra at a depth of 4 mm. Also shown in Fig. 3 is the average spectrum (dotted line) collected by the probe. As in figure 4.2, the spectra have not been smoothed or filtered. Figure 4.3a, shows the effect of using all 50 collection fibers for BTEM calculations. Comparison of the recovered spectrum with the exposed bone spectrum (dotted line) shows incomplete separation of the bone factor from the overlying tissue spectrum. The problem is most easily visible as the erroneously high intensity of the  $\text{CH}_2$   $1446\text{cm}^{-1}$  band. If the outer ring of 18 collection fibers is excluded from the calculation, the recovery of the bone factor is improved (figure 4.3b) because the operation is equivalent to increasing the distance between excitation annulus and collection fibers. The signal/noise ratio is not improved because the number of spectra included in the calculation is reduced. As table 4.1 shows, at 4 mm depth, the error in measurement of carbonate/phosphate is acceptable (11.8%) when all the collection fibers are used in the data analysis. The error is reduced to 7.6% when data from the outer ring of 18 collection fibers is not used. On the other hand, at 2 mm depth, better results are obtained when data from all fibers are included in the BTEM calculation.

These preliminary results can be substantially improved by optimization of the design based on realistic modeling of the tissue optics of these complex skin, bone and connective tissue systems. However, the results seen in figure 4.3 indicate varying depth resolutions based on the spacing between the illumination and collection region. In the

second part of this chapter we systematically investigate the affect of changing the ring/disk spacing and compare the ring/disk probes performance to that of the global illumination probe.

### **Experimental Method and Data Treatment**

Blocks of polymers were used as a model system to demonstrate the subsurface Raman mapping capabilities of the global illumination and ring/disk probe geometries. Delrin, polyethylene, and Teflon were machined into 51mm x 51mm slabs of known thicknesses. Teflon blocks were stacked to the desired height above slabs of Delrin and polyethylene. The Delrin and polyethylene were arranged so that the boundary between them lay approximately in the center of the field of view of the collection fibers. The illumination annulus diameter and distance to the collection circle are shown in table 4.2. Teflon outer layers of 0.0-7.2 mm were systematically varied. The data acquisition time was 60 sec.

Transcutaneous spectra were obtained from chicken tibiae purchased from a local market. Glycerol was applied as an optical clearing agent. The illumination beam from the probe was incident directly on the skin overlying the distal end of the diaphysis. The integration time was 120 sec. To obtain reference bone spectra, the overlying tissue was excised using a scalpel to expose the bone. An integration time of 60 sec was used to collect reference spectra. Experiments were performed with ring diameters and ring-disk spacing as shown in table 4.2. Data sets from all five spacings were combined in order to extract bone Raman spectra.

All data reduction was performed in Matlab 6.1 (The Mathworks Inc., Natick, MA) using locally written and vendor supplied scripts. The data for each experiment were arrays of 256 Raman spectra collected as single CCD images. Initial preprocessing included dark current subtraction, correction for pixel-pixel response variation, and correction for wavelength response dependence. The response-corrected images were then corrected for slit image curvature caused by the large gathering angle of the spectrograph. A Blackman-Harris windowing function was applied to each spectrum to remove high frequency noise.<sup>17</sup> Each fiber at the slit illuminated five pixels. To eliminate cross-talk, only data from the central three fibers were used. The retained data from each fiber was co-added to yield a fifty spectrum data set for each acquisition.

Both global illumination/collection and ring/disk measurements were made on the polymer system. The ring/disk offset spacing was 2.5 mm. To minimize noise contributions, a region of interest that contained Raman bands for each of the polymer samples was selected to be used for further processing. The covariance matrix was calculated. The factors were normalized so that the sum of the scores for a given fiber was unity. Score plots for Delrin and polyethylene were generated from the eigenvectors. The relative intensity plots were then mapped onto a spatial representation of the fiber collection array.

For the chicken tibial data, an iterative baselining procedure with a fifth order polynomial was used to correct for the background fluorescence<sup>18</sup>. A wavenumber region of interest (ROI) was selected to include both mineral and matrix bands. The datasets for all five ring/disk offsets were combined and a covariance matrix was

calculated for data in the ROI. With the global illumination system, five 2 minute acquisitions were combined into a single data set to match the 10 minute data acquisition used with the ring/disk system. Band target entropy minimization (BTEM)<sup>19-23</sup> was used to obtain the spectral factors of interest for each data set. A 6 cm<sup>-1</sup> interval, 956-962cm<sup>-1</sup>, was chosen for targeting. The first 25 eigenvectors of a global illumination data set were used for the calculation of Raman spectral factor. Five eigenvectors were used for the ring/disk data. The numbers of eigenvectors were based on visual inspection of the Score plot of eigenvalues for each covariance matrix.

## **Results and Discussion**

The subsurface mapping performance of each probe is illustrated in figure 4.4. In the global illumination (top row) experiments we used a 3 mm diameter illumination disk and collection spot. In our earlier work a 7 mm diameter spot and disk were used. As a consequence of the small spot and disk size, the depth penetration is less than we have previously reported, but the measurement time is reduced because of a higher power density. Mapping is accurate only to about 2.4 mm below the Teflon surface. Global illumination yields a larger surface component in the acquired spectra because the illumination and collection regions overlap. The net effect of global illumination is less subsurface signal than observed for geometries in which there is no overlap between the illuminated region and the collection fibers. This phenomenon is illustrated by the ring/disk data in the second row of figure 4.4. With the same 3 mm collection disk, but a

2.5 mm spacing between the inner edge of the ring and the outer edge of the collection disk. Accurate mapping is obtained to depths of 5-6 mm.

These data, together with our already published results, illustrate the importance of controlling illumination and collection geometries to achieve the desired trade-off between measurement and depth at which signal is recovered. In these experiments limited depth is accepted as the cost of faster data acquisition.

Data obtained for the chicken tibia model system are shown in figure 4.5. Results obtained both with the global illumination/collection probe and the ring/disk probe are presented. The ring/disk probe was operated with 5 different ring/disk spacings (table 4.2). The average spectra acquired for each probe configuration are shown in figure 4.5a. The same intensity scale is used throughout to illustrate the decrease in signal intensity with increasing spacing. The included global illumination data shows that this configuration provides the greatest total signal intensity because the illumination and collection region fully overlap. Illumination with ring 1 (figure 4.5a) provides the second largest intensity because the spacing between the illumination annulus and collection disk is the smallest. The signal intensity decreases as the ring/disk spacing increases.

Just as importantly, however, the background fluorescence (figure 4.5b) is most intense with global illumination. It is smaller in the ring/disk data and decreases with increasing ring/disk spacing. The fluorescence background in the global illumination/collection has greater and more complex curvature than the background fluorescence in the ring/disk Raman spectra. With deep red or NIR illumination the most important source of fluorescence is melanin. Most melanin is in the melanocytes located in the epidermis, close to the surface. In humans and other mammals the melanocytes lie

just below the stratum corneum. Because the fluorescence source is so close to the surface, separation of the illumination and collection regions will decrease its contribution to the total collected signal.

The subsurface selectivity of the ring/disk probe is illustrated in figure 4.5c. The fitted backgrounds (figure 4.5b) have been subtracted from the raw spectra of figure 4.5a. Comparison of these signals show that the bone contribution (e.g. phosphate  $\nu_1$ , dotted line at  $959\text{ cm}^{-1}$ ) becomes an increasingly larger component of the signal. It is barely visible over the collagen contributions in the global illumination spectra (bottom trace), but is easily seen in the spectra with large ring/disk spacing.

The recovered (BTEM) bone Raman spectral factors for the global illumination/collection fiber optic probe and the ring/disk probe are shown in figure 4.6. For the specimen of figure 4.5 and 4.6 the periosteal surface of the bone lay beneath about 4.3 mm skin and soft tissue. The soft tissue included skin, facia, muscle, blood vessels and tendons. As can be seen in the figure, with global illumination (top trace) only phosphate  $\nu_1$  ( $959\text{ cm}^{-1}$ ) is recovered with a high enough signal/noise ratio to provide useful information. Even at this depth the ring/disk probe yields not only phosphate information but also the carbonate  $\nu_1$  band at  $1070\text{ cm}^{-1}$ . The ring/disk configuration provides better recovery of subsurface bone spectra at this depth.

## Conclusions

For transcutaneous Raman spectroscopy, the ring/disk fiber optic probe provides the benefits of good depth penetration and the ability to supply sufficient laser power to

allow acquisition of Raman spectra at moderate collection times. Further improvement is possible by optimizing the illumination and collection optics. As the ring/disk spacing increases, the thickness of the illumination ring increases. From a heat transport point of view, a thin ring is desirable, so that heat dissipation proceeds efficiently in all directions perpendicular to the circumference of the ring. More sophisticated telephoto designs than the Galilean telescope can provide the necessary thin rings located further away from the collection disk than is currently possible. Of course, laser power can be increased beyond the 230-270 mW incident power that is available from our current laser. Further improvement in spectral recovery is likely with illumination at 830 nm, because of the reduced fluorescence observed at that wavelength.

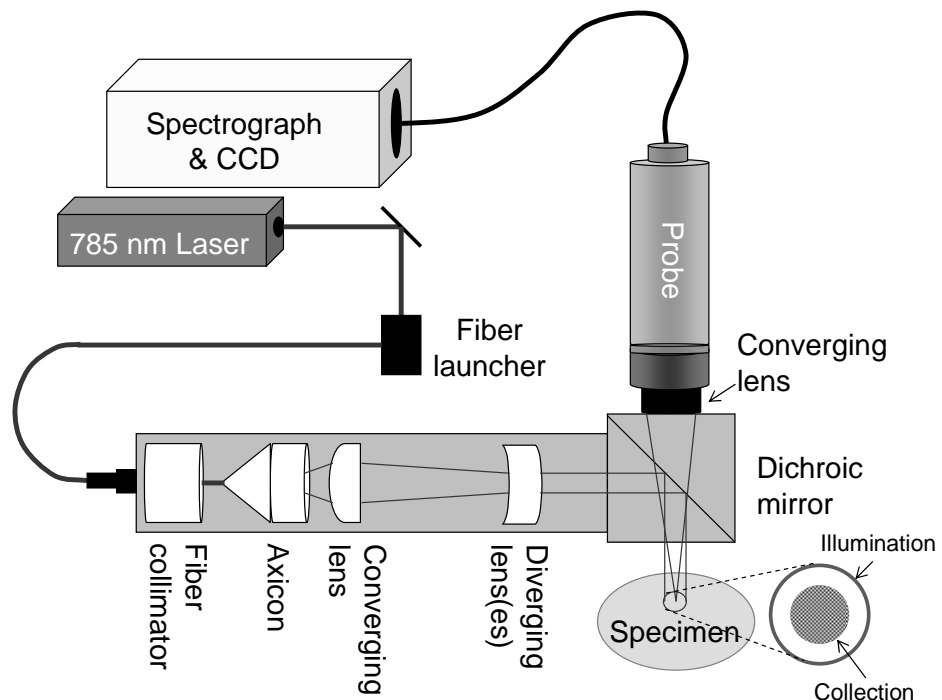


Figure 4.1: Schematic of fiber optic Raman system. The components are as marked in the figure. Lenses of different focal lengths were used to adjust dimensions of illuminating annulus as needed. The drawing is not to scale.



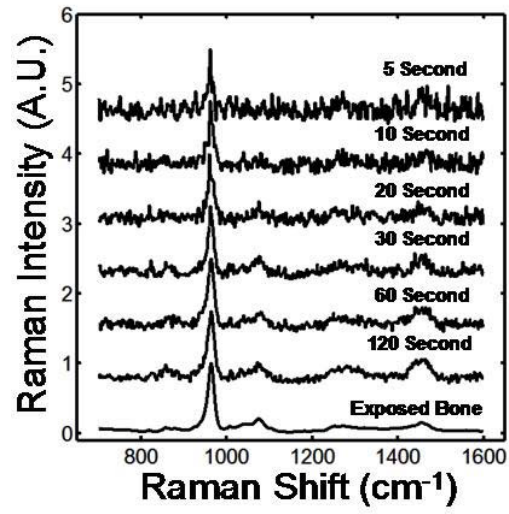


Figure 4.2: Transcutaneous Raman spectra of rat tibia. The spectrum integration times are shown on the figure. The bands are: phosphate, 958 cm<sup>-1</sup>; carbonate, 1070 cm<sup>-1</sup>; amide III, 1240-1270 cm<sup>-1</sup>; matrix CH<sub>2</sub> deformation, 1446 cm<sup>-1</sup>.

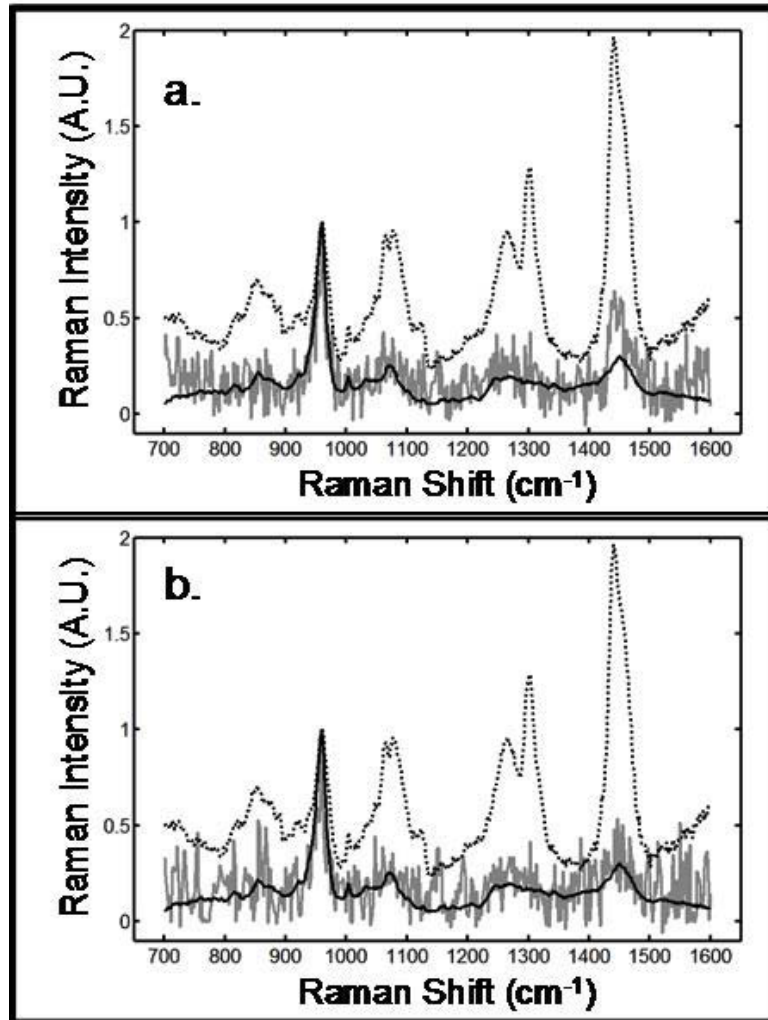


Figure 4.3: Measurements made through 4mm of overlying tissue on a chicken tibia at the mid diaphysis. Transcutaneous (dotted), recovered bone factor (gray), exposed bone (black). (a) recovered bone factor using data from all 50 collection fibers. (b) recovered bone factor using data from the 32 innermost collection fibers.

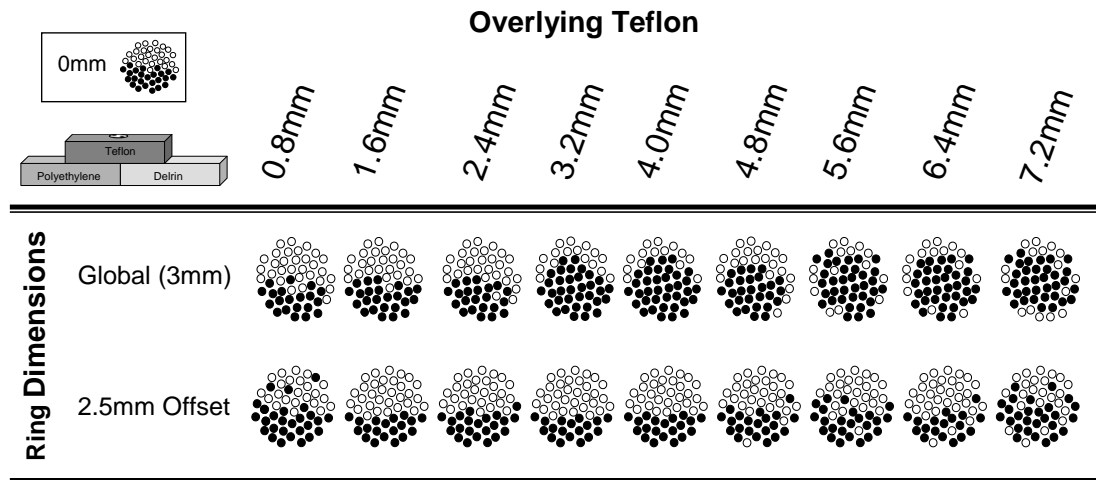


Figure 4.4: Subsurface mapping performance for each probe: Subsurface maps of polyethylene/Delrin interface acquired from global illumination/collection probe (top row) and ring/disk illumination/collection (bottom row) at different overlying Teflon thicknesses. The Polymer model system is shown in the upper left corner.

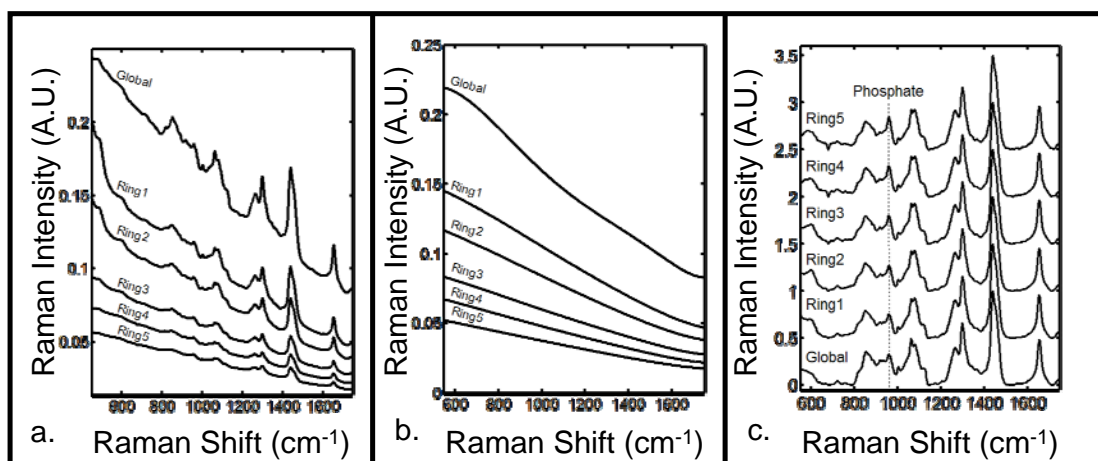


Figure 4.5: Raman spectra of chicken tibia (distal-diaphysis). (a) The mean spectra acquired by the global illumination/collection probe and the ring/disk probe operated at five different ring/disk separations (traces labeled). (b) The average background resulting from the different illumination/collection geometries for each probe. (c) The normalized and baselined mean transcutaneous spectra for each probe configuration.

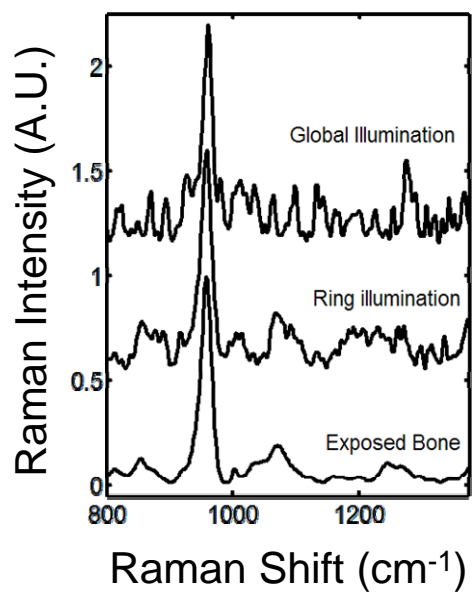


Figure 4.6: Recovered (BTEM) bone factor for the global illumination/collection probe (top trace), ring/disk probe using a combined data set (middle trace), and averaged exposed bone measurement (bottom trace).

<b>Specimen</b>	<b>Depth (mm)</b>	<b>Acquisition Time (sec)</b>	<b>Carbonate to Phosphate ratio</b>	<b>% error</b>
Rat Tibia	0	60	0.215 <sup>a</sup>	
	1	120	0.220 <sup>b</sup>	2.3%
	1	60	0.201 <sup>b</sup>	-6.6%
	1	30	0.236 <sup>b</sup>	9.6%
	1	20	0.250 <sup>b</sup>	16.4%
	1	10	0.098 <sup>b</sup>	-54.3%
	1	5	NA	NA
Rat Femur	0	60	.222 <sup>a</sup>	
	2	120	.210 <sup>b</sup>	-5.4%
Chicken Tibia	0	60	.225 <sup>a</sup>	
	2	120	.214 <sup>b</sup>	-4.9%
	2	120	.133 <sup>c</sup>	-40.9%
Chicken Tibia	0	60	.202 <sup>a</sup>	
	4	120	.226 <sup>b</sup>	11.8%
	4	120	.218 <sup>c</sup>	7.6%
<sup>a</sup> Calculated as height ratio of 1070 cm <sup>-1</sup> to 958 cm <sup>-1</sup> bands				
<sup>b</sup> Ratio calculated using data from all collection fibers				
<sup>c</sup> Ratio calculated without using data from the outer ring of fibers				

Table 4.1: Carbonate/Phosphate ratios measured transcutaneously and on exposed bone

	<b>Ring</b>	<b>OD</b>	<b>ID</b>	<b>Offset</b>
<b>Polymer</b>	1	10.0	8.0	2.5
<b>Chicken</b>	1	5.0	4.0	0.5
	2	7.0	5.0	1.0
	3	11.0	8.0	2.5
	4	12.0	10.0	3.5
	5	15.0	12.0	4.5

Table 4.2: Illumination ring geometry and disk offsets

## References

1. V. Tuchin, *Tissue Optics Light Scattering Methods and Instruments for Medical Diagnosis*, SPIE Press, Bellingham, (2000).
2. T. Vo-Dinh, *Biomedical Photonics Handbook*, CRC Press, Boca Raton (2003).
3. N. Everall, T. Hahn, P. Matousek and A. W. Parker, "Photon migration in Raman spectroscopy," *Appl. Spectrosc.* 58, 591-597 (2004)
4. N. Everall, T. Hahn, P. Matousek, A. W. Parker and M. Towrie, "Picosecond time-resolved Raman spectroscopy of solids: Capabilities and limitations for fluorescence rejection and the influence of diffuse reflectance," *Appl. Spectrosc.* 55(12), 1701-1708 (2001)
5. P. Matousek, N. Everall, M. Towrie and A. W. Parker, "Depth profiling in diffusely scattering media using Raman spectroscopy and picosecond Kerr gating," *Appl. Spectrosc.* 59(2), 200-205 (2005)
6. T. J. Pfefer, K. T. Schomacker, M. N. Ediger and N. S. Nishioka, "Multiple-fiber probe design for fluorescence spectroscopy in tissue," *Appl. Opt.* 41(22), 4712-4721 (2002)
7. U. Utzinger and R. R. Richards-Kortum, "Fiber optic probes for biomedical optical spectroscopy," *J. Biomed. Opt.* 8(1), 121-147 (2003)
8. E. L. Hull, M. G. Nichols and T. H. Foster, "Localization of luminescent inhomogeneities in turbid media with spatially resolved measurements of cw diffuse luminescence emittance," *Appl. Opt.* 37, 2755-2765 (1998)
9. P. Matousek, M. D. Morris, N. Everall, I. P. Clark, M. Towrie, E. Draper, A. Goodship and A. W. Parker, "Numerical Simulations of Subsurface Probing in Diffusely Scattering Media Using Spatially Offset Raman Spectroscopy " *Appl. Spectrosc.* 59(12), 1485-1492 (2005)
10. P. Matousek, I. P. Clark, E. R. C. Draper, M. D. Morris, A. E. Goodship, N. Everall, M. Towrie, W. F. Finney and A. W. Parker, "Subsurface Probing in Diffusely



Scattering Media Using Spatially Offset Raman Spectroscopy," *Appl. Spectrosc.* 59(4), 393-400 (2005)

11. M. V. Schulmerich, W. F. Finney, R. A. Fredricks and M. D. Morris, "Subsurface Raman Spectroscopy and Mapping Using a Globally Illuminated Non-Confocal Fiber-Optic Array Probe in the Presence of Raman Photon Migration," *Appl. Spectrosc.* 60(2), 109-114 (2006)

12. M. V. Schulmerich, W. F. Finney, V. Popescu, M. D. Morris, T. M. Vanasse and S. A. Goldstein, "Transcutaneous Raman spectroscopy of bone tissue using a non-confocal fiber optic array probe," *Proc. SPIE* 6093, O1-O7 (2006)

13. M. V. Schulmerich, K. A. Dooley, M. D. Morris, T. M. Vanasse and S. A. Goldstein, "Transcutaneous fiber optic Raman spectroscopy of bone using annular illumination and a circular array of collection fibers," *J. Biomed. Opt.* 11(6), 060502 (2006)

14. P. Matousek, "Inverse Spatially Offset Raman Spectroscopy for Deep Noninvasive Probing of Turbid Media " *Appl. Spectrosc.* 60(11), 1341-1347 (2006)

15. D. Zhang, J. D. Hanna, Y. Jiang and D. Ben-Amotz, "Influence of Laser Illumination Geometry on the Power Distribution Advantage," *Appl. Spectrosc.* 55(1), 61-65 (2001)

16. P.-A. Bélanger and M. Rioux, "Ring pattern of a lens-axicon doublet illuminated by a Gaussian beam," *Appl. Opt.* 17(7), 1080-1086 (1978)

17. F. J. Harris, "On the Use of Windows for Harmonic Analysis with the Discrete Fourier Transform," *Proc. IEEE* 66(1), 51-83 (1978)

18. C. A. Lieber and A. Mahadevan-Jansen, "Automated Method for Subtraction of Fluorescence from Biological Raman Spectra," *Appl. Spectrosc.* 57(11), 1363-1367 (2003)

19. L. Guo, F. Kooli and M. Garland, "A general method for the recovery of pure powder XRD patterns from complex mixtures using no a priori information Application of band-target entropy minimization (BTEM) to materials characterization of inorganic mixtures," *Anal. Chim. Acta* 517, 229-236 (2004)

20. L. R. Ong, E. Widjaja, R. Stanforth and M. Garland, "Fourier transform Raman spectral reconstruction of inorganic lead mixtures using a novel band-target entropy minimization (BTEM) method," *J. Raman Spectrosc.* 34, 282-289 (2003)
21. E. Widjaja, C. Li and M. Garland, "Semi-Batch Homogeneous Catalytic In-Situ Spectroscopic Data. FTIR Spectral Reconstructions Using Band-Target Entropy Minimization (BTEM) without Spectral Preconditioning," *Organometallics* 21, 1991-1997 (2002)
22. W. Chew, E. Widjaja and M. Garland, "Band-Target Entropy Minimization (BTEM): An Advanced Method for Recovering Unknown Pure Component Spectra. Application to the FTIR Spectra of Unstable Organometallic Mixtures," *Organometallics* 21, 1982-1990 (2002)
23. E. Widjaja, N. Crane, T.-C. Chen, M. D. Morris, M. A. Ignelzi and B. R. McCreadie, "Band-Target Entropy Minimization (BTEM) Applied to Hyperspectral Raman Image Data," *Appl. Spectrosc.* 57(11), 1353-1362 (2003)

**CHAPTER V**  
**SUBSURFACE AND TRANSCUTANEOUS RAMAN**  
**SPECTROSCOPY AND MAPPING USING CONCENTRIC**  
**ILLUMINATION RINGS AND COLLECTION WITH A CIRCULAR**  
**FIBER OPTIC ARRAY**

**Introduction**

As earlier chapters demonstrate fiber optic probes in which the signal is detected at a distance from the point or points where light is injected into the system can be used for depth-resolved subsurface optical spectroscopy in highly scattering (turbid) systems, such as tablets, polymers, and human or animal tissue. As the distance between the illumination and collection region is increased, the recovered Raman spectra contain increasingly greater contributions from subsurface components. This approach provides a degree of depth resolution to the technique.

Shim et al.<sup>1</sup> demonstrated depth resolved Raman spectroscopy in an Intralipid suspension phantom using a 7-around-1 fiber optic probe with interchangeable beveled tips. As tips with increasing bevel angles were used, the distance between excitation and collection region decreased and the collection region moved closer to the surface. The same probe was used by Bakker Schut and co-workers to detect dysplastic tissue in a rat model of oral cancer.<sup>2</sup> The beveled collection fibers sampled well below the surface of

the specimen to include bone tissue. To resolve the dysplastic tissue spectrum from the underlying bone spectrum, principal components analysis was used. Later, Motz et al. showed that with a tightly focused probe, a spacer between the laser delivery fiber and fifteen collection fibers was needed to obtain the maximum Raman signal from the surface of a highly scattering sample.<sup>3</sup> Their probe was intended for insertion into a catheter and only small offset effects were studied.

For these early studies, the probes used had limited source/detection spacing and therefore the signals were recovered from depths of less than 1mm. The potential for greater depth penetration and depth resolution by spatial offsetting was first demonstrated and systematically investigated by Matousek et al.<sup>4</sup> These workers were also the first to use Monte Carlo methods to model spatially offset Raman spectroscopy (SORS).<sup>5</sup> Since the first demonstration of millimeter depth resolution with a two-fiber probe, several new designs have been implemented. Pharmaceutical<sup>6</sup> and biomedical<sup>7-9</sup> problems have emerged as the first major application areas.

The first depth resolving fiber Raman probes employed point illumination. However, this approach limits the amount of laser power that can be delivered without thermal damage. The problem is serious in biomedical applications and there are accepted standards for maximum laser power exposure to human skin such as ANSI Z136.1-2007.<sup>10</sup>

We have demonstrated that laser power distributed over the field of view of collection fibers can eliminate thermal damage and can also allow subsurface mapping.<sup>11</sup> This global illumination method was demonstrated in Raman microscopic mapping a decade ago<sup>12</sup>, although its subsurface measurement properties were not discussed. Using

a commercially available fiber optic probe, we have demonstrated mapping of polymer samples placed beneath several millimeters of Teflon.<sup>11</sup> We have also shown that the global illumination probe can recover bone Raman spectra through the skin of human cadaveric limbs and chicken legs at depths of several millimeters.<sup>7</sup>

If the target tissue (or other object) is close to the surface, point illumination is certainly feasible. Bone spectra have been observed through the skin of a volunteer using point illumination with low power (1.8 mW) and an array of collection fibers.<sup>9</sup>

Though subsurface information is available, the global illumination probe, in common with other backscatter-collection methods, heavily weights spectral components from at or near the surface of the material.<sup>6</sup> For transcutaneous Raman spectroscopy in human or animal subjects, this surface weighting results in a large fluorescence background from skin melanin. One simple and powerful solution to the surface weighting problem is to illuminate one surface and collect the light transmitted through the sample.<sup>13</sup> Matousek has recently demonstrated that collecting transmitted light in a strongly scattering system provides surface fluorescence rejection as well as composition averaging.<sup>6</sup>

Another solution to the surface weighting problem is a fiber probe design that has been independently developed by our group,<sup>8, 14</sup> denoted as annular illumination or ring/disk, and by Matousek<sup>15</sup>, described as inverse SORS. In this design, an axicon is used to convert the laser beam into an annulus, which surrounds the field of view of a disk-shaped array of collection fibers. The separation between the illumination ring and the collection disk determines the depth from which much of the signal is recovered. In biomedical applications, an advantage of this design is that much of the skin fluorescence

is spatially rejected. The ring diameter is easily varied with telephoto optics<sup>8, 14</sup> or by changing the distance between the axicon and the specimen<sup>15</sup>.

It is expected that the ring/disk probe can provide subsurface maps as well as depth-resolved spectra and rejection of surface signals. The ring/disk configuration may be especially useful for measurements in tissue or in other materials where thermal damage is likely. It is well-known that heat is conducted away from a line-focused laser beam more efficiently than from an area-focused beam.<sup>16</sup> Except at very small diameters, the ring is thermally equivalent to a line, suggesting that the ring/disk probe may have better thermal properties than the global illumination probe.

An additional advantage of the ring/disk configuration is the potential of using multiple ring/disk separations to acquire both Raman spectra of a target at multiple depths and an approximate three-dimensional reconstruction. Changing ring diameter changes the angle at which light is incident on the surface of a specimen. Changes in ring diameter are equivalent to the generation of new projections for use in tomographic reconstruction.

Tomographic reconstruction methods have been described in the fluorescence literature and is currently an active area of research.<sup>17-26</sup> Reconstruction from fluorescence data is an ill-posed inverse problem. Accuracy of reconstruction can be improved and computations can be simplified by utilizing prior knowledge of the shape of the buried target. Target shape can often be obtained by proven methods based on, for example, ultrasound, magnetic resonance imaging, or X-ray tomography.

Optical spectroscopy may be an important complement to such technologies as MRI, computed tomography, and ultrasound, which provide detailed morphological

information and some mechanical property estimates, but limited or no chemical composition information. Near-infrared and fluorescence spectroscopies partially overcome this limitation, and it is expected that Raman spectroscopy can be developed into a powerful alternative and/or adjunct for many important biomedical applications.

In this paper we examine the effects of ring/disk separation on both the depth recovery of spectra of buried components and on subsurface mapping. To facilitate comparison with our global illumination probe, we test the subsurface mapping properties of the ring/disk probe using blocks of polyethylene, Teflon, and Delrin in simple geometries. We also present results of transcutaneous spectroscopy in canine tibiae, used as a model system for human subject bone tissue spectroscopy and mapping.

## **Experimental**

A schematic of the Raman spectroscopic system is shown in figure 5.1. A 400 mW 785 nm external cavity diode laser (Invictus, Kaiser Optical Systems, Inc., Ann Arbor, MI) is used for excitation. The laser beam is passed through a 200  $\mu\text{m}$  core NIR optical fiber (Multimode Fiber Optics, Hackettstown, NJ). The light was collimated (F810FC-780, Thorlabs Inc., Newton, NJ) and directed through a 175° axicon (Del Mar Photonics, San Diego, CA). A Galilean telescope (positive/negative lens pair) was used to focus the ring to inner diameters between 3.0 mm and 14.5 mm. The collection channel of a non-confocal fiber optic probe (PhAT probe, Kaiser Optical Systems, Inc.) was employed to collect backscattered Raman shifted light and present it to the spectrograph. The probe contained a 1 mm in diameter circular bundle of fifty 100  $\mu\text{m}$

core/125  $\mu\text{m}$  core plus cladding collection fibers. A 75 mm focal length lens was used at the probe head, resulting in a 3 mm diameter circular field of view from the fiber bundle. A dichroic mirror (Chroma Technology Corp., Rockingham, VT) reflected the 785 nm light to the sample and transmitted the Raman signal to the collection fibers. Components were mounted in lens tubes and a mirror mount (SM1 series, Thorlabs Inc., Newton, NJ). A NIR-optimized imaging spectrograph (Holospec, f/1.8, Kaiser Optical Systems) fitted with a 50  $\mu\text{m}$  slit was used to provide 6-8  $\text{cm}^{-1}$  spectral resolution. The detector was a thermoelectrically cooled deep-depletion 1024x256 pixel CCD (Model DU420-BR-DD, Andor Technology, Belfast, Northern Ireland) operated at -75  $^{\circ}\text{C}$ . No binning was used.

The wavelength axis of the spectrograph was calibrated against the neon discharge lamp of a HoloLab Calibration Accessory (Kaiser Optical Systems, Inc.). The diffused white light from the Calibration Accessory was used to correct for the wavelength response of the CCD. The acquisition time for measurement at each ring diameter was 60 seconds. The incident power varied between 200 and 210 mW depending on the details of optical alignment.

Blocks of polymers were used for depth penetration and subsurface mapping experiments. Polyethylene, Delrin, and Teflon were machined into 51 mm x 51 mm blocks and stacked to achieve different thicknesses and different geometries (Figure 5.2). A 225 g brass block with a circular hole was placed over the assembly of polymer blocks to minimize voids between them. The configuration in figure 5.2a was used to examine mapping capabilities of the probe. The collection disk was oriented over the center of the interface between the polyethylene and Delrin blocks. The illumination ring was



incident on the Teflon surface and the collection optics were focused onto the surface of the Teflon block over the subsurface interface. The thickness of the Teflon layer was varied between 0 mm and 10.4 mm in increments of 0.8 mm. To generate maps of the subsurface interface, the known correspondence between the positions of fibers at the linear array (spectrograph) end of the fiber bundle and the circular (collection) end was used.<sup>11</sup> The configuration in figure 5.2b was used to measure the polymer thickness through which the spectrum of a buried block of Delrin 4 mm thick could be recovered. Teflon layer thicknesses between 13.0 mm and 22.6 mm were used. Table 5.1 shows the inner and outer diameters of the rings of laser light used in these measurements, and a schematic of the ring illumination/disk collection scheme is shown in figure 5.3.

The tissue specimens used were intact canine lower extremities obtained from a discarded tissue repository. The limbs were harvested from an animal euthanized in approved (University Committee on Use and Care of Animals) studies at the University of Michigan Medical School. The preparation of the specimen included preservation of all the soft tissues and skin distal to the mid-femur. Hair was removed with a depilatory agent (Sally Hansen Corp, Uniondale, NY) and glycerol was then applied for optical clearing. The collection disk was positioned at the medial side of the left and right tibia at the diaphysis. The dimensions of the rings used for transcutaneous measurements are shown in table 5.1.

After all transcutaneous measurements were completed, the overlying tissue was removed. Spectra of the exposed bone were obtained with global illumination and with the ring/disk configuration using ring 5 (table 5.1). The two data sets were combined to provide 100 reference bone spectra.

## Data Treatment

All data reduction was performed in MATLAB 6.1 (The Mathworks Inc., Natick, MA) using vendor-supplied and locally written scripts. The data for each acquisition consisted of an array of 256 Raman spectra as a single CCD image. Initial preprocessing included dark current subtraction, correction for pixel-pixel response variations, and correction for wavelength response variations. The images were then corrected for slit image curvature caused by the large gathering angle of the spectrograph. A Blackman-Harris windowing function was applied to each spectrum to remove high frequency components.<sup>27</sup> The spectra from each fiber covered five rows of the spectrograph, but only the central three spectra from each fiber were used to avoid cross-talk from adjacent fibers. For each acquisition the central three spectra were averaged prior to further data reduction, yielding a data set of fifty spectra, each spectrum corresponding to one fiber. A wavenumber region of interest was then selected.

To investigate depth of signal recovery for the polymer data, band target entropy minimization (BTEM)<sup>28-32</sup> was used to recover the Delrin factor. The spectral range chosen for targeting was  $910\text{ cm}^{-1}$  to  $925\text{ cm}^{-1}$  (Delrin max at  $918\text{ cm}^{-1}$ ); the number of eigenvectors was increased from 15 to 195 as the amount of overlying Teflon increased.

Use of a large number of eigenvectors is necessary to extract minor spectral components by BTEM. Inclusion of eigenvectors containing predominantly distributed random noise is used to improve the signal to noise ratio of the recovered spectra. The stopping point is reached when additional eigenvectors add only noise. At least twice as many eigenvectors are included in the calculation as the number of components sought.

Usually many more are included. We use the eigenvector weight distribution test for selecting the appropriate number of eigenvectors, as described elsewhere.<sup>31</sup>

To investigate the preservation of spatial information, a covariance matrix was calculated and a score plot was generated using reference measurements on each of the polymers. The factors were normalized so that the sum of the scores for a given fiber equaled the total intensity of signal from that fiber. The relative intensities were then mapped onto a schematic of the collection array. This was done for each ring. Measurements for all four rings were normalized and then combined into a single matrix resulting in a dataset equivalent to taking a 4 minute acquisition with each ring illuminating for 1 minute. Each ring was concentric to the collection region.

For the canine limb data, an iterative baselining procedure with a fifth-order polynomial was used to remove background fluorescence.<sup>33</sup> For the transcutaneous measurements, BTEM was used to recover a bone factor for each ring. The region of interest targeted was  $956\text{ cm}^{-1}$  to  $962\text{ cm}^{-1}$  which contains the phosphate  $\nu_1$  band in bone. The number of eigenvectors ranged from 5 to 25. The recovered bone factor and all the exposed bone measurements were imported into GRAMS/AI/Razor Tools (Thermo Galactic, Madison, Wisconsin) and fit for peak areas and heights using mixed Gaussian and Lorentzian polynomials and standard peak width constraints.

## **Results and Discussion**

Reference spectra for polyethylene, Delrin, and Teflon were obtained using global illumination and are shown normalized and offset in figure 5.4. The top spectrum of

polyethylene is the averaged spectra obtained from fifty collection fibers. The strongest band is at  $808\text{ cm}^{-1}$ . The middle (averaged) spectrum is of Delrin. The strongest Raman band is at  $918\text{ cm}^{-1}$ . The bottom (averaged) spectrum is of Teflon. The strongest band is at  $732\text{ cm}^{-1}$ .

Figure 5.5 shows results from the three component polymer system (figure 5.2a). The spectra in figure 5.5a are the averaged spectra obtained from the fifty collection fibers for each ring/disk spacing with 5.6 mm of overlying Teflon. The spectra are offset for clarity. The spectral region from  $800\text{ cm}^{-1}$  to  $1150\text{ cm}^{-1}$  contains the most intense bands for the polyethylene and Delrin subsurface components. This region is enlarged to illustrate the increasing contribution of the subsurface components to recovered signal intensity as the ring/disk spacing is increased. Figure 5.5b shows the average spectrum from all four ring/disk separations (i.e. from 200 fibers) as the depth of overlying Teflon increases. The most intense bands of both Delrin and polyethylene are visible through 10.4 mm of overlying Teflon.

Figure 5.6 shows Raman maps of the three component system used to investigate the depths at which spatial recovery is achievable with different illumination/collection separations. A Raman map of the polyethylene-Delrin interface (no overlying Teflon) is shown at the top left-hand side of the figure. The first and second column illustrates a 0 mm and 0.5 mm illumination/collection spacing. The spatial information is preserved from 0.8 mm until a depth of  $\sim 4$  mm of overlying Teflon. Raman maps of the 2.5 mm collection/illumination spacing are shown in the third column. The interface is blurred at a 0.8 mm depth, regains focus at a 1.6 mm depth, and then loses focus at a depth between 4.8 mm and 5.6 mm of overlying Teflon. Similar results are seen in the fourth column

for the 4.5 mm illumination/collection spacing. As the illumination/collection spacing increases, spatial information from deeper depths is preserved while the spatial information at shallower depths is blurred. This suggests that an optimal illumination/collection offset exists for different depths. The fifth column shows Raman fiber maps that result when the datasets from all four illumination/collection separations are linearly added (200 collection fibers). The polyethylene-Delrin subsurface interface is in focus from 0.8 mm of overlying Teflon and remains in focus until between 5.6 mm to 6.4 mm of overlying Teflon. The multiple depths of focus are a result of multiple illumination/collection spacings. Equal weighting of each ring in the combined data set provides only a first approximation towards the reconstruction of the subsurface composition and morphology. This approximation yields adequate results for simple polymer block geometries. In less contrived systems, more complex restoration algorithms and optimized spacing protocols will be necessary to achieve subsurface Raman mapping.

Figure 5.7 shows results for the two layer polymer system (figure 5.2b). In figure 5.7a, the data from all four illumination/collection spacings are combined and averaged at each of the Teflon depths sampled. Reference spectra for Teflon (top) and Delrin (bottom) are included. The region from  $800\text{ cm}^{-1}$  to  $1150\text{ cm}^{-1}$  is magnified to emphasize the Delrin contribution to the average signal. The Delrin band at  $918\text{ cm}^{-1}$  is visible with 22.6 mm of overlying Teflon. The recovered (BTEM) Delrin factor is shown in figure 5.7b. The Delrin factor is recoverable with high signal/noise ratio through 17.8 mm of overlying Teflon, while more noisy Delrin factors, which can be used for mapping, are recoverable at 22.6 mm of overlying Teflon.

Figure 5.8 shows the results of spectra taken of an excised canine tibia. The target was bone which was found to be 2 mm below the skin's surface. In figure 8a, the transcutaneous measurement (gray) is the average spectra obtained from all 10 rings (500 fibers). The transcutaneous measurements contain bands from components of the skin and underlying tissue including collagen, lipids, melanin, and blood. For comparison, the exposed bone measurements (n=100) are shown in black. Figure 5.8b shows the BTEM recovered bone factors for each illumination/collection spacing. The exposed bone measurements are shown for reference.

Figure 5.8c shows the carbonate/phosphate ( $1070\text{ cm}^{-1}/958\text{ cm}^{-1}$ ) band area ratios and figure 5.8d shows the carbonate/phosphate band height ratios as a function of ring center diameter. Carbonate/phosphate is a potential biomarker for fragility fracture susceptibility in osteoporotic bone tissue.<sup>34</sup> Both figures 5.8c and 5.8d show the ratio for the exposed bone spectra (n=100; error bars represent one standard deviation from the mean), the recovered bone factor for each ring illumination, and the recovered bone factor for the combined data set, with each ring/disk spacing given an equal weighting. From this data it is seen that for a 3 mm diameter collection disk, a center ring diameter of 8.0 mm provides an approximation to the optimal ring/disk separation. At this ring/disk spacing there is a +1.5% error in the ratio calculated from band areas and a -0.7% error in the ratio calculated from band heights. Using all the ring/disk spacings result in larger errors. The carbonate/phosphate ratio calculated as band areas has a +22% error and by heights a 36% error. These poor results occur because the small ring spacings overemphasize scatter from close to the skin surface, while those at the largest spacings include data with very low signal/noise ratio.

To define criteria for choosing ring/disk separations, we plotted phosphate  $\nu_1$ /phenylalanine ring breathing band height and area ratios as functions of ring diameter. This ratio measures the relative amounts of bone mineral and total collagen (skin, tendon and bone) in the recovered spectra. The results are shown in figure 5.9. As expected, these ratios increase with increasing ring/disk spacing. The increase is slow at small spacings and rapid when the spacing is increased sufficiently to attenuate much of the signal from skin and tendon collagen. The starting point of this rise is the spacing at which the best accuracy is obtained. Although the bone contributions to the measured spectra are even greater with larger spacings, the signal/noise ratio decreases rapidly, leading to increased error.

A simple and effective protocol for bone signal recovery is to vary the ring spacing around the approximate value of the optimum. Either the inflection point, or the results of BTEM or another multivariate self-modeling curve resolution method can be used to extract the bone spectrum and calculate the desired band area and height ratios. Of course, efficient use of this procedure requires prior knowledge of the depth below the skin at which the bone is found. Approximate values are known for both men and women and methods such as ultrasound can provide accurate results for individuals.

To test this protocol, we applied it to measurement of a second canine tibia, using a point near the distal end of the tibia at which the bone was below 5 mm of skin and tendon. This measurement site was chosen because it is similar to the distance expected to the distal radius of female human subjects. Figure 5.10 shows the results of spectra taken of a second excised canine tibia. In figure 5.10a we show the mean transcutaneous spectrum calculated over the data set used to recover the bone spectrum by BTEM, the

recovered spectrum and the spectrum of the exposed bone. Figure 5.10b shows the phosphate  $\nu_1$ /phenylalanine ring breathing band height ratios as functions of ring diameter. For clarity error bars are omitted. In figure 5.10c the calculated carbonate/phosphate ratios by band height and area are compared to the measurements made on exposed bone tissue. From this figure it is seen that the height measurements are in good agreement (-4.5% error) with the results for exposed tissue, but the agreement is poor (-63%) for measurements by area. We attribute this difference to the difficulty of defining area, especially the area of the less intense carbonate band, in these noisy measurements.

## Conclusions

The results obtained with two and three component polymer systems demonstrates that the ring/disk fiber optic probe has good depth recovery properties and preserves subsurface component distribution, although it is blurred by photon diffusion. Importantly, the ring/disk fiber optic probe samples deep enough to recover bone spectra at least 5 mm below skin and tendons of canines. The data suggests that bone Raman measurements in human subjects are feasible at the distal radius and other sites that are important for prediction of osteoporotic fragility fracture susceptibility. Improving the collection efficiency of the optics will be needed to reduce the collection time to more realistic values. Our probe uses an f/3 collection lens. Decreasing the f/number should allow collection in shorter times.



In this work tomographic reconstruction has been limited to finding a buried interface centered in the field of view of the probe. This case is the simplest possible case of reconstruction using *a priori* spatial information and measured spectral information. It is known that the combination of independently measured spatial and optical spectral information provides the most accurate tomographic reconstruction using currently available fitting algorithms. The use of information-rich Raman spectral bands in tomographic reconstruction is potentially a powerful new methodology for medical diagnostics and a host of other applications.

## Figures

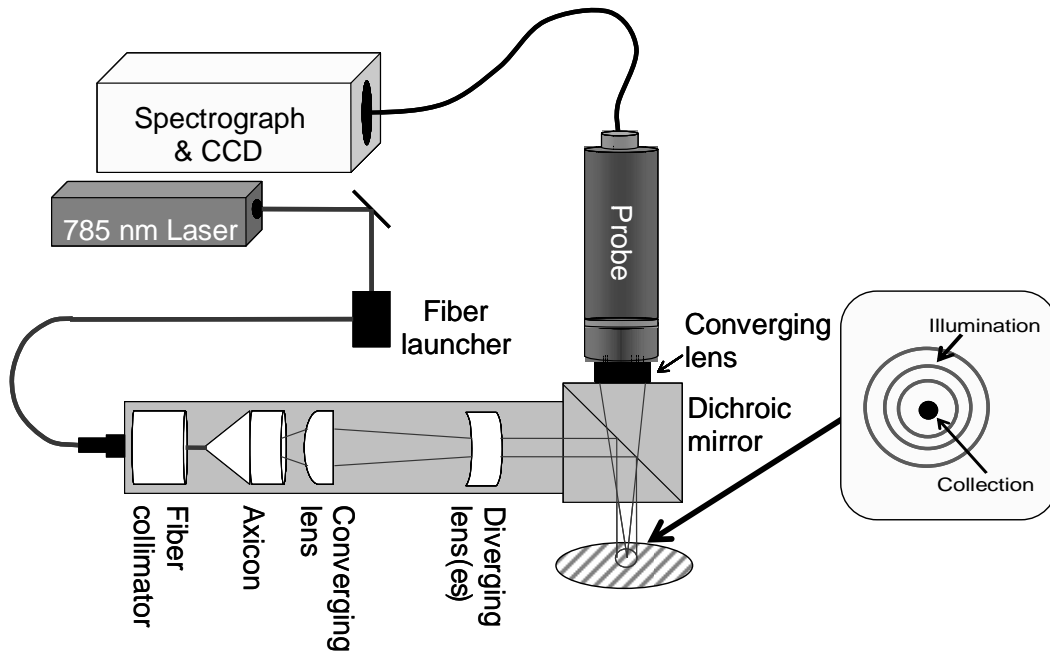


Figure 5.1: Schematic of the experimental apparatus. Probe generates a single ring that can be varied in diameter, light is collected from the center of the ring.

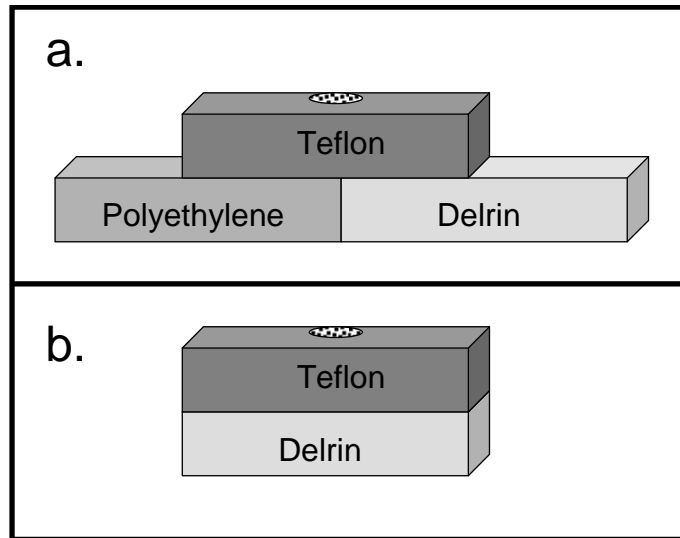


Figure 5.2: Configuration of polymer test systems. Light is incident on the surface of the top layer (shaded circle). (*a*) subsurface interface between polyethylene (4mm thick) and Delrin (4mm thick) under Teflon (*b*) Delrin target under Teflon. Teflon layer was systematically varied.

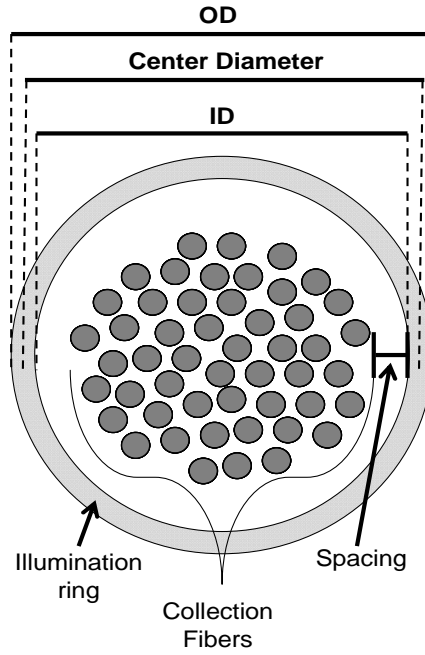


Figure 5.3: Schematic of ring illumination/disk collection. Center diameter is defined as the diameter of the illumination ring measured from the center of the laser beam.

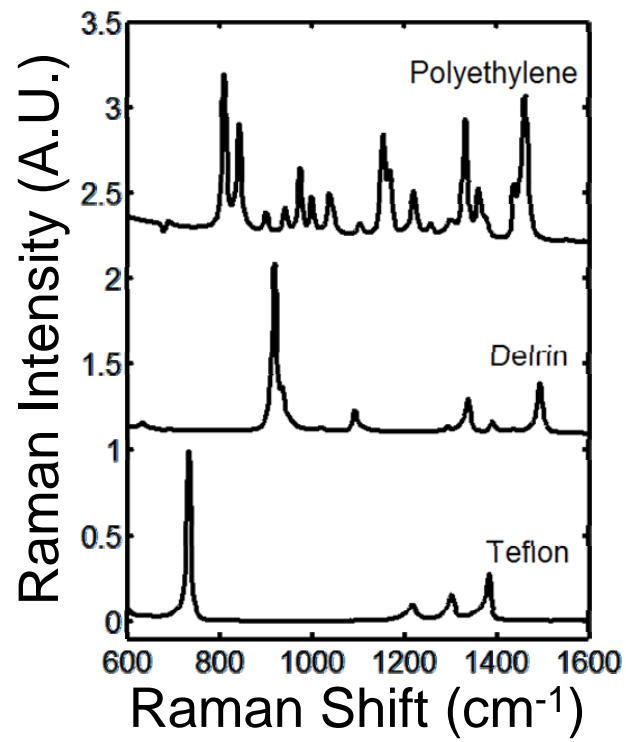


Figure 5.4: Raman spectra of (*top*) polyethylene, (*middle*) Delrin, and (*bottom*) Teflon

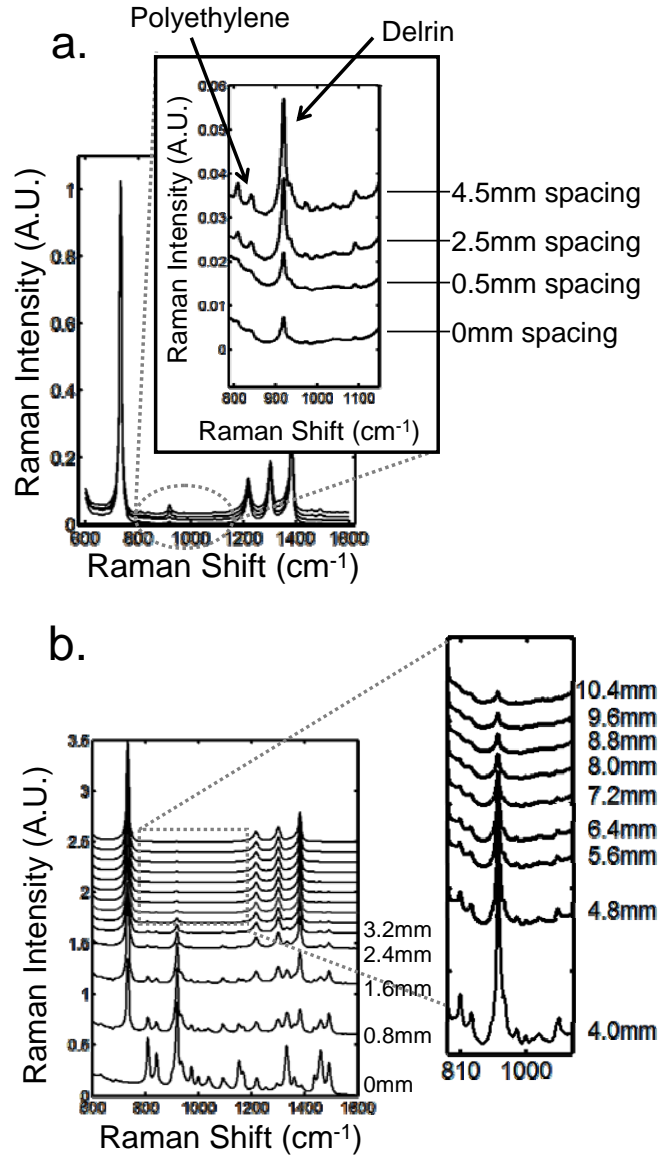


Figure 5.5: Raman spectra of subsurface interface (a) polyethylene and Delrin contributions to the mixed component spectra at four different ring/disk spacings, with 5.6mm of overlying Teflon (b) averaged ( $n=200$ ) spectra of all four ring/disk spacings combined (rings equally weighted) into a single data set with varying amounts of overlying Teflon.

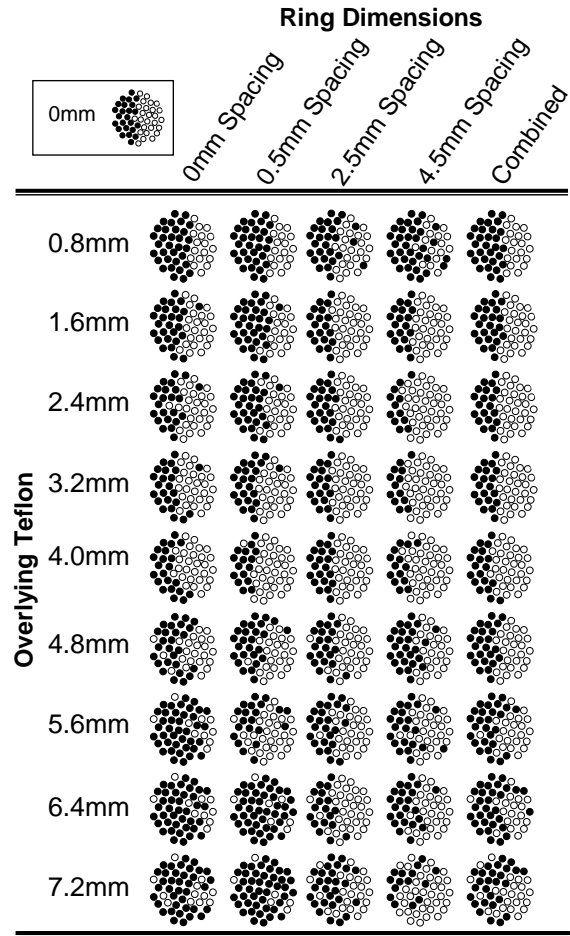


Figure 5.6: Fiber maps of subsurface interface at different ring/disk spacings

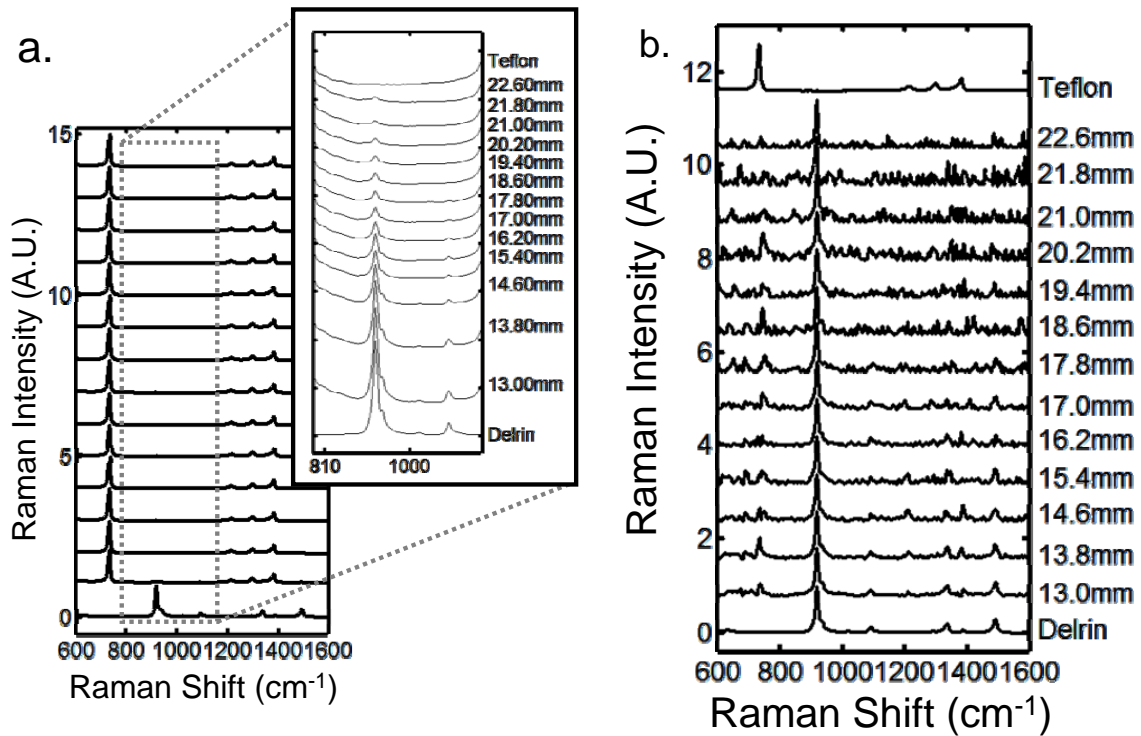


Figure 5.7: Varying amounts of Teflon over Delrin (*a*) averaged ( $n=200$ ) mixed component spectra. The insert shows the 800 to 1200  $\text{cm}^{-1}$  region magnified to emphasize the subsurface contribution (*b*) BTEM recovered Delrin factors



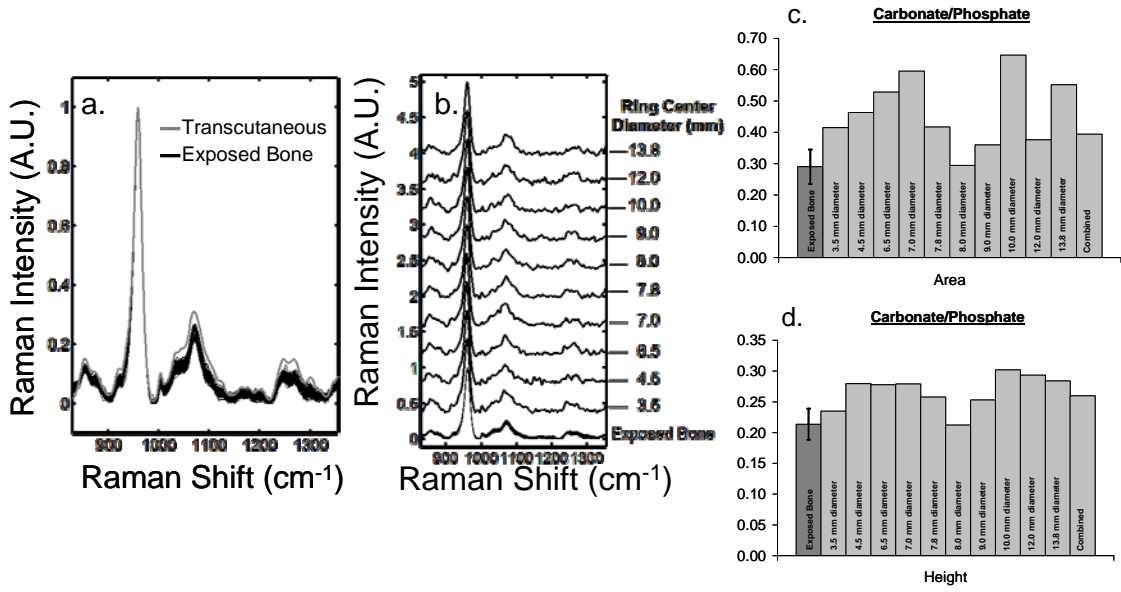


Figure 5.8: Transcutaneous Raman spectra of dog tibia positioned at the medial side of the left tibia at the dyaphysis, 2mm of overlying tissue (**a**) averaged (n=500) transcutaneous, spectrum (gray) and exposed bone spectra (n=100) (black) (**b**) recovered bone spectrum for each ring/disk spacing (**c**) carbonate/phosphate band area ratio; comparison of the recovered bone spectra for each ring to the exposed bone measurement (**d**) carbonate/phosphate band height ratio; comparison of the recovered bone spectra for each ring to the exposed bone measurement

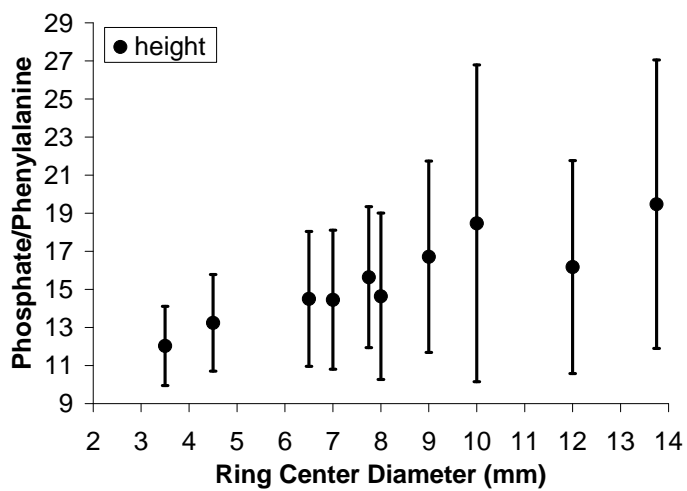
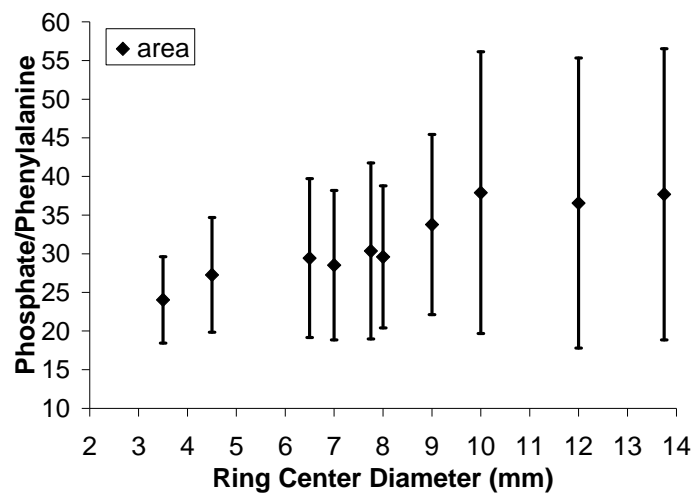


Figure 5.9: Phosphate  $\nu_1$ /phenylalanine ring breathing band height and area ratios as functions of ring diameter

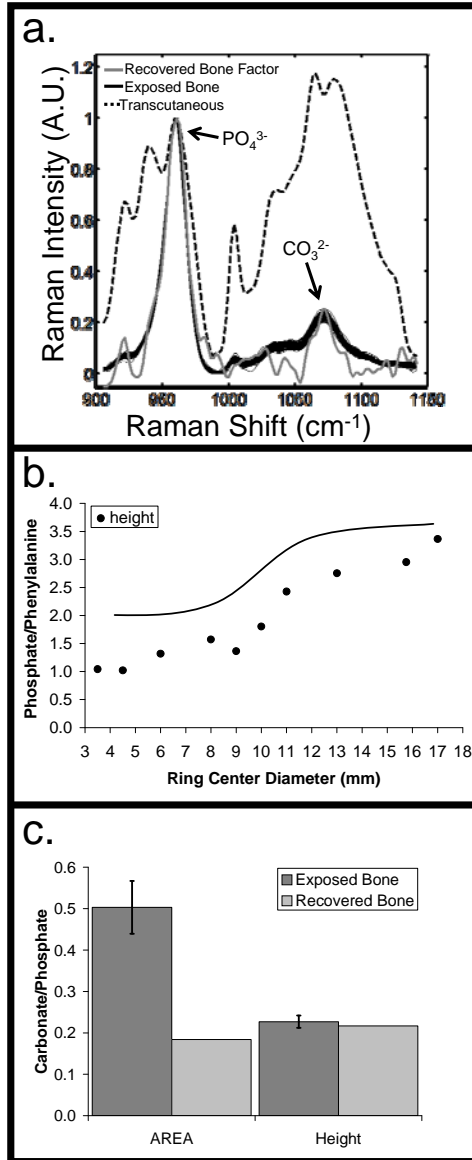


Figure 5.10: Transcutaneous Raman spectra of dog tibia at the medial side of the right tibia at the dyaphysis, 5mm of overlying tissue (**a**) averaged ( $n=250$ ) transcutaneous spectrum (dashed), exposed bone spectra ( $n=100$ ) (black), and recovered bone spectra (gray) (**b**) Phosphate  $\nu_1$ /phenylalanine ring breathing band height ratio as functions of ring diameter (circles), approximation of expected function (line) (**c**) carbonate/phosphate band area and height ratios for the recovered and exposed bone spectra.

	ring #	OD (mm)	ID (mm)	Center Diameter (mm)	Spacing (mm)
<b>Polymers</b>	1	4.0	3.0	3.5	0
	2	5.0	3.5	4.3	0.25
	3	10.0	8.0	9.0	2.5
	4	14.0	12.0	13.0	4.5
<b>Dog Tibia</b> <i>(2mm depth)</i>	1	4.0	3.0	3.5	0
	2	5.0	4.0	4.5	0.5
	3	7.0	6.0	6.5	1.5
	4	8.0	6.0	7.0	1.5
	5	9.0	6.5	7.8	1.75
	6	9.0	7.0	8.0	2
	7	10.0	8.0	9.0	2.5
	8	11.0	9.0	10.0	3
	9	13.0	11.0	12.0	4
	10	15.0	12.5	13.8	4.75
<b>Dog Tibia</b> <i>(5mm depth)</i>	1	4.0	3.0	3.5	0
	2	5.0	4.0	4.5	0.5
	3	7.0	5.0	6.0	1
	4	9.0	7.0	8.0	2
	5	10.0	8.0	9.0	2.5
	6	11.0	9.0	10.0	3
	7	12.0	10.0	11.0	3.5
	8	14.0	12.0	13.0	4.5
	9	17.0	14.5	15.8	5.75
	10	20.0	14.0	17.0	5.5

Table 5.1: Ring/disk spacings

## References

1. M. G. Shim, B. C. Wilson, E. Marple and M. Wach, "Study of Fiber-Optic Probes for in Vivo Medical Raman Spectroscopy," *Appl. Spectrosc.* 53(6), 619-627 (1999)
2. T. C. Bakker Schut, M. J. H. Witjes, H. J. C. M. Sterenberg, O. C. Speelman, J. L. N. Roodenburg, E. T. Marple, H. A. Bruining and G. J. Puppels, "In Vivo Detection of Dysplastic Tissue by Raman Spectroscopy," *Anal. Chem.* 72, 610-618 (2000)
3. J. T. Motz, M. Hunter, L. H. Galindo, J. A. Gardecki, J. R. Kramer, R. R. Dasari and M. S. Feld, "Optical fiber probe for biomedical Raman spectroscopy," *Appl. Opt.* 43(3), 542-554 (2004)
4. P. Matousek, I. P. Clark, E. R. C. Draper, M. D. Morris, A. E. Goodship, N. Everall, M. Towrie, W. F. Finney and A. W. Parker, "Subsurface Probing in Diffusely Scattering Media Using Spatially Offset Raman Spectroscopy," *Appl. Spectrosc.* 59(4), 393-400 (2005)
5. P. Matousek, M. D. Morris, N. Everall, I. P. Clark, M. Towrie, E. Draper, A. Goodship and A. W. Parker, "Numerical Simulations of Subsurface Probing in Diffusely Scattering Media Using Spatially Offset Raman Spectroscopy " *Appl. Spectrosc.* 59(12), 1485-1492 (2005)
6. P. Matousek and A. W. Parker, "Bulk Raman Analysis of Pharmaceutical Tablets," *Appl. Spectrosc.* 60(12), 1353-1357 (2006)
7. M. V. Schulmerich, W. F. Finney, V. Popescu, M. D. Morris, T. M. Vanasse and S. A. Goldstein, "Transcutaneous Raman spectroscopy of bone tissue using a non-confocal fiber optic array probe," *Proc. SPIE* 6093, O1-O7 (2006)
8. M. V. Schulmerich, K. A. Dooley, M. D. Morris, T. M. Vanasse and S. A. Goldstein, "Transcutaneous fiber optic Raman spectroscopy of bone using annular illumination and a circular array of collection fibers," *J. Biomed. Opt.* 11(6), 060502 (2006)
9. P. Matousek, E. R. C. Draper, A. E. Goodship, I. P. Clark, K. L. Ronayne and A. W. Parker, "Noninvasive Raman Spectroscopy of Human Tissue *In Vivo*," *Appl. Spectrosc.* 60(7), 758-763 (2006)

10. " Z136.1 " in Safe use of Lasers American Nation Standards Institute, Ed., Orlando Florida (2007).
11. M. V. Schulmerich, W. F. Finney, R. A. Fredricks and M. D. Morris, "Subsurface Raman Spectroscopy and Mapping Using a Globally Illuminated Non-Confocal Fiber-Optic Array Probe in the Presence of Raman Photon Migration," *Appl. Spectrosc.* 60(2), 109-114 (2006)
12. J. Ma and D. Ben-Amotz, "Rapid Micro-Raman Imaging Using Fiber-Bundle Image Compression " *Appl. Spectrosc.* 51(12), 1845-1848 (1997)
13. M. L. Myrick and S. M. Angel, "Elimination of Background in Fiber-Optic Raman Measurements," *Appl. Spectrosc.* 44(4), 565-570 (1990)
14. M. V. Schulmerich, M. D. Morris, T. M. Vanasse and S. A. Goldstein, "Transcutaneous Raman spectroscopy of bone: global sampling and ring/disk fiber optic probes," *Proc. SPIE* 6430(643009), 1-8 (2007)
15. P. Matousek, "Inverse Spatially Offset Raman Spectroscopy for Deep Noninvasive Probing of Turbid Media " *Appl. Spectrosc.* 60(11), 1341-1347 (2006)
16. D. Zhang, J. D. Hanna, Y. Jiang and D. Ben-Amotz, "Influence of Laser Illumination Geometry on the Power Distribution Advantage," *Appl. Spectrosc.* 55(1), 61-65 (2001)
17. A. D. Klose, V. Ntziachristos and A. H. Hielscher, "The inverse source problem based on the radiative transfer equation in optical molecular imaging," *J Comp Phys* 202(1), 323-345 (2005)
18. A. B. R. Roy, A. Thompson, Godavarty and E. M. Sevick-Muraca, "Tomographic Fluorescence Imaging in Tissue Phantoms: A Novel Reconstruction Algorithm and Imaging Geometry," *IEEE Trans Med Image* 24(2), 137-154 (2005)
19. A. Joshi, W. Bangerth, K. Hwang, J. Rasmussen and E. M. Sevick-Muraca, "Plane-wave fluorescence tomography with adaptive finite elements," *Opt. Lett.* 31(2), 193-195 (2006)

20. B. W. Pogue, S. C. Davis, X. Song, B. A. Brooksby, H. Dehghani and K. D. Paulsen, "Image analysis methods for diffuse optical tomography," *J. Biomed. Opt.* 11(3), 0330015 (2006)
21. B. W. Pogue, B. Chen, X. Zhou and P. J. Hoopes, "Analysis of sampling volume and tissue heterogeneity on the in vivo detection of fluorescence," *J. Biomed. Opt.* 10(4), 041206 (2005)
22. S. C. Davis, B. W. Pogue, H. Dehghani and K. D. Paulsen, "Contrast-detail analysis characterizing diffuse optical fluorescence tomography image reconstruction" *J. Biomed. Opt.* 10(5), 050501 (2005)
23. B. Brooksby, S. Srinivasan, S. Jiang, H. Dehghani, B. W. Pogue, K. D. Paulsen, J. Weaver, C. Kogel and S. P. Poplack, "Spectral priors improve near-infrared diffuse tomography more than spatial priors," *Opt. Lett.* 30(15), 1968-1970 (2005)
24. W. Cong, G. Wang, D. Kumar, Y. Liu, M. Jiang, L. V. Wang, E. A. Hoffman, G. McLennan, P. B. McCray, J. Zabner and A. Cong, "Practical reconstruction method for bioluminescence tomography," *Opt. Express* 13(18), 6756-6771 (2005)
25. H. Dehghani, C. M. Carpenter, P. K. Yalavathy, B. W. Pogue and J. P. Culver, "Structural a-priori Information in Near Infrared Optical Tomography," *Proc. SPIE* 6431(B), 1-7 (2007)
26. H. Dehghani, B. W. Pogue, S. C. Davis and M. S. Patterson, "Modeling and Image Reconstruction in Spectrally resolved Bioluminescence Tomography," *Proc. SPIE* 6434(V), 1-9 (2007)
27. F. J. Harris, "On the Use of Windows for Harmonic Analysis with the Discrete Fourier Transform," *Proc. IEEE* 66(1), 51-83 (1978)
28. W. Chew, E. Widjaja and M. Garland, "Band-Target Entropy Minimization (BTEM): An Advanced Method for Recovering Unknown Pure Component Spectra. Application to the FTIR Spectra of Unstable Organometallic Mixtures," *Organometallics* 21, 1982-1990 (2002)
29. L. Guo, F. Kooli and M. Garland, "A general method for the recovery of pure powder XRD patterns from complex mixtures using no a priori information Application of band-target entropy minimization (BTEM) to materials characterization of inorganic mixtures," *Anal. Chim. Acta* 517, 229-236 (2004)

30. L. R. Ong, E. Widjaja, R. Stanforth and M. Garland, "Fourier transform Raman spectral reconstruction of inorganic lead mixtures using a novel band-target entropy minimization (BTEM) method," *J. Raman Spectrosc.* 34, 282-289 (2003)
31. E. Widjaja, N. Crane, T.-C. Chen, M. D. Morris, M. A. Ignelzi and B. R. McCreadie, "Band-Target Entropy Minimization (BTEM) Applied to Hyperspectral Raman Image Data," *Appl. Spectrosc.* 57(11), 1353-1362 (2003)
32. E. Widjaja, C. Li and M. Garland, "Semi-Batch Homogeneous Catalytic In-Situ Spectroscopic Data. FTIR Spectral Reconstructions Using Band-Target Entropy Minimization (BTEM) without Spectral Preconditioning," *Organometallics* 21, 1991-1997 (2002)
33. C. A. Lieber and A. Mahadevan-Jansen, "Automated Method for Subtraction of Fluorescence from Biological Raman Spectra," *Appl. Spectrosc.* 57(11), 1363-1367 (2003)
34. B. R. McCreadie, M. D. Morris, T.-C. Chen, D.S.Rao, W. F. Finney, E. Widjaja and S. A. Goldstein, "Bone Extracellular Matrix Compositional Differences in Women with and without Osteoporotic Fracture," *Bone* 39, 1190-1195 (2006)



# **CHAPTER VI**

## **OPTICAL CLEARING IN TRANSCUTANEOUS RAMAN SPECTROSCOPY OF MURINE CORTICAL BONE TISSUE**

### **Introduction**

To realize the potential of transcutaneous Raman spectroscopy it is necessary to develop both spectroscopic instrumentation for transcutaneous measurements of bone tissue composition and ancillary techniques, such as optical clearing,<sup>10</sup> that enhance the recovery of subsurface spectra. Skin presents a formidable barrier to bone Raman spectroscopy, both because the tissue, especially the stratum corneum, is highly scattering, and because melanocytes, which contain the skin pigment melanin, absorb even in the near-infrared (NIR) spectrum and fluoresce intensely. Raman spectroscopy has been used to study skin and skin diseases.<sup>11-13</sup> To date, dermatological Raman spectroscopy has aimed primarily to measure the moisture content and drug penetration in skin at depths that do not exceed 1 mm.<sup>14, 15</sup> Similarly, arterial plaque<sup>16-18</sup> and blood components<sup>12, 19-21</sup> have been measured using arteries that lie close to the surface of the skin.

Although it has not previously been applied to Raman spectroscopy, optical clearing is well-known in other areas of biomedical optics, including NIR spectroscopy and optical coherence tomography.<sup>10, 22-25</sup> With this methodology, a liquid is used to

penetrate the stratum corneum and displace the native water, because it has an index of refraction that is closer to that of proteins. Clearing agents may also disrupt the internal hydrogen bonding of collagen, which partially disorders the fibrils and increases their transparency.<sup>22, 26</sup> The use of an optical clearing agent decreases scattering, thereby increasing light penetration into the tissue.<sup>10</sup> Glycerol is one of the most commonly employed clearing agents. It is non-toxic, has a high index of refraction ( $n_D = 1.47$ ) and disrupts the internal hydrogen bonding of collagen. For these reasons we have used glycerol in this study.

With the development of spatially-resolved Raman spectroscopy,<sup>27, 28</sup> transcutaneous measurements at depths of several millimeters or greater have become feasible. In human cadaveric tissue, we have shown that transcutaneous bone Raman spectra can be obtained with a commercially available fiber optic probe that uses distributed laser power and an array of collection fibers.<sup>29, 30</sup> Using a recently developed ring/disk probe,<sup>31-33</sup> we have demonstrated the recovery of Raman spectra from canine bone tissue at a depth of 5 mm below the skin surface.<sup>34</sup> This work demonstrated several difficulties that must be addressed in the development of non-invasive bone Raman spectroscopy. These include a high background fluorescence, multiple scattering that is characteristic of almost all tissue,<sup>35-37</sup> and the limitations of existing fiber optic Raman probes.

In this communication we discuss the use of optical clearing to improve the Raman signal and reduce the effects of scattering. We show that a very simple protocol with glycerol as a clearing agent increases the signal-to-noise ratio and reduces the systematic error incurred as a result of incompletely resolved surface and subsurface

spectra using multivariate techniques. We also demonstrate a fiber probe with line-focused laser delivery that is better suited to small animal limb studies than ring-focused probes.

## **Materials and Methods**

The specimens used for *in vitro* transcutaneous Raman measurements through skin and overlying tissue were tibiae from mice sacrificed between the ages of 12 and 20 weeks in the course of other unrelated studies. These mice were sacrificed according to study designs and protocols approved by the University of Michigan Committee on Use and Care of Animals. Both tibiae from healthy female animals from four randomly selected mice strains were used.

The depilatory agent was Sally Hansen Hair Removal Lotion (Sally Hansen Corp, Uniondale, NY.). The optical clearing agent was American Chemical Society reagent grade glycerol (Sigma-Aldrich Corp., Milwaukee, WI ).

A schematic of the Raman instrument is shown in figure 6.1. A 400 mW, 785 nm external cavity diode laser (Invictus, Kaiser Optical Systems, Inc., Ann Arbor, MI) was used for excitation. The laser beam was passed through a 200  $\mu\text{m}$  core NIR optical fiber (PCN200 4-FF-HT-GN, Multimode Fiber Optics, Hackettstown, NJ). The light was collimated with a fiber optic collimator (F230FC-B, Thorlabs Inc., Newton, NJ) and directed through a 5° fan angle Powell lens/collimating optics assembly (C10, StockerYale Montreal, Quebec, Canada) and a 75 mm focal length NIR coated achromat (AC254-075-B, Thorlabs Inc., Newton, NJ) to obtain a 3 mm by 0.75 mm line

illumination. A non-confocal fiber optic probe (PhAT probe, Kaiser Optical Systems, Inc.) was employed to collect backscattered Raman shifted light and present it to the spectrograph. The probe contained a circular bundle of fifty 100  $\mu\text{m}$  core collection fibers. At the probe head a 75 mm focal length lens was employed to obtain a 3 mm diameter circular field of view. A dichroic mirror (Chroma Technology Corp., Rockingham, VT) reflected the 785 nm light to the sample and transmitted the Raman signal to the collection fibers. A NIR-optimized imaging spectrograph (HoloSpec f/1.8i, Kaiser Optical Systems) fitted with a 50  $\mu\text{m}$  slit was used to provide a 6-8  $\text{cm}^{-1}$  spectral resolution. The detector was a thermoelectrically cooled, deep-depletion 1024x256 pixel charged-coupled device camera (CCD) (DU420-BR-DD, Andor Technology, Belfast, Northern Ireland) operated at  $-75^{\circ}\text{C}$  with no binning.

Transcutaneous Raman spectroscopic measurements were made on intact, sacrificed animals. Prior to measurement, the depilatory lotion was used on the tibiae to facilitate hair removal with a tissue paper wipe from the region of interest. Excess depilatory was rinsed off with distilled water after hair removal was complete. After transcutaneous measurements, the entire tibia was excised, and overlying tissue was removed with a scalpel. The Raman spectrum of the exposed bone was then measured in the same region.

Transcutaneous Raman spectra were acquired with the illumination line and the collection disk focused onto the skin at the medial side of the tibia mid-diaphysis just below the tibial proximal tuberosity. The laser line was positioned so that the long axis of the line was parallel to the bone and centered over the bone. The power of the laser light at the specimen was 35 mW. The acquisition time was 300 s for transcutaneous

measurements and 120s for exposed bone measurements. For optical clearing experiments, glycerol was applied topically with a cotton swab. The glycerol was left to diffuse into the skin for approximately three minutes before spectra were acquired.

For six of the tibiae, seven sequential replicate spectra were acquired prior to optical clearing. After application of glycerol and a three minute wait, seven replicate spectra were acquired in the same location. For one of the tibiae, only five measurements were taken before optical clearing and five afterwards. After the sequence of transcutaneous measurements was completed, soft tissue was removed, and twenty consecutive Raman spectra of the exposed bone were acquired.

Data reduction was performed in MATLAB 6.1 (The Mathworks Inc., Natick, MA) using vendor-supplied scripts and locally-written scripts that have been described previously. Statistical analyses were performed in SAS, version 9.1 (SAS Institute Inc., Cary, NC).

A single CCD frame contained 256 Raman spectra. Initial preprocessing included CCD calibration against a neon discharge lamp, with a check against a Teflon® Raman spectrum. White light correction and dark current subtraction were used to account for the spectral response of the detector. The image was then corrected for curvature caused by the large gathering angle of the spectrograph.

The spectrum from each of the fifty collection fibers of the probe was imaged onto slightly more than 5 rows of the CCD. To avoid cross-talk, spectra from only the central three rows of each fiber image were used. These three spectra were averaged to generate one spectrum for each collection fiber. Finally, the 905-1500  $\text{cm}^{-1}$  region of interest (ROI) was selected. This region contains the mineral phosphate P-O and

carbonate C-O stretches and matrix bands including collagen amide III and CH<sub>2</sub> wag.<sup>2, 8,</sup>

38

The amount of noise in the transcutaneous measurements was quantified using spectral averages, that is, without background correction and without separation into bone and overlying tissue components. The three spectra from each of the fifty collection fibers were averaged, and the power spectrum of each averaged spectrum was computed. For this purpose, the dispersion axis was not converted to wavenumber, but was left in wavelength (nm) so that the noise contribution from each pixel would be equally weighted. The root-mean-square (rms) value was calculated for the high transform frequency region between 0.02 cycles/nm and 0.07 cycles/nm. Data from one tibia was excluded, because the probe was improperly aligned during the measurements. For each of the remaining six tibiae, the mean rms values were computed for each of the seven sequential acquisitions.

For each tibia, a paired t-test was used to assess the difference in rms noise magnitudes between spectra of each tibia acquired with and without optical clearing. The effect of optical clearing on the noise rms values was examined for all six tibiae using a repeated measures analysis of variance (ANOVA). Using a mixed-effects model<sup>39</sup>, optical clearing was treated as a fixed factor with two levels (glycerol-treated, controls). The repeated measure was the series of measurements made on each mouse. The series had seven (or five) levels and was treated as a random effect. A significance level of 0.05 was used for all statistical calculations.

Recovery of a bone factor for each transcutaneous measurement followed previously described procedures.<sup>40</sup> An iterative background removal with a 5<sup>th</sup>-order

polynomial was used to subtract the background fluorescence.<sup>41,42</sup> The resulting spectra were normalized, the covariance matrix was calculated, and band target entropy minimization (BTEM)<sup>40,43,44</sup> was used to recover the spectral factors. A 3 cm<sup>-1</sup> interval around the phosphate band (ca. 959 cm<sup>-1</sup>) was chosen for band targeting. Between 3 and 23 eigenvectors from the data set were included for the calculation of Raman spectral factors. Eigenvectors containing predominantly random noise were used to improve the signal-to-noise ratio of the recovered bone spectra. An eigenvector weight distribution test for selecting the appropriate number of eigenvectors was used, as described elsewhere<sup>40</sup>. A stopping point was reached when additional eigenvectors added only noise.

Once the bone spectral factors were calculated, the cross-correlation coefficient between the bone factor and the exposed bone measurement was calculated using the 'xcorr' function of the Matlab signal processing toolbox. To exclude the intense P-O stretch, while including enough of the spectrum for computation, the interval used was 988-1500cm<sup>-1</sup>. The mean cross-correlation coefficient was computed for the average of the spectra from each of the six tibiae. For each tibia, a paired t-test, as described above, was used to examine the difference in the cross-correlation coefficients between transcutaneous spectra measured with and without optical clearing. The effect of optical clearing on the correlation between transcutaneous and exposed bone measurements was tested for all six tibiae using a repeated measures ANOVA. Optical clearing was treated as a fixed factor with two levels (glycerol-treated, controls), and the repeated measure was the series of measurements on each mouse, which had seven (or five) levels and was treated as a random effect.

## Results and Discussion

Transcutaneous Raman spectra taken through approximately 1mm of tissue on a mouse tibia are shown in figure 6.2a. CCD white light correction, dark current subtraction, and correction of spectrograph-induced curvature was applied, but no further processing was done. The measurements made after glycerol application have visibly less intense and more reproducible background fluorescence than those from the control spectra, which were acquired prior to optical clearing. The power spectra for these Raman spectra are shown in figure 6.2b. In the high transform frequency region ( $> 0.02$  cycles/nm), where mostly noise is represented, the measurements made after optical clearing have both lower noise power and reduced measurement-to-measurement variability.

We attribute the spectroscopic effects of optical clearing to reduced specimen fluorescence in the acquired spectra. With 785 nm excitation the most important source of fluorescence is melanin, which is located in the melanocytes. In mice, as in humans and other mammals the melanocytes lie just below the stratum corneum.<sup>45</sup> Decreasing the scattering at and just below the skin surface decreases the amount of fluorescence that is generated and the amount reaching the collection fibers, thereby decreasing its contribution to the total collected signal. Some photobleaching may also be occurring during the first few minutes of laser illumination. The background decreases rapidly between the first and second spectrum acquisition but slowly thereafter (figure 6.2a).

Bar graphs of noise levels and measurement variability for each tibia are shown in figure 6.3a. The measurements taken after optical clearing had a significantly lower



noise level ( $p < 0.05$ ) in 4 out of the 6 tibiae. In addition, the variability in a set of spectra, indicated by the error bars, was lower for spectra acquired after the application of glycerol, although the differences were not statistically significant in tibiae 2 and 6. The mean noise levels for the six tibiae are presented in figure 6.3b. The spectra acquired after optical clearing have significantly less noise ( $p = 0.0037$ ).

Recovery of the bone spectrum depends on separation of the bone component from that of the overlying tissue, which includes skin, tendon, blood vessels and even some adipose tissue. Optical clearing can actually degrade the recovered bone spectrum if the fiber optic probe is not aligned so as to maximize the contribution from bone and minimize the contribution from overlying tissue. This effect is illustrated in figure 6.4. The illumination line must be positioned directly over the bone, and the collection fibers must be centered on this line, as shown in figure 6.4a. The field of view of the collection fibers is then as illustrated in figure 6.4b.

However, if the collection fibers are not positioned directly over the bone and centered on the illumination line, spectra from soft tissue are over-sampled. We demonstrated these effects by misaligning the probe. The field of view of the collection fibers was shifted toward the medial side of the tibia while the illumination line centered over the bone. The improper collection fiber alignment is shown in figure 6.4c. The rms noise for the control and optical clearing cases are shown in Figure 6.4d. Significantly more noise was observed in the measurement made after glycerol application ( $p < 0.00001$ ). This seemingly contradictory result is caused by the reduction of light scattering by the skin, allowing oversampling of Raman scatter from the soft tissue directly below. As expected, the overall intensity of the bone component of the

recovered spectrum is decreased. The effect is seen most clearly in the phosphate  $\nu_1$  band at  $959\text{ cm}^{-1}$  (figure 6.4e). The absolute intensity of the phosphate  $\nu_1$  band recovered with the misaligned probe is not as great as that obtained when the probe is properly aligned. Because the signal-to-noise ratio is reduced and the contribution from skin and tendon collagen is increased by probe misalignment, the accuracy of the recovered bone factor is also lowered.

The cross-correlation coefficients between bone factors recovered from transcutaneous and exposed bone spectra further illustrate the effects of optical clearing. Because in the mouse tibia the bone lies only about 1 mm below the skin, a strong phosphate  $\nu_1$  band is actually visible in the spectrum, after removal of fluorescence background (figure 6.5). The Raman spectrum of type I collagen in skin and tendon is similar to that of type I collagen in bone. As a consequence the collagen bands are much more intense than the similar bands in exposed bone, as comparison to the exposed bone spectrum shows. Collagen bands near the  $1070\text{ cm}^{-1}$  region effectively mask the carbonate  $\nu_1$  band at  $1070\text{ cm}^{-1}$ . By reducing the skin collagen contribution, optical clearing with glycerol improves the accuracy of the recovered bone factor, as shown in figure 6.5b. The difference is clearest in the less intense bands.

To quantify the difference between the recovered bone factors and the exposed bone measurements, cross-correlation coefficients were calculated in the low signal-to-noise portion of the recovered spectra, i.e., excluding the phosphate  $\nu_1$  band (figure 6.6). The spectra acquired after optical clearing had a significantly higher correlation with the exposed bone spectra ( $p < 0.07$ ) in 4 of the 6 tibiae. The mean cross-correlation coefficients are shown in figure 6.6b. The measurements made after optical clearing

have a significantly higher correlation with the exposed bone spectra ( $p=0.025$ ) than those of controls, without optical clearing.

## **Conclusions**

Optical clearing improves the signal-to-noise ratio of transcutaneously measured bone Raman spectra. Our initial experiments employed only one clearing agent, glycerol, and a simple protocol. Glycerol was chosen, because it is known to be effective and safe for use on humans. Other clearing agents and application protocols may prove even more effective. For example, dermabrasion to remove a portion of the stratum corneum is known to improve penetration of clearing agents. Compression or stretching of the skin has also been shown to improve light transmission.<sup>10</sup> The use of one or more of these techniques should allow transcutaneous measurement of bone Raman spectra with an even better signal-to-noise ratio.

Further development of the line-focused probe could also improve the performance of the system. The available Powell lens assembly was not coated for 785 nm, nor was its internal collimator adjustable to correct for beam divergence. As a result, throughput was reduced. The delivered power was 35 mW from a 400 mW laser. Unlike the ring/disk system, the present configuration does not allow for adjustment of the distance between the entry and collection points. Moreover, the collection fibers are arranged in a disk, resulting in under-sampling of the offset points at the periphery of the field of view. These problems can be mitigated with a rectangular collection fiber array

and line-forming optics that are designed to work properly with the 785 nm output from a multimode optical fiber.

## Figures

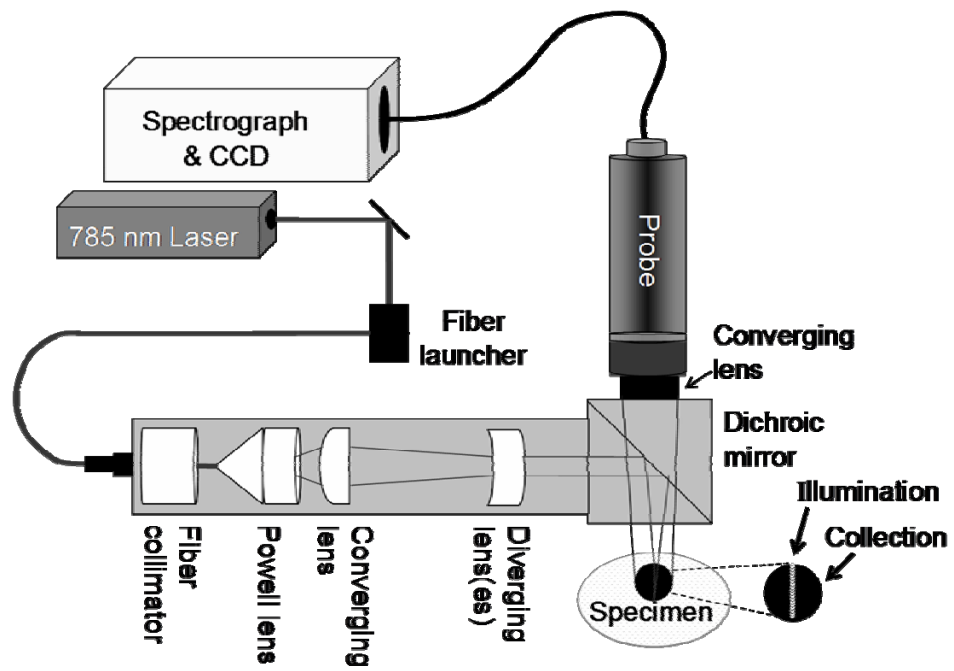


Figure 6.1: Schematic of experimental apparatus

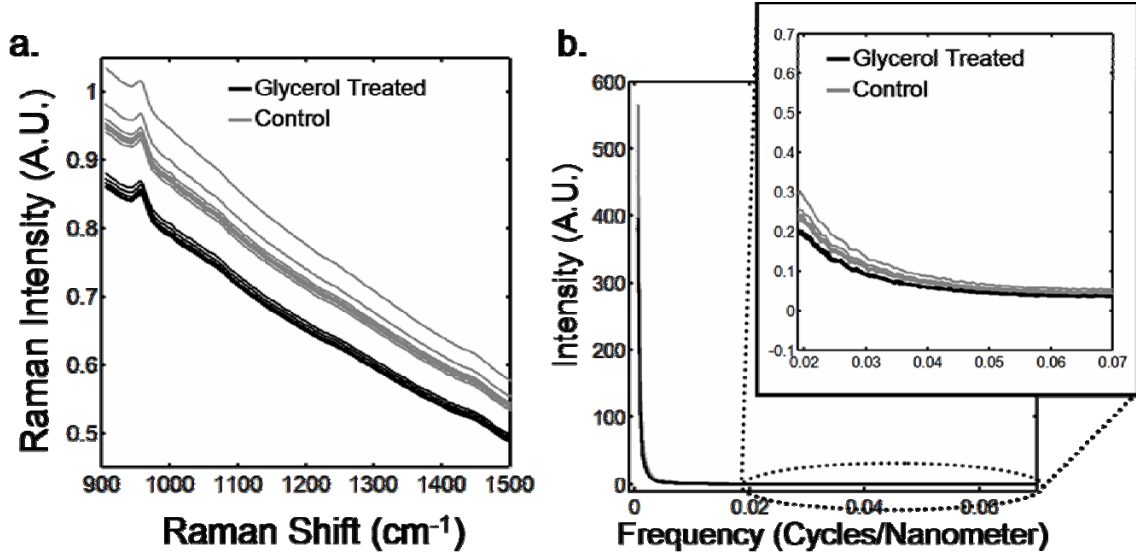


Figure 6.2: Raman spectra of a murine tibia (distal diaphysis). The bone tissue is approximately 1 mm below the skin. The gray traces are raw spectra obtained without optical clearing, and the black traces are spectra obtained after glycerol application (a) Transcutaneous Raman spectra (b) Power spectra

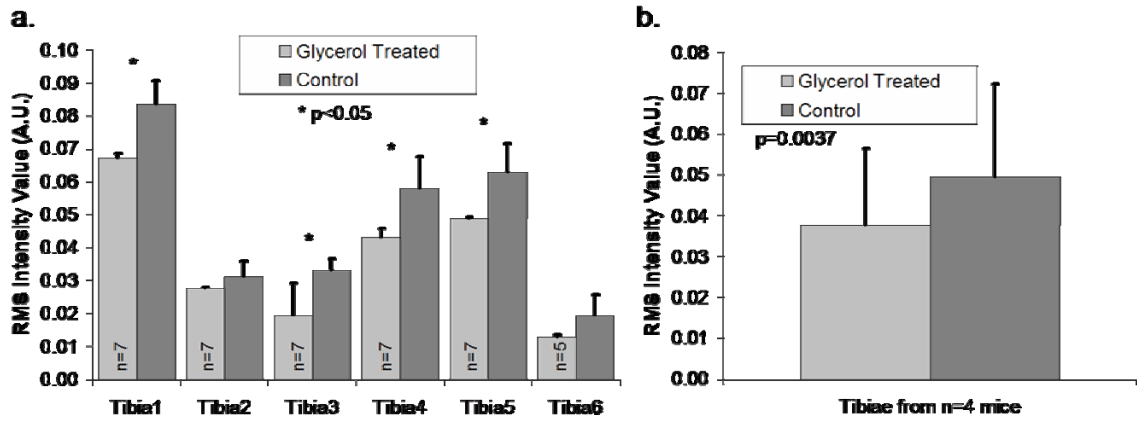


Figure 6.3: rms intensity for power spectra in high transform frequency region (mean + standard deviation) (a) Results for measurements made on six different tibiae (b) Results across tibiae from all mice

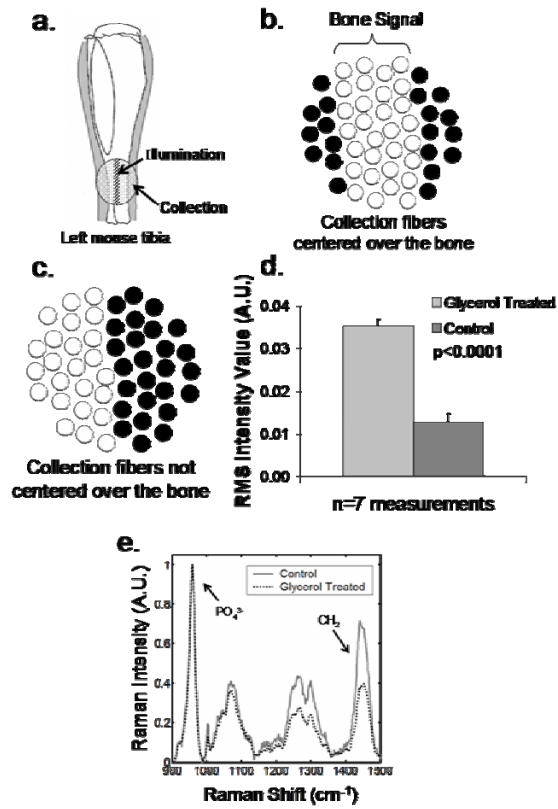


Figure 6.4: Effect of not centering the illumination line in the center of the collection fibers (a) Correct alignment of illumination line and collection disk with respect to the bone (b) Field of view of the collection fibers for proper alignment (c) Field of view of the collection fibers for improper alignment (d) Resulting noise levels in measurements made with improper alignment (compare to Fig. 3) (e) Mean transcutaneous spectra, after baselining and normalizing, for a measurement before and after glycerol application



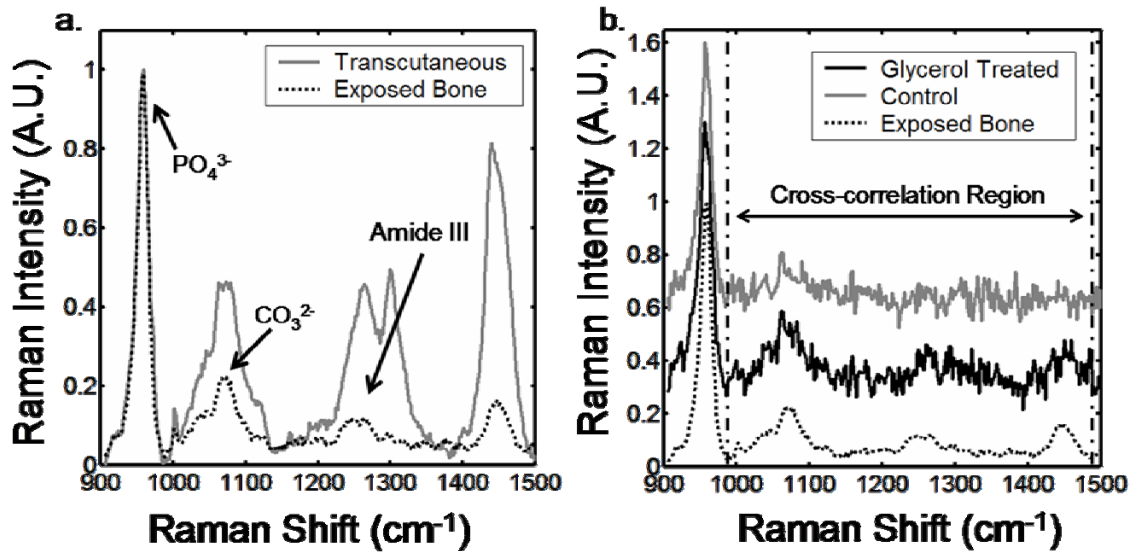


Figure 6.5: (a) Typical mean transcutaneous spectrum (gray) and typical mean exposed bone spectrum (black) (b) Recovered bone factor without an optical clearing agent (gray), recovered bone factor after glycerol application (black), and exposed bone measurement (dotted)

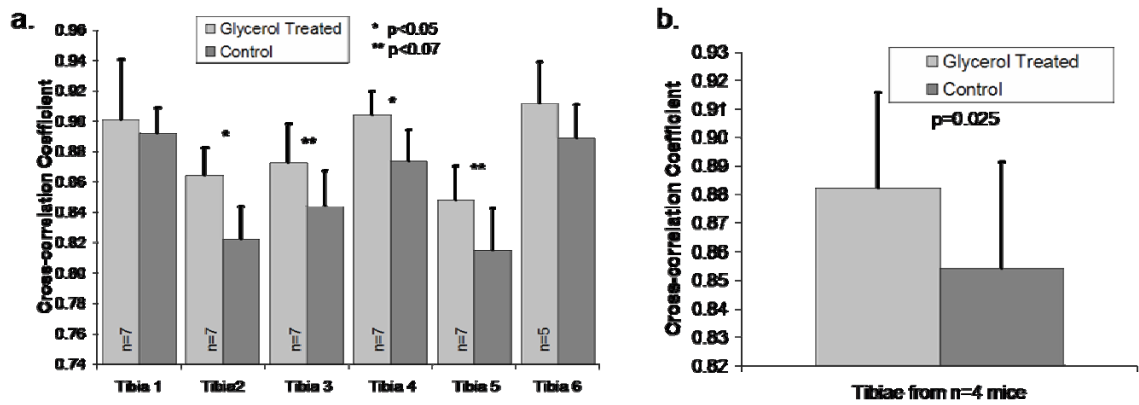


Figure 6.6: Cross-correlation coefficient between the exposed bone measurement and the recovered bone factor (mean + standard deviation) (a) Results for measurements made on six different tibiae (b) Results across tibiae from all mice

## References

1. K. M. Kozloff, A. Carden, C. Bergwitz, A. Forlino, T. E. Uveges, M. D. Morris, J. C. Marini and S. A. Goldstein, "Brittle IV Mouse Model for Osteogenesis Imperfecta IV Demonstrates Postpubertal Adaptations to Improve Whole Bone Strength," *J. Bone Miner. Res.* 19(4), 614-622 (2004)
2. C. P. Tarnowski, M. A. Ignelzi Jr. and M. D. Morris, "Mineralization of Developing Mouse Calvaria as Revealed by Raman Microspectroscopy," *J. Bone Miner. Res.* 17(6), 1118-1126 (2002)
3. C. P. Tarnowski, M. A. Ignelzi Jr., W. Wang, J. M. Taboas, S. A. Goldstein and M. D. Morris, "Earliest Mineral and Matrix Changes in Force-Induced Musculoskeletal Disease as Revealed by Raman Microspectroscopic Imaging," *J. Bone Miner. Res.* 19(1), 64-71 (2004)
4. D. H. Kohn, N. D. Sahar, S. I. Hong, K. Golcuk and M. D. Morris, "Local Mineral and Matrix Changes Associated with Bone Adaptation and Microdamage," *Mater. Res. Soc. Symp. Proc.* 898E, 1-11 (2006)
5. A. Carden, R. M. Rajachar, M. D. Morris and D. H. Kohn, "Ultrastructural Changes Accompanying the Mechanical Deformation of Bone Tissue: A Raman Imaging Study," *Calcif. Tissue Int.* 72, 166-175 (2003)
6. T.-C. Chen, K. Kozloff, S. Goldstein and M. Morris, "Bone Tissue Ultrastructural Defects in a mouse model for Osteogenesis Imperfecta: a Raman Spectroscopy Study," *Proc. SPIE* 5321, 85 (2004)
7. D. Faibish, S. M. Ott and A. L. Boskey, "Mineral Changes in Osteoporosis a Review," *Clin. Orthop. Relat. Res.* 443, 28-38 (2006)
8. B. R. McCreadie, M. D. Morris, T.-C. Chen, D.S.Rao, W. F. Finney, E. Widjaja and S. A. Goldstein, "Bone Extracellular Matrix Compositional Differences in Women with and without Osteoporotic Fracture," *Bone* 39, 1190-1195 (2006)
9. K. A. Dehring, N. J. Crane, A. R. Smukler, J. B. McHugh, B. J. Roessler and M. D. Morris, "Identifying Chemical Changes in Subchondral Bone Taken from Murine Knee Joints Using Raman Spectroscopy," *Appl. Spectrosc.* 60(10), 1134-1141 (2006)

10. V. Tuchin, *Optical Clearing of Tissue and Blood*, SPIE Press, Bellingham, (2006).
11. N. S. Eikje, Y. Ozaki, K. Aizawa and S. Arase, "Fiber optic near-infrared Raman spectroscopy for clinical noninvasive determination of water content in diseased skin and assessment of cutaneous edema," *J. Biomed. Opt.* 10(1), 14013 (2005)
12. P. J. Caspers, G. W. Lucassen and G. J. Puppels, "Combined In Vivo Confocal Raman Spectroscopy and Confocal Microscopy of Human Skin," *Biophys. J.* 85, 572-580 (2003)
13. B. R. Hammond and B. R. Wooten, "Resonance Raman spectroscopic measurement of carotenoids in the skin and retina.," *J. Biomed. Opt.* 10(5), 054002 (2005)
14. P. J. Caspers, A. C. Williams, E. A. Carter, H. G. M. Edwards, B. W. Barry, H. A. Bruining and G. J. Puppels, "Monitoring the Penetration Enhancer Dimethyl Sulfoxide in Human Stratum Corneum in Vivo by Confocal Raman Spectroscopy," *Pharm. Res.* 19(10), 1577-1580 (2002)
15. Y. Song, C. Xiao, R. Mendelsohn, T. Zheng, L. Strekowski and B. Michniak, "Investigation of iminosulfuranes as novel transdermal penetration enhancers: enhancement activity and cytotoxicity.," *Pharm. Res.* 22(11), 1918-1925 (2005)
16. J. T. Motz, M. Fitzmaurice, A. Miller, S. J. Gandhi, A. S. Haka, L. H. Galindo, R. R. Dasari, J. R. Kramer and M. S. Feld, "In vivo Raman spectral pathology of human atherosclerosis and vulnerable plaque," *J. Biomed. Opt.* 11(2), 021003 (2006)
17. J. T. Motz, S. J. Gandhi, O. R. Scepanovic, A. S. Haka, J. R. Kramer, R. R. Dasari and M. S. Feld, "Real-time Raman system for in vivo disease diagnosis," *J. Biomed. Opt.* 10(3), 031113 (2005)
18. O. R. Scepanovic, M. Fitzmaurice, J. A. Gardecki, G. O. Angheloiu, S. Awasthi, J. T. Motz, J. R. Kramer, R. R. Dasari and M. S. Feld, "Detection of morphological markers of vulnerable atherosclerotic plaque using multimodal spectroscopy," *J. Biomed. Opt.* 11(2), 021007 (2006)
19. A. M. K. Enejder, T.-W. Koo, J. Oh, M. Hunter, S. Sasic and M. S. Feld, "Blood analysis by Raman spectroscopy," *Opt. Lett.* 27(22), 2004-2006 (2003)

20. A. M. K. Enejder, T. G. Scecina, J. Oh, M. Hunter, W.-C. Shih, S. Sasic, G. L. Horowitz and M. S. Feld, "Raman spectroscopy for noninvasive glucose measurements," *J. Biomed. Opt.* 10(3), 031114 (2005)
21. S. Pilotto, M. T. T. Pacheco, L. Silveira Jr, A. Balbin Villaverde and R. A. Za<sup>^</sup>ngaro, "Analysis of Near-infrared Raman Spectroscopy as a New Technique for a Transcutaneous Non-invasive Diagnosis of Blood Components," *Lasers Med. Sci.* 16(1), 2-9 (2001)
22. A. T. Yeh and J. Hirshburg, "Molecular interactions of exogenous chemical agents with collagen—implications for tissue optical clearing," *J. Biomed. Opt.* 11(1), 014003 (2006)
23. R. Cicchi, D. Massi, D. Stambouli, D. D. Sampson and F. S. Pavone, "Contrast enhancement in combined two-photon second harmonic imaging of skin by using hyperosmotic agents," *Proc. SPIE* 6089, 60890X (2006)
24. X. Xu and R. K. Wang, "The role of water desorption on optical clearing of biotissue: Studied with near infrared reflectance spectroscopy," *Med. Phys.* 30(6), 1246-1253 (2003)
25. Y. He and R. K. Wang, "Dynamic optical clearing effect of tissue impregnated with hyperosmotic agents and studied with optical coherence tomography," *J. Biomed. Opt.* 9(1), 200-206 (2004)
26. A. T. Yeh, B. Choi, J. S. Nelson and B. J. Tromberg, "Reversible Dissociation of Collagen in Tissues," *J. Invest. Derm.* 121(6), 1332-1335 (2003)
27. P. Matousek, I. P. CLark, E. R. C. Draper, M. D. Morris, A. E. Goodship, N. Everall, M. Towrie, W. F. Finney and A. W. Parker, "Subsurface Probing in Diffusely Scattering Media Using Spatially Offset Raman Spectroscopy," *Appl. Spectrosc.* 59(4), 393-400 (2005)
28. P. Matousek, M. D. Morris, N. Everall, I. P. Clark, M. Towrie, E. Draper, A. Goodship and A. W. Parker, "Numerical Simulations of Subsurface Probing in Diffusely Scattering Media Using Spatially Offset Raman Spectroscopy " *Appl. Spectrosc.* 59(12), 1485-1492 (2005)
29. M. V. Schulmerich, W. F. Finney, V. Popescu, M. D. Morris, T. M. Vanasse and S. A. Goldstein, "Transcutaneous Raman spectroscopy of bone tissue using a non-confocal fiber optic array probe," *Proc. SPIE* 6093(O1-O7 (2006)

30. M. V. Schulmerich, W. F. Finney, R. A. Fredricks and M. D. Morris, "Subsurface Raman Spectroscopy and Mapping Using a Globally Illuminated Non-Confocal Fiber-Optic Array Probe in the Presence of Raman Photon Migration," *Appl. Spectrosc.* 60(2), 109-114 (2006)
31. M. V. Schulmerich, K. A. Dooley, M. D. Morris, T. M. Vanasse and S. A. Goldstein, "Transcutaneous fiber optic Raman spectroscopy of bone using annular illumination and a circular array of collection fibers," *J. Biomed. Opt.* 11(6), 060502 (2006)
32. M. V. Schulmerich, M. D. Morris, T. M. Vanasse and S. A. Goldstein, "Transcutaneous Raman spectroscopy of bone: global sampling and ring/disk fiber optic probes," *Proc. SPIE* 6430(643009), 1-8 (2007)
33. P. Matousek, "Inverse Spatially Offset Raman Spectroscopy for Deep Noninvasive Probing of Turbid Media " *Appl. Spectrosc.* 60(11), 1341-1347 (2006)
34. M. V. Schulmerich, K. A. Dooley, T. M. Vanasse, S. A. Goldstein and M. D. Morris, "Subsurface and Transcutaneous Raman Spectroscopy and Mapping Using Concentric Illumination Rings and Collection with a Circular Fiber-Optic Array," *Appl. Spectrosc.* 61(7), 671-678 (2007)
35. R. Richards-Kortum and E. Sevick-Muraca, "Quantitative Optical Spectroscopy for Tissue Disagnosis," *An. Rev. Phys. Chem.* 47, 555-606 (1996)
36. V. Tuchin, *Tissue Optics Light Scattering Methods and Instruments for Medical Diagnosis*, SPIE Press, Bellingham, (2000).
37. T. Vo-Dinh, *Biomedical Photonics Handbook*, CRC Press, Boca Raton (2003).
38. A. Carden and M. D. Morris, "Application of vibrational spectroscopy to the study of mineralized tissues (review)," *J. Biomed. Opt.* 5(3), 259-268 (2000)
39. J. L. Devore, *Probability and statistics for engineering and the sciences*, Thomson Brooks/Cole, Toronto (2004).
40. E. Widjaja, N. Crane, T.-C. Chen, M. D. Morris, M. A. Ignelzi and B. R. McCreadie, "Band-Target Entropy Minimization (BTEM) Applied to Hyperspectral Raman Image Data," *Appl. Spectrosc.* 57(11), 1353-1362 (2003)

41. M. Leger and A. Ryder, "Comparison of Derivative Preprocessing and Automated Polynomial Baseline Correction Method for Classification and Quantification of Narcotics in Solid Mixtures," *Appl. Spectrosc.* 60(2), 182-193 (2006)
  
42. C. A. Lieber and A. Mahadevan-Jansen, "Automated Method for Subtraction of Fluorescence from Biological Raman Spectra," *Appl. Spectrosc.* 57(11), 1363-1367 (2003)
  
43. W. Chew, E. Widjaja and M. Garland, "Band-Target Entropy Minimization (BTEM): An Advanced Method for Recovering Unknown Pure Component Spectra. Application to the FTIR Spectra of Unstable Organometallic Mixtures," *Organometallics* 21, 1982-1990 (2002)
  
44. E. Widjaja, C. Li and M. Garland, "Semi-Batch Homogeneous Catalytic In-Situ Spectroscopic Data. FTIR Spectral Reconstructions Using Band-Target Entropy Minimization (BTEM) without Spectral Preconditioning," *Organometallics* 21, 1991-1997 (2002)
  
45. R. A. Briggaman and C. E. Wheeler Jr., "The Epidermal-Dermal Junction," *J. Invest. Derm.* 65(1), 71-84 (1975)

**CHAPTER VII**  
**TRANSCUTANEOUS RAMAN SPECTROSCOPY OF MURINE**  
**BONE *IN VIVO***

**Introduction**

Raman measurements are generally performed *ex vivo*. Noninvasive *in vivo* measurements would improve the state-of-the-art by allowing tissue to be monitored without perturbation, leading to a greater understanding of the development, biomechanics, and health of bone. The current limitation is that instrumentation and methods have not yet been optimized for transcutaneous *in vivo* Raman spectroscopy of bone tissue.

In other transcutaneous Raman studies (see chapter 5 and chapter 8), a canine limb was chosen, because the bone size and thickness of overlying tissue was similar to that of human subjects. However, the ring/disk probe used in prior studies is not as effective for transcutaneous Raman spectroscopy of murine bone. Mice are commonly used for the study of various bone disorders, owing to their rapid development and the availability of a variety of mutant models. Additionally, mice and rats can be used for longitudinal studies of osseointegration implant biocompatibility, bone graft incorporation, and fracture healing.<sup>1-3</sup> Because mouse limbs are small, separating the illuminated region and collection field of view is experimentally difficult. While



practical on a larger specimen, previously described ring/disk probes are not easily focused to the dimensions required for smaller animals.

In this chapter we report the development of a fiber-optic Raman probe configuration suitable for mice. By exploring five fiber-optic probe configurations in an *in vivo* study of 32 mice we demonstrate that, with proper probe design, differences between transcutaneous Raman spectra and spectra obtained on exposed bone are not statistically significant, as measured by the carbonate-to-phosphate ratio.

## Experimental

A schematic of the Raman spectroscopy system, including the mouse positioning apparatus for *in vivo* measurements is shown in figure 7.1a. The mouse restraint components are shown in more detail in figure 7.1b. The Raman excitation source comprises a 400 mW, 785 nm external cavity diode laser (Invictus, Kaiser Optical Systems, Inc., Ann Arbor, MI) launched into a 200  $\mu\text{m}$  core NIR optical fiber (Multimode Fiber Optics, Hackettstown, NJ) for excitation. The collection fibers (fifty 100  $\mu\text{m}$  core circular bundle) and optics of a non-confocal fiber-optic probe (PhAT probe, Kaiser Optical Systems, Inc.) were employed to collect backscattered Raman shifted light and present it to the spectrograph. A NIR-optimized imaging spectrograph (Holospec, f/1.8, Kaiser Optical Systems, Inc.) fitted with a 50  $\mu\text{m}$  slit was used to provide 6-8  $\text{cm}^{-1}$  spectral resolution. The detector was a thermoelectrically cooled deep-depletion 1024x256 pixel CCD (Model DU420-BR-DD, Andor Technology, Belfast, Northern Ireland) operated at -75  $^{\circ}\text{C}$ . A 75 mm focal length converging lens was fitted at

the probe head, resulting in a 3 mm diameter circular field of view from the bundle of collection fibers. The wavelength axis of the spectrograph was calibrated against the neon discharge spectrum from a HoloLab calibration accessory (Kaiser Optical Systems, Inc.). The diffused white light from the calibration accessory was used to correct for the wavelength response of the CCD.

Five different illumination configurations were tested, as illustrated in Figure 7.2. For ring illumination, the laser light was collimated (F810FC-780, Thorlabs Inc., Newton, NJ) and directed through a 175° axicon (Del Mar Photonics, San Diego, CA). A telephoto lens pair was used to focus the ring to an inner diameter of 1.0 mm and an outer diameter of 2.5 mm. For global illumination, laser light was projected through the built-in optics of the PhAT probe and a 75 mm focal length lens. For line illumination, the laser light was collimated and passed through a 60 mm focal length cylinder lens. A telephoto lens pair was used to shape and focus a 5.0x1.0 mm laser line onto the specimen. The projected laser line could be rotated by turning the cylinder lens about its axis. For the ring and line illumination geometries a dichroic mirror (R785rdc, Chroma Technology Corp., Rockingham, VT) reflected the 785 nm light to the specimen and transmitted the Raman signal to the collection fibers. All components were mounted in lens tubes and a cube mount (SM1 series, Thorlabs, Inc., Newton, NJ).

Signal collection was achieved by using the circular array of fifty collection fibers from the PhAT probe. As a group these fibers will be referred to as the collection disk. Each illumination configuration was paired with a single collection disk. For the line illumination configurations (figure 7.2), the position of the illumination line relative to

the collection disk was achieved by angling the dichroic mirror so that the projection of the collection fibers and the projection of the illumination line were not coaxial.

For each probe configuration we took a set of *in vitro* transcutaneous measurements on a mouse tibia at the medial side of the mid-diaphysis just below the tibial tuberosity. Each probe configuration was tested on a different right or left mouse tibia obtained from an animal sacrificed in the course of unrelated studies at the University of Michigan Medical School. Fur in the site of interest was removed with a depilatory agent (extra strength hair remover lotion, Sally Hansen Corp, Uniondale, NY), and transcutaneous measurements were made. Spectra were acquired with 2-minute integration times. Laser power at the specimen varied from 150 mW to 200 mW, depending on the illumination geometry. Transcutaneous signals collected with the different probe configurations were compared for variance and bone signal intensity. The 'line/disk 1' probe configuration was selected for *in vivo* transcutaneous measurements on 32 mice because it provided the best combination of subsurface signal intensity, signal variance, and laser power distribution.

The relative size of the illumination and collection area and the probe alignment for the *in vivo* studies are illustrated in figure 7.3. The illumination line was always positioned directly over the bone, while the collection area was either offset to the posterior side (*offset left*), centered over (*probe centered*), or offset to the anterior side (*offset right*) of the tibia. A helium-neon laser was directed through the illumination optics of the collection (PhAT) probe and used to align the probe so that the 785 nm laser line was in the center of the collection disk (made visible by the helium-neon laser) when a flat object was 75 mm away from the probe head. With the tibia surface positioned at

the focal point of the collection fiber bundle field of view, the 785 nm laser line was aligned in the center of the collection disk on a planar target. As a consequence of the limb curvature, in some cases the laser light was actually positioned to one side of the field of view, resulting in the three different probe alignments shown in figure 7.3. However, the laser line was always positioned over the tibia.

All *in vivo* measurements followed protocols approved by the University of Michigan Committee on the Use and Care of Animals. The animals were 15 week old female UM-HET3 mice. The UM-HET3 stock is derived from four inbred mice strains: BALB/cJ (*C*), C57BL/6J (*B6*), C3H/HeJ (*C3*), and DBA/2J (*D2*). They are the female progeny of (*C x B6*)F<sub>1</sub> females and (*C3 x D2*) F<sub>1</sub> males. The mice were anesthetized with 5% isoflurane in a small chamber and then placed on the stage and fitted with a nose cone for continual delivery of 2% isoflurane to maintain sedation during the measurements. Fur was removed from the site of interest using the depilatory agent. Glycerol was applied for optical clearing.<sup>4</sup> Transparent 12.5 μm thick polyethylene film (Handi-Wrap, DowBrands, Indianapolis, IN) was placed over the limb at the site of interest, and room temperature water was dripped onto the film for the duration of the measurement to prevent thermal damage. After the line/disk probe was aligned on the tibia, ten 60 second transcutaneous acquisitions were acquired. The animal was then sacrificed, the tibia was excised, and direct measurements were taken on the exposed bone in the region of interest.

## **Data Treatment**

All spectral processing was performed in MATLAB 6.1 (The Mathworks, Inc., Natick, MA). Each acquisition consisted of an array of 256 spectral rows as a single CCD image. Preprocessing included removing spikes due to cosmic rays, subtracting the dark current, correcting for pixel-pixel and wavelength response variation on the CCD, and correcting for slit image curvature caused by the large gathering angle of the spectrograph. The spectra from each fiber typically covered five pixel rows on the CCD. Only the central three spectra from each fiber were used to avoid cross-talk from adjacent fibers. For each acquisition these central three spectra were summed prior to further data reduction, yielding a data set of fifty spectra per acquisition (one spectrum per fiber). The transcutaneous spectral data were truncated to the 775-1500  $\text{cm}^{-1}$  region of interest and then baselined using a weighted least squares iterative baselining procedure with a seventh-order polynomial.<sup>5,6</sup>

The *in vitro* transcutaneous measurements for each probe configuration were compared for bone signal intensity and fiber-to-fiber spectral variance. To compare bone signal intensity, the fifty spectra from all measurements for a given probe configuration were averaged and then normalized to the 1050-1090  $\text{cm}^{-1}$  spectral range. The averaged intensity of the phosphate  $\nu_1$  band was compared between probe configurations. The fiber-to-fiber spectral variance was determined by standardizing (mean centering and division by the standard deviation) the fifty spectra for each probe configuration and comparing the fiber-to-fiber signal variance in the phosphate  $\nu_1$  signal intensity across the standardized spectra. Additionally, the laser power distribution for each probe configuration was considered by calculating the area of illumination.

The data from the *in vivo* transcutaneous measurements were combined so that the ten 60-second measurements were paired to form five data sets of 100 spectra each. The delivered radiation dose and collection time for each mouse was equivalent to five 2 minute transcutaneous measurements. Band target entropy minimization was used to recover the bone factors<sup>7-10</sup>. The region of the transcutaneous spectra targeted was the bone mineral phosphate  $\nu_1$  band, which is intense and is absent from the spectra of overlying tissue. The eigenvector weight distribution test was used for selecting the appropriate number of eigenvectors for each transcutaneous measurement.<sup>9</sup> The recovery algorithm was run five times on each 2 minute acquisition, and the average of these five results was taken to be the recovered bone factor. The number of eigenvectors used ranged between 3 and 40.

The cross-correlation coefficient between the average recovered bone factor and the averaged exposed bone spectrum for each 2 minute measurement was calculated from the standardized spectra using MATLAB. The recovered bone factors and exposed bone measurements were imported into GRAMS/AI (Thermo Galactic, Madison, WI) with RazorTools/8 (Spectrum Square Associates, Ithaca, NY) and fit for peak heights using mixed Gaussian and Lorentzian polynomials and standard peak width constraints. The carbonate-to-phosphate band height ratio ( $1070\text{ cm}^{-1}/959\text{ cm}^{-1}$ ) was used for comparison of recovered transcutaneous bone spectra and exposed bone spectra.

All statistical calculations were performed using SAS 9 (SAS Institute, Inc., Cary, NC). A significance level of 0.05 was used for all analyses.

The accuracy of the transcutaneous measurements was assessed by comparing the recovered bone factors to the exposed bone spectra using both the mean and standard

deviation of the carbonate-to-phosphate band height ratios. For *in vivo* transcutaneous bone data, the mean and standard deviation of the ratio was computed for each mouse over all 25 measurements (the recovered bone factor was calculated 5 times for each of the five 2 minute measurements). For exposed bone data, the mean and standard deviation of the ratio was computed over all 19-30 measurements. The number of exposed bone measurements was based on the number of collection fibers that could be focused onto the tibia, a number that was variable because the size of the mouse tibia varied. The mean transcutaneous and exposed measurements were compared using a paired t-test. Because the difference in standard deviation measurements was not normally distributed, a nonparametric Wilcoxon signed-rank test was used to compare those data.

The precision of the transcutaneous measurements was examined with repeated measures analysis of variance (RM ANOVA) using a mixed-effect model. The carbonate-to-phosphate ratios from the recovered bone factors were treated as the repeated measure within mice, with five levels (one for each 2 minute acquisition). Two RM ANOVAs were analyzed, one for the mean ratio and one for the standard deviation of the mean ratio. The optimum within-subjects covariance structure was determined using both the Akaike and the Bayesian Information Criteria.<sup>11</sup> A heterogeneous autoregressive model fit best for analysis on the mean, and an autoregressive model fit best for analysis on the standard deviation.

The cross-correlation coefficients were grouped by color of the animal's fur to analyze the effect of animal coat color. The 32 mice were divided equally into four groups (brown agouti, brown, black, and agouti), and the average value of the five

measurements was used for analysis. Three one-way ANOVAs were analyzed using a fixed-effect model: one for the mean value of correlation coefficients, one for the standard deviation of correlation coefficients, and one for the coefficient of variation of correlation coefficients.

In order to evaluate probe alignment, the spectral data were grouped according to probe alignment (figure 7.3), and each group was matched for coat color. Because the three probe alignments were a result of unintentional probe misalignments, the majority of alignments were offset right. To ensure an equal number of mice in each group and an even distribution of coat color we were restricted to four mice per group: two brown, one brown agouti, and one black. The transcutaneous signal collected by each fiber was averaged over all five repetitions to improve the signal-to-noise ratio. The phosphate  $\nu_1$ /phenylalanine ring breathing band height ratio, a measure that has previously been used as a metric of bone signal relative to the signal of overlying tissue,<sup>12</sup> was calculated for each collection fiber. The average ratio over the 50 fibers for each of the 4 mice was analyzed using a one-way ANOVA on means and a one-way ANOVA on standard deviation. Additionally, a RM ANOVA was used with ratios from the 50 fibers as the repeated measure. The probe alignment, coat color, and their interaction were modeled in the RM ANOVA using a mixed-effect model with a compound symmetry covariance structure. Pair-wise comparisons of the probe alignment configurations were examined using orthogonal contrasts.

## **Results and Discussion**



Three factors were assessed to determine an optimal probe configuration. An ideal probe configuration would maximize the bone signal relative to the background, maximize the fiber-to-fiber variation in the collected signal, and maximize the distribution of laser power to prevent thermal damage to the tissue. The results from the different probe configurations are illustrated in figure 7.4. The bone signal, indicated by the phosphate  $\nu_1$  band, was much higher for the ring/disk and ‘line/disk 1’ probe configurations (figure 7.4a). For these two configurations, the majority of the laser light was focused directly on bone tissue beneath the overlying tissue. For the global, ‘line/disk 2’, and ‘line/disk 3’ configurations, the illuminated region included a greater area outside of the bone, which led to a greater contribution from other tissues and a decreased contribution from the bone tissue.

The 1050-1090  $\text{cm}^{-1}$  range was chosen for normalization of transcutaneous spectra because it contains signal originating from the overlying tissue. With this normalization, visual inspection provides an estimate of the relative contribution of overlying tissue and bone contributions to the observed spectrum. The phosphate  $\nu_1$  band region (ca. 950-970  $\text{cm}^{-1}$ ), which has been widely employed for normalization of bone Raman spectra, was not used in these measures, because the signal originates entirely from the subsurface bone.

The fiber-to-fiber spectral variation in the signal was smallest for the global probe (figure 7.4b), because it does not provide the range of offsets of the line illumination geometries.<sup>13</sup> As we have previously shown, the depth penetration with the global probe is not as great as with probe configurations that completely offset the excitation points and collection field of view. The ‘line/disk 2’ and ‘line/disk 3’ configurations showed

greater variation in the signal than the other illumination schemes. The ring/disk and 'line/disk 1' configurations provided a partial separation of excitation and collection fibers regions, and the variance of these two configurations fell between that of the other probe configurations.

The laser power distribution was greatest with the global illumination approach; however, the configuration lacked variation in the fiber-to-fiber signal and signal intensity from the underlying bone. The ring/disk configuration had the most intense subsurface bone signal, but it illuminated the smallest area. The line illumination has been shown to dissipate heat more efficiently than a spot or point illumination.<sup>14</sup> As a result, the 'line/disk 1' probe configuration had the best trade-offs between laser power distribution, subsurface bone signal intensity, and fiber-to-fiber signal variation. Therefore, the 'line/disk 1' probe was chosen for the *in vivo* studies.

A typical recovered bone spectrum is shown in figure 7.5a and 7.5b. The spectra are from specimen number 19 (figure 7.5c). Figure 7.5a shows the fiber-fiber variation in the exposed bone spectra, while figure 7.5b shows the averaged exposed bone spectrum. The average transcutaneous measurement is illustrated by a dotted line, and the exposed bone spectra are shown in black. The fiber-to-fiber variance in the exposed bone spectra (figure 7.5a) is large, because the fiber probe sampled different points along the tibia. Because of the diffusive nature of light transport in transcutaneous measurements, determination of the exact location on the tibia from which the recovered bone factor originated is not possible. Therefore, the average exposed bone spectrum is similar to, but not identical to, the recovered bone factor (figure 7.5b). The average recovered bone factors were highly correlated with the average exposed bone spectra, as seen by the high

cross-correlation coefficient for each of the specimens (figure 7.5c). The average cross-correlation over all of the measurements was 0.96. However, some specimens had higher cross-correlations and smaller standard deviations in the repeated measures than did others.

In addition to cross-correlation, the carbonate-to-phosphate band height ratio (figure 7.6) was used as a measure of recovered bone accuracy and precision. The average carbonate-to-phosphate ratio for the exposed bone spectrum and recovered bone factor is shown in figure 7.6a. The results for each mouse are shown in figure 7.6b. Over all mice, the mean carbonate-to-phosphate ratios computed for the transcutaneous bone data did not differ significantly from those computed for the exposed bone data ( $p=0.12$ ). However, the standard deviation of the ratios was significantly smaller for transcutaneous measurements than for exposed measurements ( $p < 0.0001$ ). For the transcutaneous data, neither the mean nor the standard deviation of the carbonate-to-phosphate ratios varied significantly across the five acquisitions ( $p = 0.45$  and  $p = 0.25$ , respectively). Therefore, the noninvasive Raman spectroscopic measurements of bone tissue in the mouse tibia were both precise and accurate, as compared to measurements on the exposed bone tissue.

Both animal coat color and probe alignment may have an effect on the recovered bone spectra. The cross-correlation results are grouped by coat color in figure 7.7. Coat color was not a significant predictor of either the mean ( $p=0.22$ ) or standard deviation ( $p=0.069$ ) of the correlation coefficients (figure 7.7a). However, the number of specimens was small for these analyses, which limited our ability to detect differences among the coat colors. For the mice with brown fur, the mean of the coefficients tended

to be slightly higher and the standard deviation of the coefficients tended to be lower than for mice with other coat colors (figure 7.7a). In addition, the measurement-to-measurement variability tended to be lower for the mice with brown fur (figure 7.7b). Taken together, these results indicate that the exposed and recovered bone spectra had more consistent agreement in the mice with brown fur. Measurements of larger number of specimens would be necessary to find statistical significance (or its lack) in this trend at a 95% confidence level.

The effect of the different probe alignments on the recovered signal is shown in figure 7.8. Because coat color had some effect on signal variability, mice were grouped based on probe alignment and coat color, with four mice per group. The phosphate  $\nu_1$  band at  $959\text{ cm}^{-1}$  was used as a measure of bone signal intensity and was compared to the height of the phenylalanine band ca.  $1003\text{ cm}^{-1}$ , which is found in both overlying tissue and bone. This ratio was computed for the signal collected by each fiber for the three different probe alignments. The larger the ratio, the greater the collected bone signal. When the mean ratio of the 50 fibers was examined for each of the 4 mice and three probe alignments, neither the mean ( $p=0.37$ ) nor the standard deviation ( $p=0.11$ ) of the phosphate-to-phenylalanine ratio differed significantly across the three probe alignments.

However, when the ratio for each of the fibers was treated as a repeated measure, probe alignment had a significant effect on these measurements ( $p<0.0001$ ). Even after accounting for the effect of coat color, the three alignments were significantly different from each other (center vs. left  $p<0.0001$ , center vs. right  $p<0.0001$ , and left vs. right  $p=0.0027$ ). Although some of the fibers collected signal from over the bone in all three alignments, the remaining fibers collected signal from other sources that varied

depending on alignment. Therefore, the collected signal should differ across the different probe alignments. In the offset left position the remaining collection fibers collected signal from the soft tissue in the posteromedial portion of the limb and from the aluminum of the mouse restraint. In the centered position, the remaining collection fibers collected signal from soft tissue in the anteromedial and posteromedial portions of the limb. In the offset right position, the remaining fibers collected signal from the anteromedial side of the left leg and from the aluminum of the mouse bed.

The mean and standard deviation of the absolute relative difference in the carbonate-to-phosphate ratio between the exposed bone and the recovered bone factor for each of the specimens grouped by probe alignment is shown in figure 7.9a. The average value over all specimens for each probe alignment is indicated by a black dashed line. The mean difference was lower for the offset right alignment than for the other two probe alignments. The coefficient of variation between the three probe alignments, as shown in figure 7.9b, was slightly lower for the offset right probe, indicating a lower variability between carbonate-to-phosphate ratio measurements for this probe alignment.

## **Conclusions**

The results obtained using the line/disk probe demonstrates that this configuration is suitable for precise and accurate transcutaneous Raman spectroscopy of murine bone tissue *in vivo*. This configuration distributes the laser power to prevent thermal damage and provides a spatial separation between the illuminated region and some of the collection fibers. Both probe alignment and animal coat color were found to have an

impact on the transcutaneous Raman signal. These data suggest that transcutaneous studies of bone would benefit by choosing a mouse with a brown coat color and by aligning the probe so that the collection fibers are to the anteromedial side of the tibia or, more generally, over as little soft tissue as possible.

Though the laser fluence was above ANSI Z163.1 threshold limit values (TLV)<sup>15</sup> for human skin exposure, no burning was observed in any of the *in vivo* measurements. The ANSI TLVs are designed to insure that no thermal damage will occur in even the most heavily pigmented skin. Our results do not allow us to assess the role, if any, of active water cooling in the prevention of thermal damage.

In this study, validation of the recovered bone factor was limited to evaluating the averaged exposed bone spectra over the general region of collection. Though this approach is reasonable, we would prefer to have more accurate knowledge of the exact origin of the observed Raman spectra. *A priori* knowledge of the bone architecture measured independently by micro-computed tomography or magnetic resonance imaging, would allow Raman tomographic reconstruction,<sup>16, 17</sup> which would provide a more accurate definition of the regions of exposed bone for validation of our transcutaneous measurements.

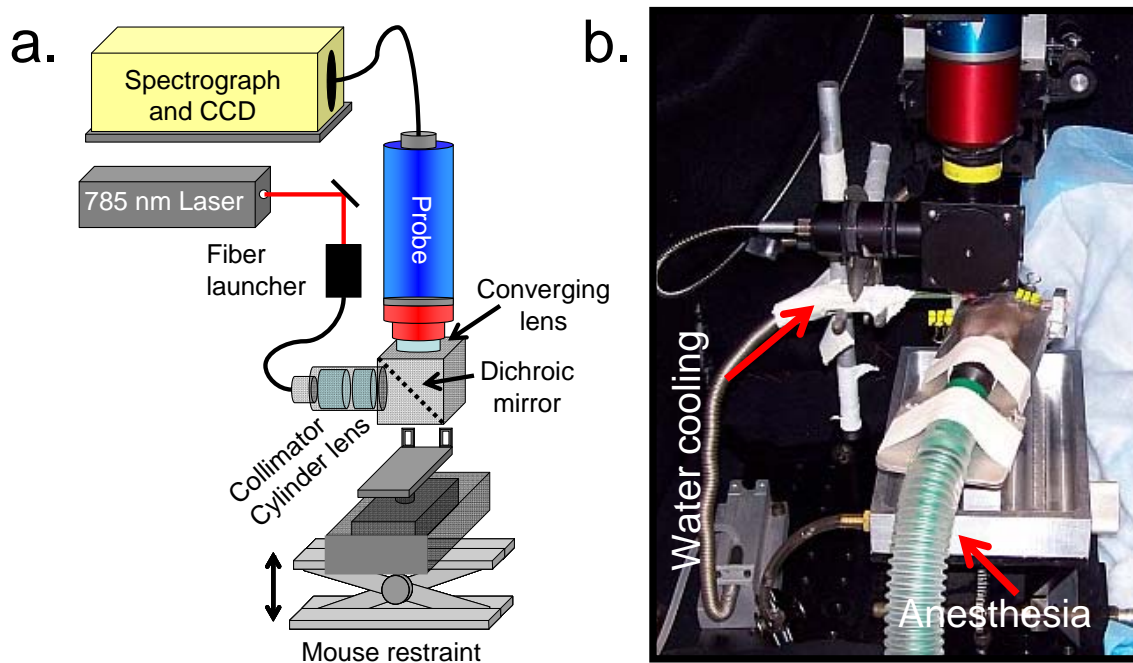


Figure 7.1: (a) Schematic of Raman spectroscopy system for *in vivo* measurements on mice. (b) Photograph of mouse restraint, showing water cooling and anesthesia delivery subsystems.

## Illumination/Collection Configurations

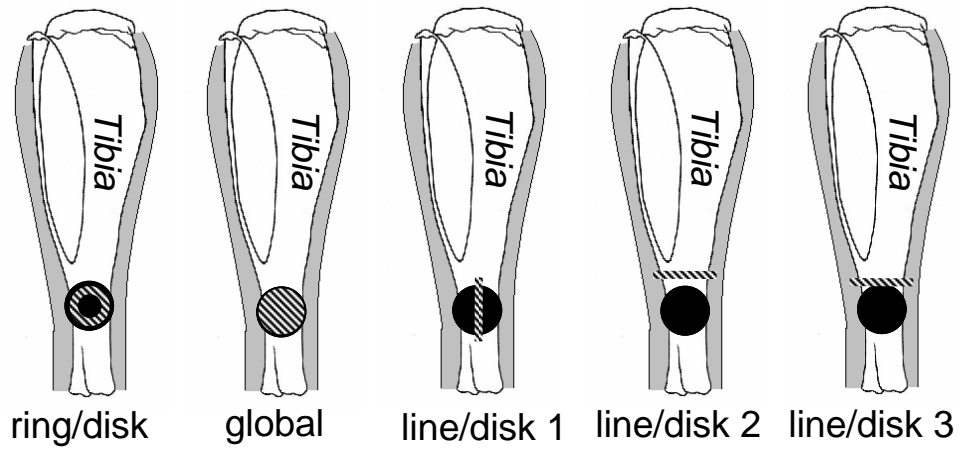


Figure 7.2: Schematic of a mouse tibia with five different illumination (striped) and collection (solid) optical configurations.



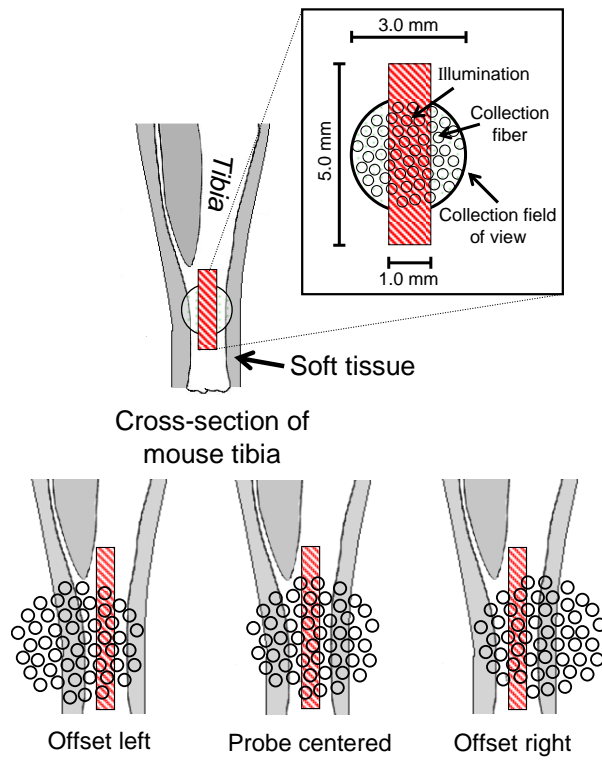


Figure 7.3: Schematic of probe alignment on a left mouse tibia

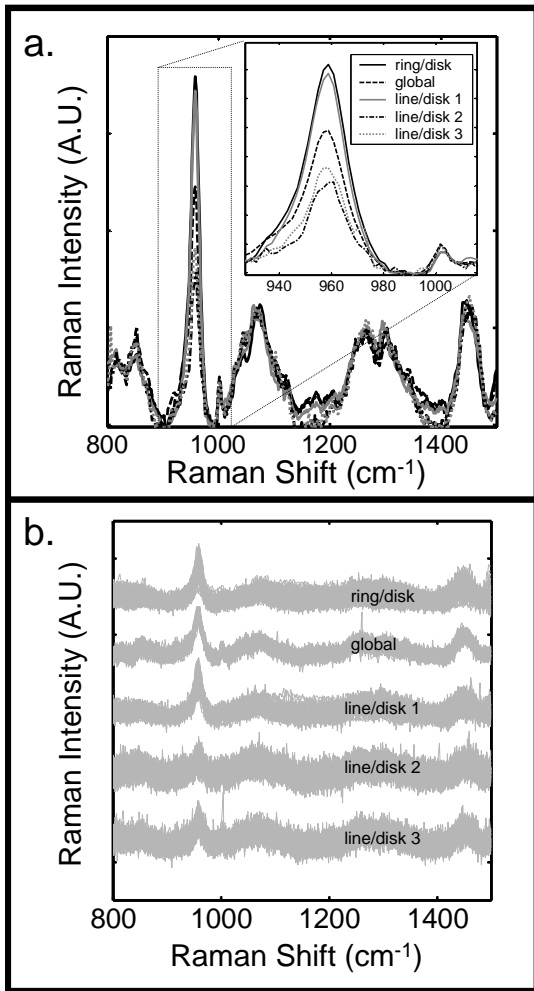


Figure 7.4: (a) Average transcutaneous signal for the five different Raman probe configurations of Fig. 7.2. (b) Superimposed standardized spectra from each of the fifty collection fibers for each probe configuration.

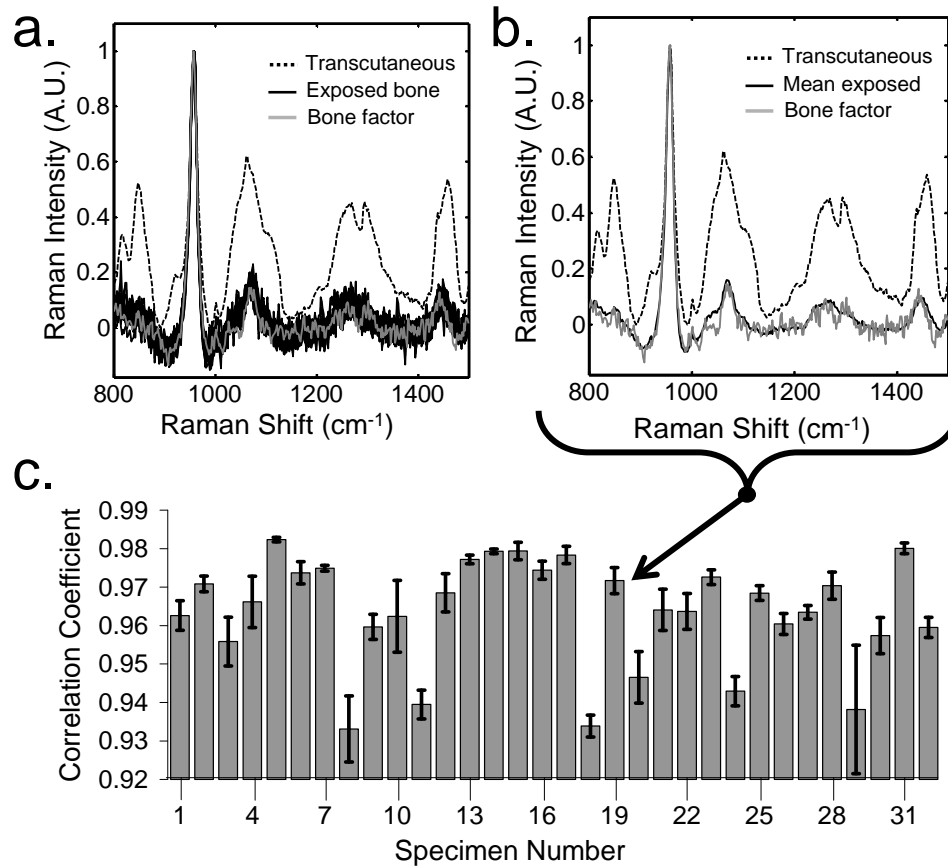


Figure 7.5: Representative recovered bone factor for the *in vivo* transcutaneous measurements (a) compared to the individual exposed bone spectra and (b) the average exposed bone spectrum of specimen 19. (c) The correlation coefficient results for all specimens.

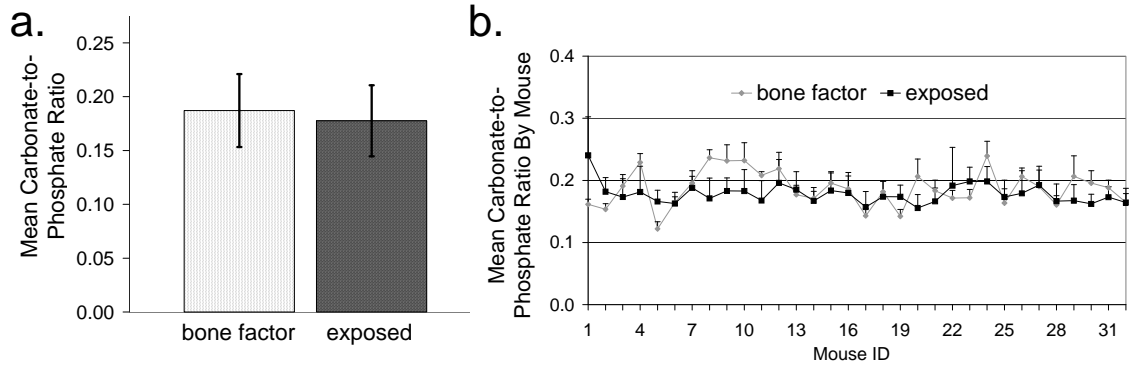


Figure 7.6: (a) Average carbonate-to-phosphate ratio for all mice. (b) Average carbonate-to-phosphate ratio by mouse showing the standard deviation of the exposed bone measurements and of the recovered bone factors.

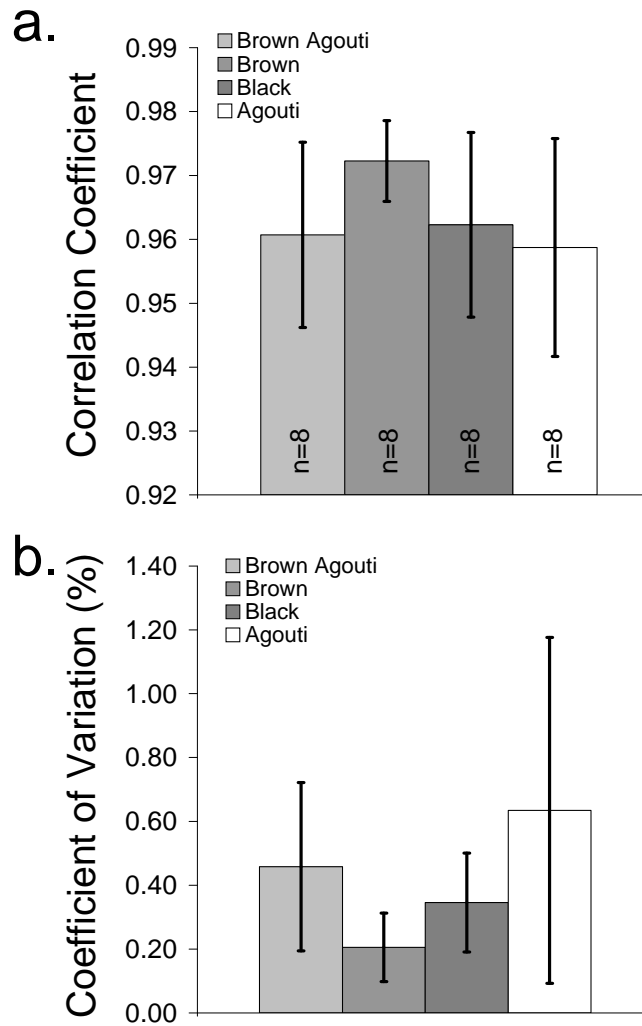


Figure 7.7: (a) Correlation coefficient and (b) coefficient of variation over the correlation coefficients, grouped by coat color.

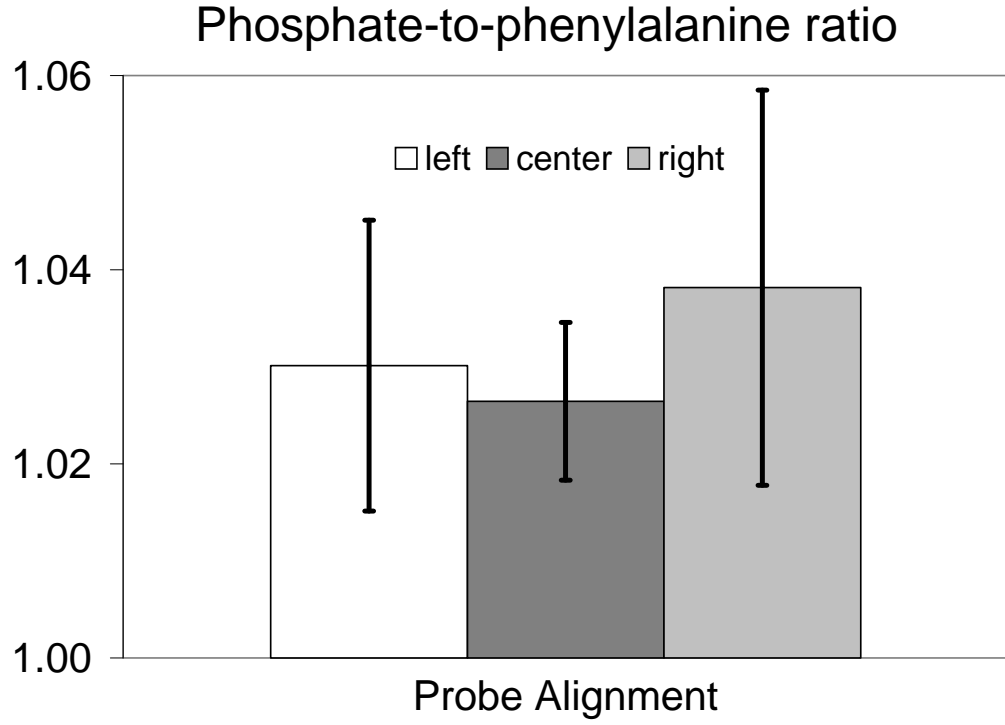


Figure 7.8: Average phosphate-to-phenylalanine height ratio taken from the transcutaneous signal collected by each fiber for each of the probe alignments

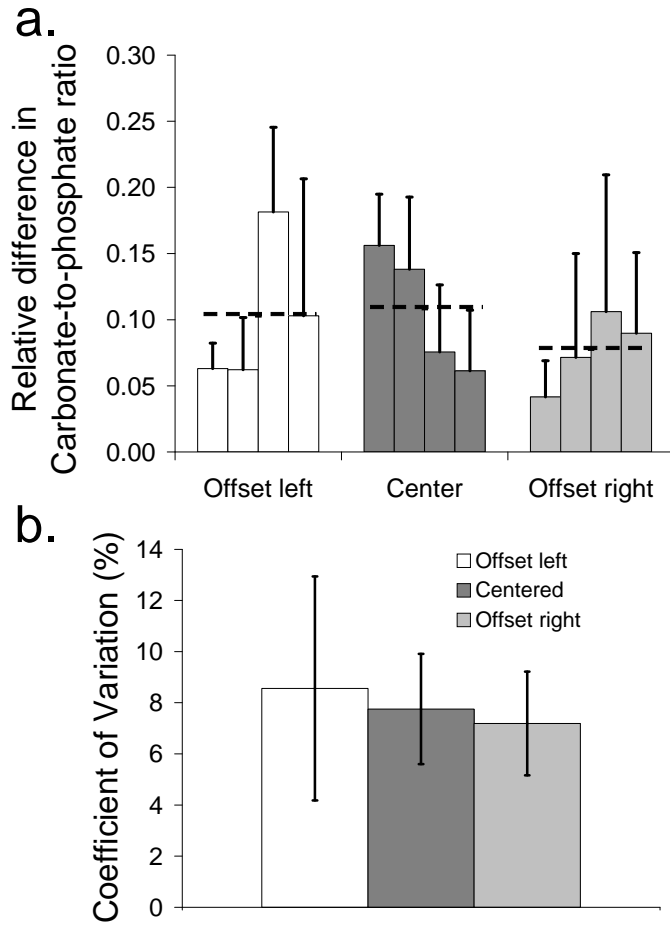


Figure 7.9: (a) Difference in the carbonate-to-phosphate ratio between the recovered bone factor and the exposed bone spectrum for each specimen and average difference over all four mice (dashed line) for each probe alignment (b) Coefficient of variation between the carbonate-to-phosphate ratios for each of the probe alignments.

## References

1. T. Masuda, G. Salvi, S. Offenbacher, D. Felton and L. Cooper, "Cell and matrix reactions at titanium implants in surgically prepared rat tibiae," *Int J Oral Maxillofac Implants* 12, 472-485 (1997)
2. C. Tsai, M. Chou, M. Jonas, Y. Tien and E. Chi, "A composite graft material containing bone particles and collagen in osteoinduction in mouse," *J Biomed Mater Res* 63, 65-70 (2002)
3. J. Lane, A. Boskey, W. Li, B. Eaton and A. Posner, "A temporal study of collagen, proteoglycan, lipid and mineral constituents in a model of endochondral osseous repair," *Metab Bone Dis Relat Res* 1, 319-324 (1979)
4. M. V. Schulmerich, J. H. Cole, K. A. Dooley, J. M. Kreider, S. A. Goldstein and M. D. Morris, "Optical clearing in transcutaneous Raman spectroscopy of murine cortical bone tissue," *J. Biomed. Optics* 13(2), 021108 (2008)
5. C. A. Lieber and A. Mahadevan-Jansen, "Automated method for subtraction of fluorescence from biological Raman spectra," *Appl. Spectrosc.* 57(11), 1363-1367 (2003)
6. J. Zhao, H. Lui, D. I. McLean and H. Zeng, "Automated Autofluorescence Background Subtraction Algorithm for Biomedical Raman Spectroscopy," *Applied Spectroscopy* 61, 1225-1232 (2007)
7. E. Widjaja, C. Li, W. Chew and M. Garland, "Band-target entropy minimization. A robust algorithm for pure component spectral recovery. application to complex randomized mixtures of six components," *Anal. Chem.* 75(17), 4499-4507 (2003)
8. L. R. Ong, E. Widjaja, R. Stanforth and M. Garland, "Fourier transform Raman spectral reconstruction of inorganic lead mixtures using a novel band-target entropy minimization (BTEM) method," *J Raman Spectrosc.* 34, 282-289 (2003)
9. E. Widjaja, N. Crane, T. Chen, M. D. Morris, M. A. Ignelzi Jr. and B. McCreadie, "Band-Target Entropy Minimization (BTEM) Applied to Hyperspectral Raman Image Data," *Appl Spectrosc.* 57(11), 1353-1362 (2003)
10. C. Wee, E. Widjaja and M. Garland, "Band-target entropy minimization (BTEM): an advanced method for recovering unknown pure component spectra. Application to the



FTIR spectra of unstable organometallic mixtures.," *Organometallics* 21, 1982-1990 (2002)

11. J. Neter, M. Kutner, C. Nachtsheim and W. Wasserman, *Applied Linear Statistical Models*, WCB/McGraw-Hill, Boston (1996).

12. M. V. Schulmerich, K. A. Dooley, T. M. Vanasse, S. A. Goldstein and M. D. Morris, "Subsurface and Transcutaneous Raman Spectroscopy and Mapping Using Concentric Illumination Rings and Collection with a Circular Fiber-Optic Array," *Applied Spectroscopy* 61, 671-678 (2007)

13. M. V. Schulmerich, M. D. Morris, T. M. Vanasse and S. A. Goldstein, "Transcutaneous Raman spectroscopy of bone global sampling and ring/disk fiber optic probes," in *Advanced Biomedical and Clinical Diagnostic Systems V*, pp. 643009-643008, SPIE, San Jose, CA, USA (2007).

14. D. Zhang, J. D. Hanna, Y. Jiang and D. Ben-Amotz, "Influence of laser illumination geometry on the power distribution advantage," *Appl. Spectrosc.* 55(1), 61-65 (2001)

15. "Z136.1" in *Safe use of Lasers* American National Standards Institute, Ed., Orlando Florida (2007).

16. M. V. Schulmerich, S. Srinivasan, J. Kreider, J. H. Cole, K. A. Dooley, S. A. Goldstein, B. W. Pogue and M. D. Morris, "Raman tomography of tissue phantoms and bone tissue," in *Biomedical Optical Spectroscopy*, pp. 68530V-68537, SPIE, San Jose, CA, USA (2008).

17. M. V. Schulmerich, S. Srinivasan, J. H. Cole, J. Kreider, K. A. Dooley, S. A. Goldstein, B. W. Pogue and M. D. Morris, "Non-invasive Raman tomographic imaging of canine cortical bone tissue," *J. Biomed. Optics* 13, 020506 (2008)

## **CHAPTER VIII**

### **RAMAN TOMOGRAPHY IN TISSUE PHANTOMS AND CANINE TISSUE**

#### **Introduction**

Diffuse Optical Tomographic (DOT) imaging of tissue has been under investigation for almost two decades<sup>1-3</sup> and is emerging as a viable method of analysis in breast cancer diagnosis,<sup>4, 5</sup> neonatal and adult cerebral monitoring,<sup>6, 7</sup> and in the imaging of small animals.<sup>8, 9</sup> In more recent years, the ability to do diffuse fluorescence tomography *in vivo* has shown great progress.<sup>10-12</sup> Diffuse fluorescence tomography uses model-based algorithms to calculate the propagation of photons through light scattering systems and by computationally matching the calculated signal to the measured signal reconstructs the size, shape, and position of targets buried in the optically turbid media.<sup>10, 13-16</sup> However, fluorescence tomography requires the presence of a fluorophore in the analyte and therefore limits the technique's usefulness in many biological sites of interest. For some applications this problem has been overcome with the use of site-targeting fluorescent labels.<sup>9</sup> Still, fluorescent labels cause an otherwise non-invasive technique to become minimally invasive. Label-free chemical imaging is possible by using Raman spectroscopy. A Raman spectrum has much higher information content and better composition specificity than a fluorescence spectrum. Additionally,

because of the high specificity, multivariate data analysis is well-suited to separate out spectral components originating from different tissue types. For example, bone has a very different Raman spectrum than the overlying tissue.<sup>17</sup> This approach generates a great deal of information in a single set of measurements.

Recent advances in DOT algorithms are useful in the development of Raman tomography. In both Raman and fluorescence, light scattering is dominant over absorption and the signal is generated only after the source light interacts with a given target. Other than molecular origin, the only major difference in how the signal propagates through the light scattering material is the signal intensity. The Raman scatter has a quantum yield several orders of magnitude lower than most fluorophores. Despite this weakness, if enough Raman scattered light is collected then the diffusion based algorithms developed for fluorescence imaging in tissue can be applied to do Raman tomography. Here, we explore the feasibility of using algorithms developed for diffuse fluorescence tomography with a Raman signal obtained from a tissue phantom and an intact excised canine hind limb with the tibia as the target site.

Bone is an especially promising tissue for Raman tomography. Molecular imaging modalities are increasingly important to basic research in bone biology and orthopaedics<sup>18</sup> as well as to clinical practice. The correlation of spectroscopically-measured bone composition change with presence of genetic defects<sup>19</sup> aging<sup>20</sup> and susceptibility to osteoporotic fracture<sup>21</sup> and the demonstration of non-invasive measurement of Raman spectra at depths of 5 mm below the skin<sup>22</sup> suggest a role for diagnostic measurements based on non-invasive Raman spectroscopy.

In this study, a diffusion model for optical tomography was used, along with Raman scattering data, to recover values from tissue phantoms and bone tissue ex vivo. Here we applied the ring/disk probe with multiple illumination rings in a backscattered geometry to demonstrate the feasibility of diffuse Raman tomography in a tissue phantom. We also applied this technology to an excised canine limb and reconstructed the position of the bone. We found the backscatter geometry caused the recovered bone signal to be surface-weighted. We then used a transmission-based setup which did a better job in reconstructing the position of the bone. Finally, because diffuse optical spectroscopic measurements can be used to overlay molecular information onto imaging systems, and a transmission geometry is known to limit the accuracy of imaging,<sup>23-25</sup> we explored the possibility of use of spatial priors in the reconstruction algorithm. Preliminary studies on Raman tomographic imaging using a transmission geometry allowed three-dimensional visualization of spatial changes in biochemical composition,<sup>26</sup> however, the localization of the origin of Raman signal was limited by the diffuse nature of light propagation. Here we also present the use of high-resolution CT images to guide the diffuse modeling of light in order to achieve a high-contrast molecular and structural characterization of tissue with accurate localization of signal origins.

## **Materials and Methods**

### **Raman probes, materials and experimental method**

The Raman system employed for backscattered collection was the ring/disk illumination/collection probe (figure 8.1a) which is described in greater detail in chapter

5 and elsewhere.<sup>22, 27, 28</sup> A transmission based Raman probe (figure 8.1b) was used for Raman tomography measurements on an intact excised canine tibia. Briefly, both system were comprised of a 400 mW 785 nm external cavity diode laser (Invictus, Kaiser Optical Systems, Ann Arbor, MI), a NIR-optimized imaging spectrograph (HoloSpec, f/1.8i, Kaiser Optical Systems) fitted with a 50  $\mu\text{m}$  slit to provide 6-8  $\text{cm}^{-1}$  resolution. The detector was a thermoelectrically cooled deep-depletion 1024x256 pixel CCD (Model DU420-BR-DD, Andor Technology, Belfast, Northern Ireland) operated at  $-75^{\circ}\text{C}$  with no binning. The dispersion axis of the spectrograph was calibrated against the neon discharge lamp of a Raman Calibration Accessory (Kaiser Optical Systems). The diffused quartz-halogen light of the Calibration Accessory was used to flat-field the CCD.

Backscatter Raman measurements were acquired from both the tissue phantom and the canine limb. For these measurements, the sampling system was a filtered fiber optic probe with a bundle of fifty 100  $\mu\text{m}$  core collection fibers arranged in a close-packed circle (PhAT probe, Kaiser Optical Systems, Ann Arbor, MI). At the spectrograph end, the collection fibers were arranged in a linear array for coupling into the spectrograph. For the tissue phantom measurements, the collection probe was fitted with a 500 mm focal length fused silica lens that focused to a 14 mm diameter collection field of view. For the canine measurements a 250 mm focal length fused silica lens was used to provide a collection field of view that was 7 mm in diameter. The laser power available at the sample/specimen was attenuated to 200 mW. To generate an annulus for ring/disk illumination the laser light was launched into a 200 $\mu\text{m}$  NIR optical fiber (Multimode Fiber Optics Inc., Hackettstown, NJ). The light was collimated (F810FC-780, Thorlabs Inc., Newton, NJ) and directed through a  $175^{\circ}$  axicon (Delmar Ventures,

San Diego, CA). Telephoto optics (positive/negative lens pair with variable spacing) were placed after the axicon and used to vary the annulus diameter. A dichroic mirror (Chroma Technology Corp., Rockingham, VT) reflected the 785nm light to the sample and transmitted the Raman signal for collection.

Transmission Raman measurements were acquired for the excised canine limb. For these measurements the sampling system was a rectangular fiber optic array of 100  $\mu\text{m}$  fibers arranged in a 5 x 10 closed-packed rectangle (FiberTech Optica Inc., Kitchener, ON, Canada). At the other end of the bundle, these collection fibers were arranged in a line for coupling into the spectrograph. An 800 nm band-pass filter and 250 mm fused silica lens was placed in front of the rectangular bundle to reject ambient and Rayleigh scattered light and to focus the fibers to a 9 x 5 mm collection field of view at the specimen. For illumination, laser light was launched into a 200 $\mu\text{m}$  NIR optical fiber (Multimode Fiber Optics Inc., Hackettstown, NJ). The light was collimated (F810FC-780, Thorlabs Inc., Newton, NJ) and directed through a 50mm focal length cylinder lens that was positioned between a telescope comprised of two 50 mm singlet fused silica lenses. The optical elements were translated to project an 8 x 1.5 mm illumination line onto the specimen. Power at the specimen was attenuated to 200 mW.

### **Tissue phantom**

An agar/Intralipid® tissue phantom with a 3/8" (~9 mm) Teflon® sphere embedded 10 mm below the surface was used as a model system to demonstrate the feasibility of Raman tomography. The tissue phantom was prepared by combining

2.67 g of agar (No A-7049, Sigma-Aldrich) with 133 ml of distilled water and 0.043 g of Sodium azide (No S-2002, Sigma-Aldrich) and heating to 90 °C for fifteen minutes until the solution appeared optically clear. The liquid was left at room temperature to cool to ~ 45 °C and was then combined with 6.5 ml of 20% Intralipid® while stirring to produce a 1% agar/Intralipid® phantom. This solution was then poured into a mold which held the Teflon® sphere in place with pins so that the top of the sphere was position 10mm below the surface of the liquid. The placement of the pins was such that they would not interfere with measurements. The mold was placed in a vacuum chamber for 10 minutes to remove air bubbles and then was refrigerated overnight inside an air tight container. The next day pins were removed and the phantom was released from the mold for measurements. Nine acquisitions were taken using the ring/disk probe with the illuminations rings incremented from 4.0 to 13.5 mm in diameter (table 8.1). These diameters were chosen so that the illuminated region overlapped the field of view of the collection fibers. The acquisition time for each measurement was 10 seconds.

### **Canine limb**

The second model system was an intact excised canine tibia obtained from a discarded tissue repository. The limb was harvested from an animal euthanized in approved (University Committee on Use and Care of Animals) studies at the University of Michigan Medical School. In excising the limb, care was taken to preserve all the soft tissues surrounding the tibia. The limb was scanned using an in-vivo micro-computed tomography (micro-CT) scanner (eXplore Locus RS, GE Healthcare, Ontario, Canada).

Measurements were taken at an operating voltage of 80kV and 450 $\mu$ A of current, with an exposure time of 100 ms using a 360 degree scan technique. The high dynamic range adjustment was selected so that pins being used to hold the skin intact would not cause problems with the image reconstruction. The effective voxel size of the reconstructed image was 93 x 93 x 93  $\mu\text{m}^3$ . The micro-CT reconstruction was used to create a finite element mesh for the Raman tomographic reconstruction. Prior to Raman measurement all hair was removed over the region of interest using a depilatory agent (Sally Hansen Corp, Uniondale, NY) and glycerol was then applied for optical clearing.<sup>29</sup> The collection disk was focused at the medial side of the right tibia at the diaphysis. The dimensions of the ten illumination rings used for transcutaneous measurements were between 6 and 16 mm (table 1). Each acquisition was 1 minute. After all transcutaneous measurements were taken the overlying tissue was removed with a scalpel and an exposed bone measurements was taken for validation. Additional Raman measurements were taken of the tibia using a transmission geometry. The tibia was clamped onto a 360 $^\circ$  rotation stage and 13 five minute projections were obtained at 8 $^\circ$  intervals. Line illumination was incident on the anterior side of the tibia with the light focused onto the skin and the collection fibers were focused onto the skin of the limb's posterior side.

### **Spectral data reduction methodology**

All spectral data was imported into MATLAB 6.1 (The Mathworks Inc., Natick, MA). Preprocessing included dark current subtraction and correction for the variation in the pixel-to-pixel and wavelength response of the spectrograph. The spectral dimension



was shifted from pixels to wavenumbers using a calibration against a neon source. For the tissue phantom measurements, it was necessary to obtain a single number that represented the Teflon® signal detected by each fiber. This was accomplished by taking the ratio of the 732  $\text{cm}^{-1}$  Teflon band and a band from the Intralipid® at 842  $\text{cm}^{-1}$ . A schematic of the tissue phantom and the average Raman spectra from one tissue phantom acquisition is shown in figure 8.2. The entire dataset (450 fibers) was then normalized and the number for each fiber representing the Teflon® signal was input into the reconstruction algorithm.

For the canine tibia measurements, a Blackman-Harris windowing function was applied to each spectrum to remove high frequency components.<sup>30</sup> In the experimental set-up, a single fiber from the fifty-fiber-probe projected a Raman spectrum onto the CCD over an area that covered approximately five pixel rows. To avoid cross-talk, only the central three pixel rows were used. These three spectra were averaged to improve signal-to-noise. The remaining background, resulting from auto-fluorescence, was removed using an iterative background subtraction procedure with a 5th order polynomial.<sup>31</sup> The 833-1500  $\text{cm}^{-1}$  region was chosen as the region of interest (ROI), because it includes Raman bands that are correlated with the mechanical properties of bone.<sup>21, 32, 33</sup> The spectra were normalized to the phosphate  $\nu_1$  band.

In order to reconstruct 3-D Raman tomographic images of bone, the Raman spectral signal (bone factor) coming from the bone must be determined. The methodology for recovering a bone factor is described in chapter 5 and an earlier publication.<sup>22</sup> Briefly, three of the ten ring/disk spacings were chosen as optimal spacings for the recovery of the bone Raman spectra. The spectra from the three

ring/disk spacings were combined into a single dataset and the band target entropy minimization algorithm (BTEM)<sup>17, 34-36</sup> was used with 5 eigenvectors to recover the bone factor. The band targeted in the BTEM algorithm was the phosphate  $\nu_1$  band ca.  $959\text{ cm}^{-1}$ . For validation, the cross-correlation coefficient between the recovered bone factor and the exposed bone measurement was calculated and found to be 0.97. This resulting spectrum is shown in figure 8.3b. This spectrum was then used to calculate the relative bone Raman signal collected by each fiber for the 10 acquisitions. This was accomplished by first combining the transcutaneous spectra from all the rings into a combined dataset. Bone scores were calculated from a regression of the signal detected by each of the collection fibers with respect to the recovered Raman bone spectrum. These bone scores were used as inputs to the tomographic reconstruction in both transmission and reflectance modes. After the Raman tomographic reconstruction was generated, Tecplot 360 (Tecplot, Inc., Bellevue, WA) was used to view the 3-D images.

### **Raman tomographic reconstruction**

The Raman reconstructions were calculated using an adapted reconstruction software toolbox for photon emission imaging (*NIRFAST*) developed at Dartmouth College. The tool box uses a finite element geometrical model to solve a set of coupled diffusion equations. For the tissue phantom data a volumetric mesh that contained 5993 nodes and 28009 tetrahedral elements was generated using netgen.<sup>37</sup> For the canine tibia 627 CT slices of pixel size  $875 \times 874$  were available from the dog leg, with slice increment of 0.0915 mm. Segmentation of the skin and bone tissues was accomplished through the

thresholding and region-growing techniques in the Mimics™ modeling software (Materialise Inc., Ann Arbor MI). The outer surface of the dog tibia created from the segmentation was exported from Mimics™, and used to create a volumetric grid for computation. A uniform volume mesh of resolution 2 mm was created using a 3-D mesh generator;<sup>38</sup> this grid contained 8218 nodes with 40969 tetrahedrons. The tetrahedrons corresponding to the bone region were suitably tagged so that the bone and the background (assumed to be skin) had different optical properties. The absorption and reduced scattering coefficients for these tissues were obtained from published values<sup>39</sup> for the wavelength 785 nm. The coordinates of the sources and detectors relative to the finite element models were labeled. To reconstruct the size, shape, and position of the buried signal a modified iterative version of Newton's method for minimizing the least squares norm of the difference between the measured and the model data was used.<sup>5, 12, 40</sup> Additionally, regularization to stabilize the inversion was used because of the ill-posed and ill-conditioned nature of the problem.

### **Tomographic reconstruction using spatial priors**

This section describes calculations performed by our collaborators, Professor Brian Pogue and Dr. Subhadra Srinivasan (Dartmouth College).

A finite element model of the diffusion approximation, developed for fluorescence imaging, was used in this work. Since both fluorescence and Raman imaging involve emission of light by tissue, the same numerical models are applicable to both. A set of coupled diffusion equations was used to model both the propagation of laser light at the excitation wavelength and the propagation of emitted light that resulted

from target site fluorescence at the emission wavelength <sup>41</sup>. The coupled equations can be written as a function of frequency  $\omega$  and spatial position  $\gamma$  as:

$$-\nabla \cdot D_x(r) \nabla \Phi_x(r, \omega) + \left( \mu_{ax}(r) + \frac{i\omega}{c} \right) \Phi_x(r, \omega) = S_x(r, \omega)$$

$$-\nabla \cdot D_m(r) \nabla \Phi_m(r, \omega) + \left( \mu_{am}(r) + \frac{i\omega}{c} \right) \Phi_m(r, \omega) = S_m(r, \omega)$$

where  $\Phi_x$  and  $\Phi_m$  are the isotropic fluence at the excitation and emission wavelengths, respectively. Subscript  $x$  denotes excitation, and  $m$  denotes emission;  $\mu_{ax}$  is the absorption coefficient at the excitation wavelength,  $D_x$  is the diffusion coefficient at the excitation wavelength and  $S_x$  is the source term at the excitation wavelength. Similarly,  $\mu_{am}$ ,  $D_m$  and  $S_m$  are the absorption coefficient, diffusion coefficient and the source term at the emission wavelength. The source term at the emission wavelength is related to the fluence at the excitation wavelength as:

$$S_m(r, \omega) = \eta \mu_{af}(r) \Phi_x(r, \omega) \frac{1 - i\omega\tau(r)}{1 + \omega^2\tau^2(r)}$$

where  $\eta \mu_{af}$  is the fluorescence yield (Raman yield in this case) and  $\tau$  is the fluorescence lifetime. The implementation details of this model for fluorescence were published previously.<sup>40</sup>

The inverse problem involves recovering images of Raman yield given measurements of the emission field at the boundary of the imaging domain. A modified Newton's method was used for this purpose, and, using a Taylor series approximation, the equation for update in the source term  $\partial\gamma$  can be given as:

$$\partial\gamma = [\mathfrak{J}^T \mathfrak{J}]^{-1} \mathfrak{J}^T \partial\Phi$$

where  $\partial\Phi$  refers to the change in the emission field sampled at the detector locations on the boundary and the calculated field at the same locations using the forward solver.  $\mathfrak{J}$  is the Jacobian, the matrix containing the sensitivity of the boundary data to a change in  $\gamma$  and

$$\gamma = \eta\mu_{af} \frac{1}{1 + \omega^2\tau^2}$$

Using this procedure, 3D estimates of the Raman yield were reconstructed. To implement the spatial information from the CT images, a matrix transformation was applied to the Jacobian so that the recovered  $\partial\gamma$  then contained homogeneous updates for the specified tissue types from CT. Details of this transformation can be found in Dehghani *et al.*<sup>42</sup>

The intrinsic optical properties at the emission and excitation wavelengths were assumed to be known in this work and were obtained from literature values for canine limb.<sup>39</sup> The ring source configuration for the reflectance mode was modeled by a finite set of discrete sources, and an additive combination of the field generated by each of the sources was used to obtain the fluence distribution from the excitation ring. Similarly, for the implementation of the line source used in the transmission mode, a finite set of discrete sources was used in an additive manner.

Data calibration of the experimental Raman measurements was performed using the measurements from the tissue phantom with 0.5% Intralipid®, denoted as the reference data set. Measurements were simulated assuming known optical properties for the 0.5% Intralipid® phantom, and the average difference between the experimental and simulated data was used as a scaling factor in all reconstructions to compensate for

model-data misfits. This average scaling factor was independent of the spatial heterogeneity present in the domain and presented a feasible way for data calibration.

## **Results and Discussion**

### **Tissue phantom**

The Raman signal for Teflon® obtained from the 0% Intralipid® and 1% Intralipid® tissue phantoms are shown in figure 8.4a. The 0% Intralipid® tissue phantom was a control that exhibited no light scattering. The highest Teflon® signal is localized in the center of the collection field of view over the true position of the sphere. As the illumination rings increase to a diameter that is larger than the diameter of the sphere, no Teflon® signal is observed because the system is not light scattering. The 1% Intralipid® tissue phantom is highly light scattering and as a result the highest Teflon® signal is not localized in the center of the fiber maps, instead it is distributed throughout the fiber maps for each illumination ring diameter. The Teflon® signals calculated for each fiber were then entered into the reconstruction algorithm. A slice of the reconstruction is shown in figure 8.4b. The shape of the sphere and the x and y positions was accurately recovered. However, the reconstruction was surface weighted and predicts the center of the sphere to be approximately 50% higher than the true location of the sphere. Similar surface weighting problems have been observed with backscattered probe configurations in fluorescence tomography as well.<sup>43</sup> Even with this limitation, these results demonstrate that diffuse Raman tomography is feasible.

## **Canine tibia**

Using data obtained with the ring/disk probe, a score plot was calculated for each fiber using the recovered bone factor. This score plot is shown in figure 8.5a. The score for each fiber was entered into the reconstruction algorithm and a slice from the resulting reconstruction is shown in figure 8.5b. Though the highest Raman bone signal is coincident with the actual position of the bone, the reconstruction calculates a large portion of the Raman bone signal to be protruding through the skin, which is not the case. This is likely because of the surface weighting effect of the backscattered probe configuration.

To obtain better results we reconfigured our instrumentation to an 180° transmission based system. In the DOT literature it is apparent that transmission probes yield better results than backscattered probes for deep tissue tomographic measurements.<sup>43, 44</sup> Using the previously recovered bone factor, a score plot was calculated for spectral data acquired with the transmission probe (figure 8.6a). There is much more variation in the bone signal detected for each fiber. The score for each fiber was entered into the reconstruction algorithm. The resulting reconstruction is shown in figure 8.6b. The reconstructed bone signal is positioned over an area on the model where bone is truly located. The shape of the bone is not reconstructed perfectly, most likely because projections were not taken 360° around the limb.

## **Reconstruction using Spatial Priors**

### **Tissue phantom**

The experimental measurements from the tissue phantom with 1% Intralipid® background were calibrated and used for reconstructing estimates of the Raman yield from the background and the Teflon® inclusion. A volumetric description of the phantom, generated using NETGEN,<sup>37</sup> contained 5993 nodes and 28009 tetrahedral elements and was used to find approximate solutions to the coupled diffusion equations. A cross-section of the estimated Raman yield from the reconstructed volume is shown in figure 8.7, where the yield values were scaled to produce a minimum of 1.0. The estimates of Raman yield showed a contrast of 460:1 between the Teflon® inclusion and the background agar/Intralipid® gel. The contrast for these estimates, which were reconstructed with prior knowledge of the spatial location of the inclusion, was much higher than for estimates reconstructed without spatial priors, where the contrast was only 7.4:1.<sup>45</sup> The use of spatial priors in the image reconstruction allowed us (Pogue and Srinivasan) to reconstruct Raman signal due to the Teflon® sphere in the expected location. The reconstruction algorithm converged in 6 iterations, requiring a computational time of 26 minutes on a standard Dell computer with a 2-GHz processor. These image-guided estimates from the tissue phantom illustrate the ability to provide localized Raman spectroscopic values for the background gel and the Teflon® inclusion, as well as to indicate the differences in their chemical composition non-invasively.

### **Canine tibia**

A geometric description of the canine tibia was obtained using image segmentation of the CT images. To define the boundaries between bone and surrounding tissues, the CT images were segmented based on thresholding and region-growing



algorithms using a commercial imaging software package (Mimics<sup>TM</sup>, Materialise, Inc.).<sup>46</sup> A view of the CT image is shown in Figure 8.8a. These segmented tissues were used to create a surface rendering of the canine limb (Figure 8.8b). Using the surface mesh as a starting point, we created a volumetric grid for the limb with Spmesh, an in-house 3D mesh generator.<sup>47</sup> The mesh, which contained 8218 nodes and 40969 tetrahedral elements, was delineated into different materials corresponding to bone and skin using the image segmentations, and each material was labeled with the suitable optical properties.<sup>39</sup> The prepared mesh was used to find image-guided estimates of Raman yield from bone and skin.

The calibrated Raman datasets from both geometries were used independently for the recovery of image-guided estimates of Raman yield values from the bone and the skin. The reconstruction algorithm converged in 5 iterations using reflectance data (computation time = 38.4 min) and in 12 iterations using transmission data (computation time = 94.6 min). The IG-RS estimates were scaled to produce a minimum of 1.0, and these values were used to compare the two system geometries (Figure 8.9). The image-guided estimates of Raman yield from bone were much lower when using data from the reflectance geometry with a contrast of 1.4:1 than when using data from the transmission geometry with a contrast of 145:1. The reflectance values are likely lower, because Raman signal originating from deeper layers is not sufficiently collected in back-reflectance measurements that emphasize Raman signals arising from near the surface. The image-guided estimates from bone and skin in the transmission measurements indicate that we can obtain a contrast between the bone and background of more than 100-fold with this technique.

## Conclusions

The availability of high-efficiency fiber-optic probes and systems have radically improved the use of Raman spectroscopy in clinical settings; an increasing number of research studies are evaluating molecular and biochemical contrast mechanisms with origins in Raman scattering and vibrational spectroscopy.<sup>24,48</sup> Raman spectroscopy is a promising technique, because it has known biochemical specificity that can be attributed to the spectral constituents of materials/tissues<sup>49</sup> and because it provides the possibility for non-invasive, low-cost, spectrally- rich measurements *in vivo*, without the need for contrast agent injection. Our study demonstrates the feasibility of linking Raman measurements with CT imaging of bone and subsequently examining both the structure and biochemical content of intact bone *in vivo*.

This study on Raman tomography indicated that Raman scattering measurements can provide spatial maps of changes in tissue composition. Measurements obtained in transmission mode showed a superior depth penetration as compared to reflectance mode.

These data were consistent with trends observed in fluorescence studies using reflectance mode which have shown that the penetration depth and accurate localization may be limited to a maximum of 10 mm.<sup>43</sup> In previous Raman studies, this depth was quantified at 5 mm for canine tissue.<sup>22</sup> Clearly, the reflectance mode is more useful for characterizing subsurface features within a limited depth of approximately 10 mm. The transmission geometry is more effective for deeper tissue penetration, as our previous study of canine tissue imaging demonstrated.<sup>26</sup>

The key limitation with imaging in the diffuse optical regime, whether using reflectance or transmission geometries, is the spatial resolution, which is limited to the millimeter scale due to high scattering. Increasingly, researchers are investigating multi-modality image-guidance to provide high resolution characterization of tissue, as well as to improve the accuracy of computational models. Towards this end, successful hybrid systems have combined MRI,<sup>50</sup> x rays,<sup>51</sup> and ultrasound<sup>52</sup> with diffuse optical imaging in clinical applications. We have extended this concept of multi-modality image-guidance for providing localized and non-invasive tissue characterization to include Raman spectroscopy. This work, to the best of our knowledge, presents the first image-guided Raman Spectroscopy estimates from biological tissue *in situ*.

As the field of molecular contrast agents and biomarkers expands, the need to increase the contrasts observable from relevant tissue boundaries becomes increasingly important. Typically, measurable and quantifiable contrasts between diseased and normal tissues degrade exponentially when going from *ex-vivo* and *in-vitro* experiments to *in-vivo* data. Hence, an inherently high-contrast imaging technique is particularly attractive for use in molecular tissue characterization. Our results on canine tibia indicate that a hundred-fold contrast can be observed from changes in the biochemical composition of tissue. This technique will have potential applications in observing changes in the mineral and matrix compositions that occur in bone tissue, while providing high resolution via image-guidance from MRI or CT. Future clinically-relevant studies will evaluate the ability of image-guided Raman spectroscopy to monitor biochemical changes occurring from disease.

## Figures

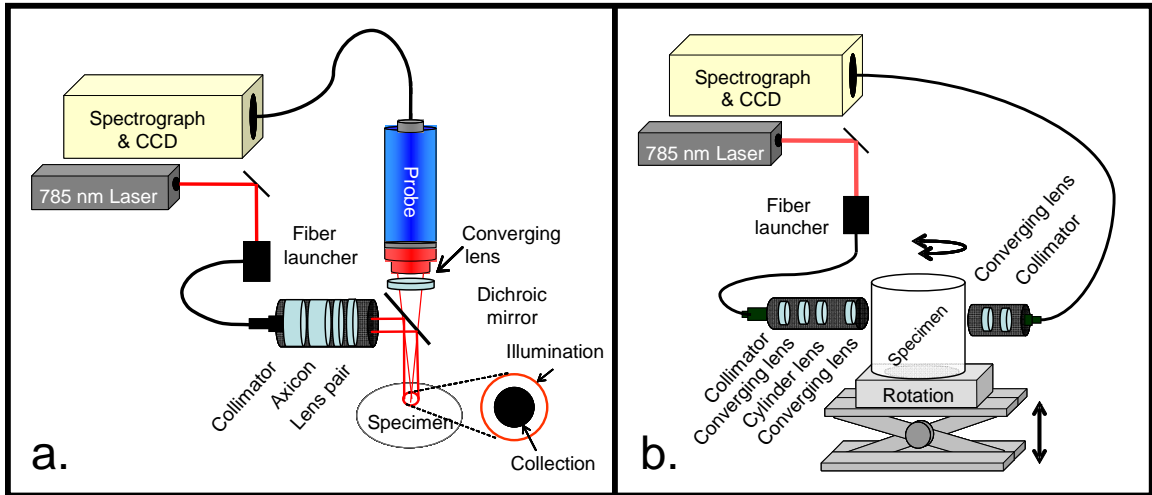


Figure 8.1: (a) Reflectance mode instrumentation for Raman measurements is shown using a ring/disk geometry. The ring diameters can be varied to sample multiple depths for tomographic reconstruction. (b) Transmission mode configuration is shown using a rectangular array of collection fibers at 180 degrees from the line source illumination. Multiple projections across the tissue can be obtained by rotating the sample with respect to the source-collection fiber setup.

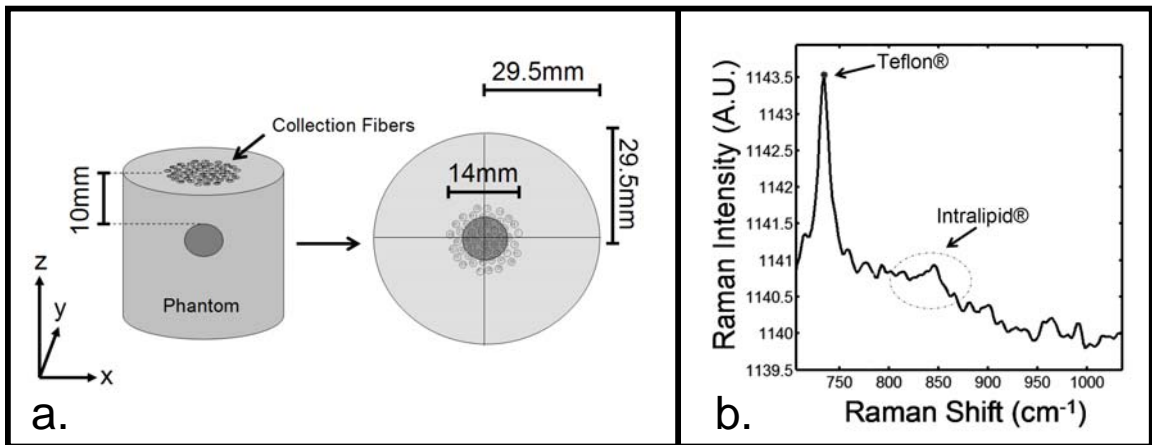


Figure 8.2: (a) Schematic of the tissue phantom (b) Average Raman spectra from one tissue phantom acquisition

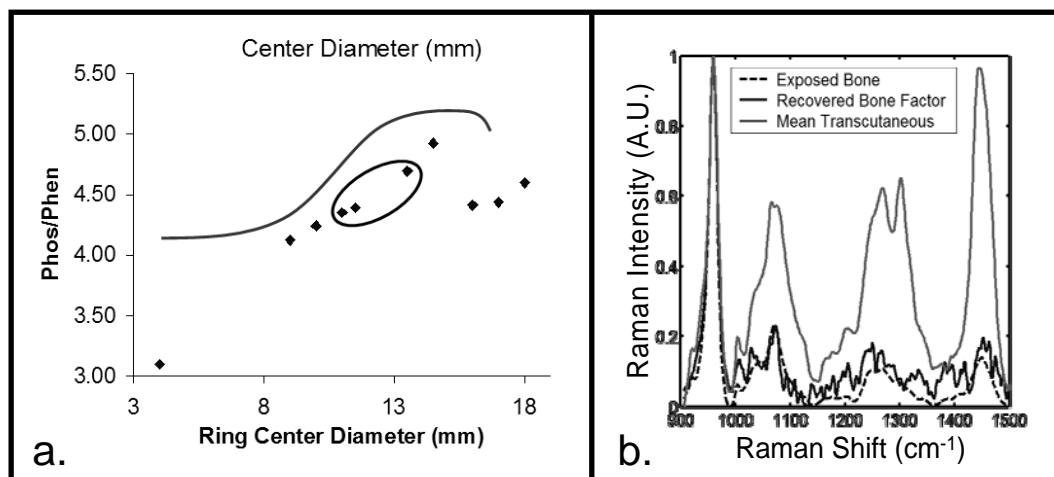


Figure 8.3: (a) Phosphate to phenylalanine ratio for determining the ring/disk separations for optimal signal recovery (b) Mean transcutaneous (gray), recovered bone factor (black), and exposed bone Raman spectrum (dashed)

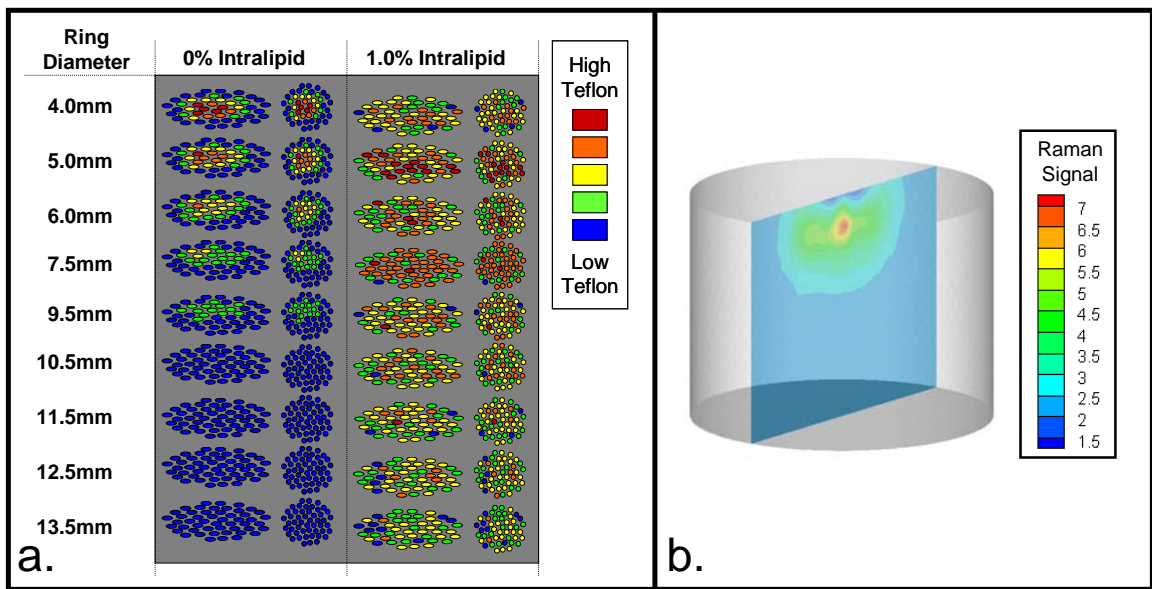


Figure 8.4: (a) five level fiber maps of the Raman Teflon® signal for each fiber (b) slice of the Raman tomographic reconstruction of the Teflon sphere

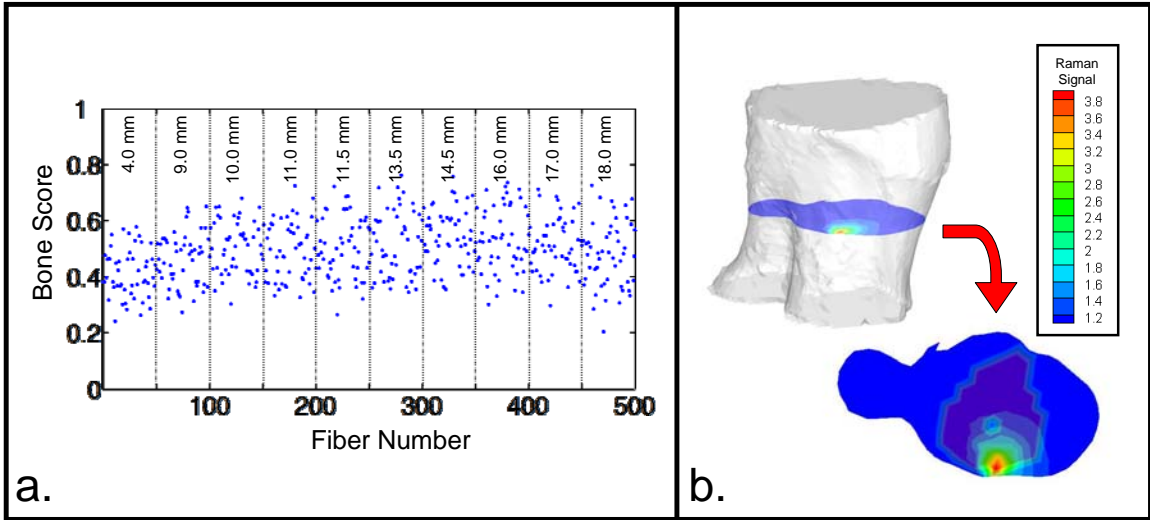


Figure 8.5: (a) ring/disk bone factor score plot (b) slice of the ring/disk Raman tomographic reconstruction of the canine tibia with the true location of the bone outlined in the background (dark red).



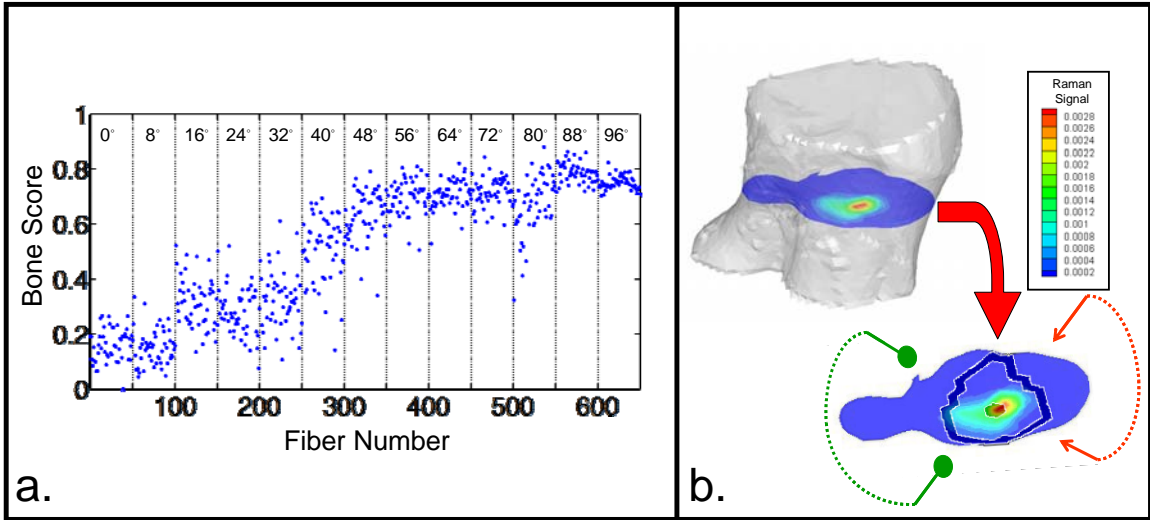


Figure 8.6: (a) transmission probe bone factor score plot (b) slice of the transmission probe Raman tomographic reconstruction of the canine tibia with the true location of the bone outlined in white

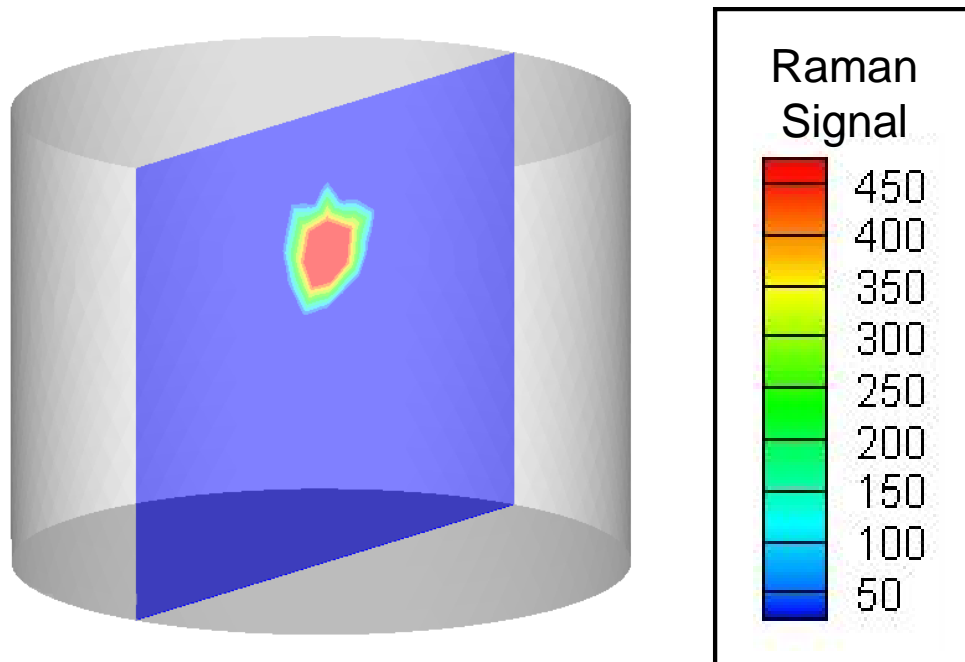


Figure 8.7: Cross-section of the reconstructed volume showing IG-RS estimates of the tissue phantom imaged using the ring/disk probe. The Teflon® inclusion was recovered with a contrast of 460:1 with respect to the background agar/1% Intralipid® gel.

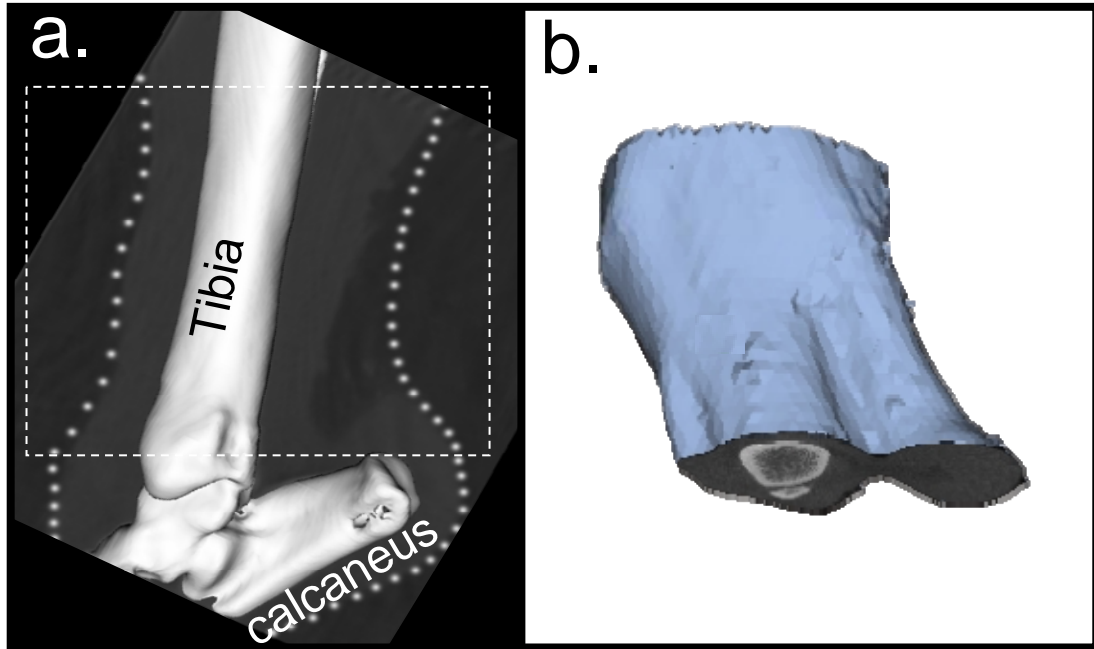


Figure 8.8: Development of mesh for tomographic reconstruction. a) Micro-CT image of canine hind limb section. c) Geometric image of tissues from micro-CT data.

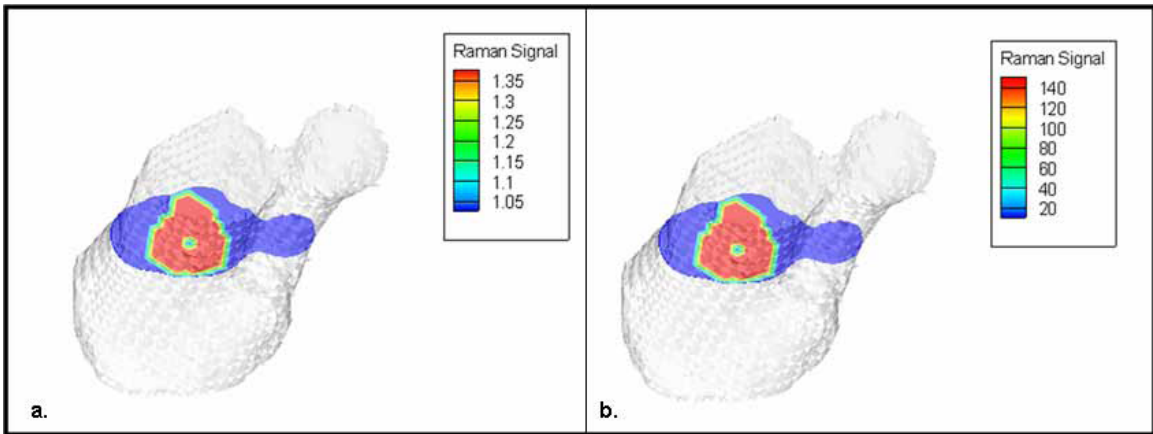


Figure 8.9: A cross-section of the reconstructed IG-RS estimates using (a) reflectance measurements from the ring/disk configuration and (b) transmission measurements using the rectangular array of collection fibers. Recovered contrast between the bone and background skin was more than 100-fold higher using transmission measurements than using reflectance data, as seen from the scale for reconstructed Raman yield.

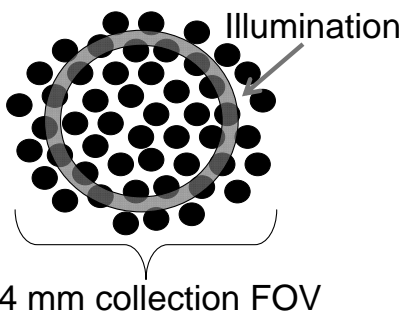
	Ring OD	Ring ID	
Tissue Phantom	5.0	3.0	
	6.0	4.0	
	7.0	5.0	
	10.0	6.0	
	11.0	8.0	
	12.0	9.0	
	13.0	10.0	
	14.0	11.0	
	15.0	12.0	
Canine Tibia	5.0	3.0	
	12.0	6.0	
	15.0	7.0	
	11.0	9.0	
	13.0	10.0	
	15.0	12.0	
	16.0	13.0	
	18.0	14.0	
	19.0	15.0	
	20.0	16.0	

Table 8.1: Illumination ring geometries

## References

1. J. R. Singer, F. A. Grunbaum, P. D. Kohn and J. P. Zubelli, "Image reconstruction of the interior of bodies that diffuse radiation," *Science* 24, 990-993 (1990)
2. S. R. Arridge, P. Zee, M. Cope and D. T. Delpy, "Reconstruction methods for infrared absorption imaging " *Proc. SPIE* 1431, 204-215 (1991)
3. K. D. Paulsen and H. Jiang, "Spatially varying optical property reconstruction using a finite element diffusion equation approximation," *Med. Phys.* 22, 691-701 (1995)
4. M. A. Franceschini, K. T. Moesta, S. Fantini, G. Gaida, E. Gratton, H. Jess, W. W. Mantulin, M. Seeber, P. M. Schlag and M. Kaschke, "Frequency-domain techniques enhance optical mammography: initial clinical results," *Proc. Nat. Acad. Sci. USA* 94(12), 6468-6473 (1997)
5. C. M. Carpenter, B. W. Pogue, S. Jiang, H. Dehghani, X. Wang, K. D. Paulsen, W. A. Wells, J. Forero, C. Kogel, J. B. Weaver, S. P. Poplack and P. A. Kaufman, "Image-guided optical spectroscopy provides molecular-specific information in vivo: MRI-guided spectroscopy of breast cancer hemoglobin, water, and scatterer size," *Opt. Lett.* 32(8), 933-935 (2007)
6. M. Cope and D. T. Delpy, "System for long-term measurement of cerebral blood and tissue oxygenation on newborn infants by near-infrared transillumination," *Med. Biol. Eng. Comp.* 26, 289-294 (1988)
7. B. Chance, Q. Luo, S. Nioka, D. C. Alsop and J. A. Detre, "Optical investigations of physiology: a study of intrinsic and extrinsic biomedical contrast," *Phil. Trans. R. Soc. Lond. B* 352, 707-716 (1997)
8. R. B. Schulz, J. Ripoll and V. Ntziachristos, "Experimental fluorescence tomography of tissue with noncontact measurements," *IEEE Trans. Med. Imaging* 23, 492-500 (2004)
9. S. V. Patwardhan, S. R. Bloch, S. Achilefu and J. P. Culver, "Time-Dependent whole-body fluorescence tomography of probe bio-distribution in mice," *Opt. Express* 13, 2564-2577 (2005)

10. D. Y. Paithankar, A. U. Chen, B. W. Pogue, M. S. Patterson and E. M. Sevick-Muraca, "Imaging of fluorescent yield and lifetime from multiply scattered light reemitted from random media," *Appl. Opt.* 36(10), 2260-2272 (1997)
11. V. Ntziachristos, E. A. Schellenberger, J. Ripoli, D. Yessayan, E. Graves, A. Bogdanov Jr., L. Josephson and R. Weissleder, "Visualization of antitumor treatment by means of a fluorescence molecular tomography with an annexin V-Cy5.5 conjugate," *Proc. Nat. Acad. Sci.* 101(33), 12294-12299 (2004)
12. S. C. Davis, B. W. Pogue, H. Dehghani and K. D. Paulsen, "Contrast-detail analysis characterizing diffuse optical fluorescence tomography image reconstruction," *J. Biomed. Optics* 10(5), 050501 (2005)
13. H. B. Jiang, "Frequency-domain fluorescent diffusion tomography: a finite-element-based algorithm and simulations," *Appl. Opt.* 37, 5337-5343 (1998)
14. D. J. Hawrysz and E. M. Sevick-Muraca, "Developments toward diagnostic breast cancer imaging using nearinfrared optical measurements and fluorescent contrast agents," *Neoplasia* 2, 388-417 (2000)
15. M. J. Eppstein, D. J. Hawrysz, A. Godavarty and E. M. Sevick-Muraca, "Three-dimensional, Bayesian image reconstruction from sparse and noisy data sets: near-infrared fluorescence tomography," *Proc. Natl. Acad. Sci. USA* 99, 9619-9624 (2002)
16. A. B. Milstein, O. Seungseok, K. J. Webb, C. A. Bouman, Q. Zhang, D. A. Boas and R. P. Millane, "Fluorescence optical diffusion tomography," *Appl. Opt.* 42, 3081-3094 (2003)
17. E. Widjaja, N. Crane, T. Chen, M. D. Morris, M. A. Ignelzi Jr. and B. McCreadie, "Band-Target Entropy Minimization (BTEM) Applied to Hyperspectral Raman Image Data," *Appl Spectrosc.* 57(11), 1353-1362 (2003)
18. P. Mayer-Kuckuk and A. L. Boskey, "Molecular imaging promotes progress in orthopedic research," *Bone* 39(5), 965-977 (2006)
19. K. M. Kozloff, A. Carden, C. Bergwitz, A. Forlino, T. E. Uveges, M. D. Morris, J. C. Marini and S. A. Goldstein, "Brittle IV Mouse Model for Osteogenesis Imperfecta IV Demonstrates Postpubertal Adaptations to Improve Whole Bone Strength," *J. Bone Miner. Res.* 19, 614-622 (2004)

20. O. Akkus, F. Adar and M. B. Schaffler, "Age-related changes in physicochemical properties of mineral crystals are related to impaired mechanical function of cortical bone," *Bone* 34(3), 443-453 (2004)
21. B. R. McCreddie, M. D. Morris, T.-C. Chen, D. Sudhaker Rao, W. F. Finney, E. Widjaja and S. A. Goldstein, "Bone tissue compositional differences in women with and without osteoporotic fracture," *Bone* 39(6), 1190-1195 (2006)
22. M. V. Schulmerich, K. A. Dooley, T. M. Vanasse, S. A. Goldstein, M. D. Morris, "Subsurface and Transcutaneous Raman Spectroscopy and Mapping using Concentric Illumination Rings and Collection with a Circular Fiber Optic Array," *Appl. Spectrosc* 61(7), 671-678 (2007)
23. J. C. Carter, S. M. Angel, M. Lawrence-Snyder, J. Scaffidi, R. E. Whipple and J. G. Reynolds, "Standoff detection of high explosive magterials at 50 meters in ambientl light conditions using a small Raman instrument," *Appl. Spectrosc.* 59(6), 769-775 (2005)
24. W. R. Johnson, D. W. Wilson, W. Fink, M. Humayun and G. Bearman, "Snapshot hyperspectral imaging in ophthalmology," *J. Biomed. Optics* 12(1), 014036-014037 (2007)
25. S. P. Poplack, T. D. Tosteson, W. A. Wells, B. W. Pogue, P. M. Meaney, A. Hartov, C. A. Kogel, S. K. Soho, J. J. Gibson and K. D. Paulsen, "Electromagnetic breast imaging: results of a pilot study in women with abnormal mammograms," *Radiology* 243(2), 350-359 (2007)
26. M. V. Schulmerich, S. Srinivasan, J. H. Cole, J. Kreider, K. A. Dooley, S. A. Goldstein, B. W. Pogue and M. D. Morris, "Non-invasive Raman tomographic imaging of canine cortical bone tissue," *J. Biomed. Optics* 13(2), 020501-020503 (2007)
27. M. V. Schulmerich, M. D. Morris, T. M. Vanasse and S. A. Goldstein, "Transcutaneous Raman spectroscopy of bone global sampling and ring/disk fiber optic probes," in *Advanced Biomedical and Clinical Diagnostic Systems V*, pp. 643009-643008, SPIE, San Jose, CA, USA (2007).
28. M. V. Schulmerich, K. A. Dooley, M. D. Morris, T. M. Vanasse and S. A. Goldstein, "Transcutaneous fiber optic Raman spectroscopy of bone using annular illumination and a circular array of collection fibers," *J. Biomed. Optics* 11, 060502 (2006)



29. M. V. Schulmerich, J. H. Cole, K. A. Dooley, J. M. Kreider, S. A. Goldstein, M. D. Morris, "Optical clearing in transcutaneous Raman spectroscopy of bone tissue " J. Biomed. Optics 021108, 1-7 (2008)
30. F. J. Harris, "On the Use of Windows for Harmonic Analysis with the Discrete Fourier Transform," Proc. IEEE 66(1), 51-83 (1978)
31. C. A. Lieber and A. Mahadevan-Jansen, "Automated method for subtraction of fluorescence from biological Raman spectra," Appl. Spectrosc. 57(11), 1363-1367 (2003)
32. D. H. Kohn, N. D. Sahar, S. I. Hong, K. Golcuk and M. D. Morris, "Local Mineral and Matrix Changes Associated with Bone Adaptation and Microdamage," Mater. Res. Soc. Symp. Proc. 898E(L09-03), 1-11 (2006)
33. A. Carden and M. D. Morris, "Application of vibrational spectroscopy to the study of mineralized tissue (review)." J Biomed Opt. 5(3), 259-268 (2000)
34. W. Chew, E. Widjaja and M. Garland, "Band-Target Entropy Minimization (BTEM): An Advanced Method for Recovering Unknown Pure Component Spectra. Application to the FTIR Spectra of Unstable Organometallic Mixtures," Organometallics 21, 1982-1990 (2002)
35. E. Widjaja, C. Li and M. Garland, "Semi-Batch Homogeneous Catalytic In-Situ Spectroscopic Data. FTIR Spectral Reconstructions Using Band-Target Entropy Minimization (BTEM) without Spectral Preconditioning," Organometallics 21, 1991-1997 (2002)
36. E. Widjaja, C. Li, W. Chew and M. Garland, "Band-target entropy minimization. A robust algorithm for pure component spectral recovery. application to complex randomized mixtures of six components," Anal. Chem. 75(17), 4499-4507 (2003)
37. J. Schöberl, "NETGEN- An advancing front 2D/3D-mesh generator based on abstract rules." Computing and Visualization in Science 1(1), 41-52 (1997)
38. Q. Zhang, "Automatic three dimensional mesh generation for anatomically accurate human bodies and organs," Dissertation in Mechanical Engineering, Worcester Polytechnic Institute (1998).

39. G. Alexandrakis, F. R. Rannou and A. F. Chatziioannou, "Tomographic bioluminescence imaging by use of a combined optical-PET (OPET) system: a computer simulation feasibility study," *Phys Med Biol* 50, 4225-4241 (2005)
40. S. C. Davis, H. Dehghani, J. Wang, S. Jiang, B. W. Pogue and K. D. Paulsen, "Image-guided diffuse optical fluorescence tomography implemented with Laplacian-type regularization," *Opt. Express* 15, 4066-4082 (2007)
41. D. Y. Paithankar, A. U. Chen, B. W. Pogue, M. S. Patterson and E. M. Sevick-Muraca, "Imaging of fluorescent yield and lifetime from multiply scattered light reemitted from random media," *Appl. Opt.* 36(10), 2260-2272 (1997)
42. H. Dehghani, B. W. Pogue, J. Shudong, B. Brooksby and K. D. Paulsen, "Three-dimensional optical-tomography: resolution in small-object imaging," *Appl. Opt.* 42(16), 3117-3128 (2003)
43. D. S. Kepshire, S. C. Davis, H. Dehghani, K. D. Paulsen and B. W. Pogue, "Subsurface diffuse optical tomography can localize absorber and fluorescent objects but recovered image sensitivity is nonlinear with depth," *Appl. Opt.* 40(10), 1669-1678 (2007)
44. D. Kepshire, S. Davis, H. Dehghani, K. D. Paulsen and B. W. Pogue, "Challenges in Sub-Surface Fluorescence Diffuse Optical Imaging," *Proc. SPIE* 6434, R1-R10 (2007)
45. S. Srinivasan, M. V. Schulmerich, B. W. Pogue and M. D. Morris, "3-D image-guided raman characterization in a phantom study," in *Biomedical Optics*, p. BWD5, Optical Society of America (2008).
46. I. Materialise, "<http://materialise.com/materialise/view/en/92458-Mimics.html>," Leuven, Belgium.
47. J. Q. Zhang, J. M. Sullivan Jr., H. Ghadyani and D. M. Meyer, "MRI guided 3D mesh generation and registration for biological modeling," *Journal of computing and information science in engineering* 5, 283-290 (2005)
48. M. D. Morris, A. Berger and A. Mahadevan-Jansen, "Infrared and Raman spectroscopy," *J. Biomed. Opt.* 10(3), 031101 (2005)

49. Z. Movasaghi, S. Rehman and I. U. Rehman, "Raman spectroscopy of biological tissues," *Appl. Spectrosc.* 42(5), 493-541 (2007)
50. C. Carpenter, B. W. Pogue, S. Jiang, H. Dehghani, X. Wang, K. D. Paulsen, W. A. Wells, J. Forero, C. Kogel, J. Weaver, S. P. Poplack and P. A. Kaufman, "Image-guided optical spectroscopy provides molecular-specific information in vivo: MRI-guided spectroscopy of breast cancer hemoglobin, water & scatterer Size," *Optics Letters* 32(8), 933-935 (2007)
51. Q. Zhang, T. J. Brukilacchio, A. Li, J. J. Stott, T. Chaves, E. Hillman, T. Wu, M. Chorlton, E. Rafferty, R. H. Moore, D. B. Kopans and D. A. Boas, "Coregistered tomographic x-ray and optical breast imaging: initial results," *J Biomed Optics* 10(2), 024033-0240339 (2005)
52. Q. Zhu, E. B. Cronin, A. A. Currier, H. S. Vine, M. Huang, N. Chen and C. Xu, "Benign versus malignant breast masses: optical differentiation with US-guided optical imaging reconstruction," *Radiology* 237(1), 57-66 (2005)

## **CHAPTER IX**

### **CONCLUSIONS AND FUTURE DIRECTIONS**

Light scattering complicates the non-invasive Raman spectroscopy of tissue and turbid media making it difficult to obtain accurate chemical composition information. We have developed novel fiber optic Raman probes capable of recovering Raman spectra, maps, and tomographic images through several millimeters of overlying tissue. Our work with polymers and tissue phantoms suggest that our methodology may be widely useful. This is a significant breakthrough in analytical chemistry because it allows label-free and non-invasive chemical monitoring of many targets, not just bone, buried inside of light scattering systems, providing information that is unobtainable by other non-invasive methods.

In our first experiments we employed a commercially available fiber-optic probe tested with polymer model systems to recover subsurface spectra and provide maps of the component distribution. The probe was an advance over earlier probe configurations because it utilized global illumination which reduced local power density at the sample or specimen. The subsurface spatial resolution of the probe was governed by the number and size of the fibers in the bundle, the dynamic range of the detector, and ultimately by the inevitable scrambling of spatial information caused the multiple scattering events in the sample or specimen. With the same probe we demonstrated the feasibility of acquiring transcutaneous bone spectra. Despite the laser power being distributed into a

large spot some burning was observed in more heavily pigmented specimens. An additional disadvantage of the global illumination probe was the over-sampling of the surface components caused by illumination and collection over the same region.

These deficiencies led to the development of the ring/disk fiber optic probe. The ring/disk probe had several advantages over the global illumination probe. It provided the benefits of good depth penetration and the ability to supply sufficient laser power to allow acquisition of Raman spectra at moderate collection times. The heat transport of a thin ring is desirable over a spot, since heat dissipation proceeds efficiently in all directions perpendicular to the circumference of the ring. The ring/disk fiber optic probe has good depth resolution properties and preserves subsurface component distribution. Importantly, the ring/disk fiber optic probe samples deep enough to recover bone spectra at least 5 mm below skin and tendons of animal tissue. The data suggests that bone Raman measurements in human subjects are feasible at the distal radius and other sites that are important for prediction of osteoporotic fragility fracture susceptibility. Though the ring/disk probe proved transcutaneous Raman measurement of bone on large animal's feasible, it was less successful on smaller animals.

In a later study we used a line-focused probe suitable for transcutaneous bone measurements on mice to demonstrate the simple ancillary technique of optical clearing to improve the signal-to-noise ratio of transcutaneously measured bone Raman spectra. After further probe development the performance of the line-focused probe was improved and later evaluated *in vivo*. The results obtained using the line/disk probe demonstrates that the configuration is suitable for precise and accurate transcutaneous Raman spectroscopy of murine bone tissue *in vivo*. The configuration distributes the laser power

to prevent thermal damage and provides some spatial separation between the illuminated region and some of the collection fibers.

In these studies, validation of the recovered bone factor was limited to evaluating the averaged exposed bone spectra over the general region of collection. Though this approach is reasonable, it is preferred to have more accurate knowledge of the exact origin of the observed Raman spectra. *A priori* knowledge of the bone architecture measured independently by micro-computed tomography or magnetic resonance imaging, would allow Raman tomographic reconstruction,<sup>1,2</sup> which would in turn provide a more accurate definition of the regions of exposed bone for validation of our transcutaneous measurements.

In the final set of experiments described in this dissertation we demonstrate non-invasive diffuse Raman tomography for the first time. Using both tissue phantoms and an excised canine limb we reconstructed the size, shape, and position of the buried targets. Both back-scattered and transmission based Raman probes were tested. The back-scattered probe configuration was found to have surface-weighting limitations, while the transmission probe was found to be better suited for Raman tomographic measurements. By combining the chemical information obtained by Raman measurements with spatial information from computed tomography we were able to significantly improve the signal-to-noise and accuracy of the Raman tomographic reconstruction. Future clinically relevant studies should evaluate the ability of image-guided Raman spectroscopy to monitor biochemical changes occurring from bone diseases, such as osteoporosis.

Subsurface (and transcutaneous) Raman spectroscopy, imaging, and tomography are attracting increasing interest. Though the technology is still in its infancy, in only two years a wide variety of applications have emerged. Other non-bone related near-term biomedical applications include cancer diagnostics and monitoring arterial plaques.<sup>3</sup> Non-biomedical applications where feasibility has been demonstrated include security screening for the presence of illegal substances, quality control in pharmaceuticals, and active pharmaceutical ingredient (API) authentication.<sup>4-8</sup> The future for non-invasive spectroscopy, imaging, and tomography in turbid media is bright.

## References

1. M. V. Schulmerich, S. Srinivasan, J. Kreider, J. H. Cole, K. A. Dooley, S. A. Goldstein, B. W. Pogue and M. D. Morris, "Raman tomography of tissue phantoms and bone tissue," in *Biomedical Optical Spectroscopy*, pp. 68530V-68537, Proc. SPIE, San Jose, CA, USA (2008).
2. M. V. Schulmerich, S. Srinivasan, J. H. Cole, J. Kreider, K. A. Dooley, S. A. Goldstein, B. W. Pogue and M. D. Morris, "Non-invasive Raman tomographic imaging of canine cortical bone tissue," *J. Biomed. Optics* 13, 020506 (2008)
3. P. Matousek and N. Stone, "Prospects for the diagnosis of breast cancer by noninvasive probing of calcifications using transmission Raman spectroscopy," *J. Biomed. Optics* 12(2), 024008-024008 (2007)
4. P. Matousek and A. W. Parker, "Non-invasive probing of pharmaceutical capsules using transmission Raman spectroscopy," *J. Raman Spectrosc.* 38(5), 563-567 (2007)
5. P. Matousek and A. W. Parker, "Bulk Raman analysis of pharmaceutical tablets," *Appl. Spectrosc.* 60(12), 1353-1357 (2006)
6. P. Matousek, "Deep non-invasive Raman spectroscopy of living tissue and powders," *Chem. Soc. Rev.* 36(8), 1292-1304 (2007)
7. C. Eliasson and P. Matousek, "Noninvasive Authentication of Pharmaceutical Products through Packaging Using Spatially Offset Raman Spectroscopy," *Anal. Chem.* 79(4), 1696-1701 (2007)
8. C. Eliasson, N. Macleod and P. Matousek, "Non-invasive detection of concealed liquid explosives using laser spectroscopy," *Anal. Chem.* 79 (21), 8185 -8189 (2007)



## APPENDIX 1

### PUBLICATIONS

1. Schulmerich, Matthew V.; Finney, William F.; Fredricks, Richard A.; Morris, Michael D. **Subsurface Raman Spectroscopy and Mapping using a Globally Illuminated non-confocal Fiber Optic Array Probe in the Presence of Raman Photon Migration.** *Appl. Spectrosc.* (2006), 60(2), 109-114. (chapter II)
2. Schulmerich, Matthew V.; Finney, William F.; Popescu, Victoria; Morris, Michael D.; Vanasse, Thomas M; Goldstein, Steven A. **Transcutaneous Raman Spectroscopy using a non-confocal Fiber Optic Array Probe.** *Proc. SPIE* (2006), 6093, O1-O7. (chapter III)
3. Schulmerich, Matthew V.; Dooley Katherine A.; Morris, Michael D.; Vanasse, Thomas M; Goldstein, Steven A. **Transcutaneous Fiber Optic Raman Spectroscopy of Bone Using Annular Illumination and a Circular Array of Collection Fibers.** *J. Biomed. Optics* (2006), 11(6), 060502. (chapter IV)
4. Schulmerich, Matthew V.; Vanasse, Thomas M; Goldstein, Steven A.; Morris, Michael D. **Transcutaneous Raman Spectroscopy of Bone: Global Sampling and Ring/Disk Fiber Optic Probes.** *Proc. SPIE* (2007), 6430, 643009\_1-8. (chapter IV)
5. Schulmerich, Matthew V.; Dooley, Kathryn A.; Vanasse, Thomas M.; Goldstein, Steven A; Morris, Michael D. **Subsurface and Transcutaneous Raman Spectroscopy and Mapping using Concentric Illumination Rings and Collection with a Circular Fiber Optic Array.** *Appl. Spectrosc.* (2007), 61(7), 671-678. (chapter V)
6. Schulmerich, Matthew V.; Cole, Jacqueline H.; Dooley, Kathryn A.; Kreider, Jaclynn M.; Goldstein, Steven A.; Morris, Michael D. **Optical clearing in transcutaneous Raman spectroscopy of murine cortical bone tissue.** *J. Biomed. Optics* (2008), 13(2), 021108. (chapter VI)
7. Schulmerich, Matthew V.; Srinivasan, Subhadra; Cole, Jacqueline H.; Kreider, Jaclynn M.; Dooley, Kathryn A.; Goldstein, Steven A.; Pogue, Brian W.; Morris, Michael D.; **Raman Tomography in tissue phantoms and tissue.** *Proc. SPIE* (2008), 6853V ,1-7. (chapter VIII)

8. Schulmerich, Matthew V.; Srinivasan, Subhadra; Cole, Jacqueline H.; Kreider, Jaclynn M.; Dooley, Kathryn A.; Goldstein, Steven A.; Pogue, Brian W.; Morris, Michael D.; **Non-invasive Raman tomographic imaging of canine cortical bone tissue.** *J. Biomed. Optics* (2008), 13(2), 020506. (chapter VIII)
9. Morris, Michael D.; Schulmerich, Matthew V.; Dooley, Kathryn A.; Esmonde-White, Karen A.; **Vibrational Spectroscopic Imaging of Hard Tissue.** *Book chapter for Salzer Siesler (Eds.): Infrared and Spectroscopic Imaging*, Wiley-VCH, *in press*
10. Srinivasan, Subhadra; Schulmerich, Matthew V. Cole, Jacqueline H.; Kreider, Jaclynn M.; Dooley, Kathryn A.; Goldstein, Steven A.; Pogue, Brian W.; Morris, Michael D.; **Image-guided Raman Spectroscopic Recovery of Canine Cortical Bone Contrast *In Situ*.** *Opt. Express* (2008), 16(16) 12190-12200. (chapter VIII)
11. Schulmerich, Matthew V.; Cole, Jacqueline H.; Kreider, Jaclynn M.; Esmonde-White, Francis; Dooley, Kathryn A.; Goldstein, Steven A.; Morris, Michael D. **Transcutaneous Raman spectroscopy of murine bone tissue *In Vivo*.** *Appl. Spectrosc.*, *submitted* (chapter VII)

## APPENDIX 2

### MATLAB SCRIPTS AND FUNCTIONS

% This script outlines the general approach taken to recover a subsurface or transcutaneous spectral factor

```
dir % display director
fileroot=input('Please input sacked file root name: ','s'); % define the spectral dataset
numframes=1; % all measurements consisted of a single frame
load cm; % load the wavenumber shift
Lowerlimit=605 % define the spectral region of interest (lower limit)
Upperlimit=1600; %define the spectral region of interest (Upper limit)
L=Interp1(cm,1:1024,Lowerlimit,'nearest'); % interpolate wavenumber to pixels
Up=Interp1(cm,1:1024,Upperlimit,'nearest'); % interpolate wavenumber to pixels
dat=andor([fileroot '.asc'],numframes); %load spectral dataset

% below define spectral region on the ccd
serialoffset=1 + 0;
serialsize=-1 + 1024;
paralleloffset=1 + 0;
parallelsized=-1 + 256;
prange=paralleloffset+parallelsized;
srange=serialoffset+serialsize;numframes=size(dat,2)/(parallelsized+1);

unspikes % automated program for removing spikes in the dataset
load dark % load data time dark file
darksub; % dark file correction on dataset
load white; % load white light file
whitecorr; % white light correction on the dataset
load fitwidth; % load slit width curvature file
remvcrv; % remove slit width curvature
trans=[]; % initiate a variable
load peaksb; % this is a file that contains the central pixels that correspond to each of the
fibers position relative to the ccd

% double check to make sure 50 fiber positions are in peaksb
[fiber,fibers]=size(peaksb);
```

```

if fibers~=50
display('You have entered in more or less than fifty fibers')
break
end

% select three pixels for each fiber and combine pixels to improve signal to noise
newdatb1=dat(:,peaksb);
peaksa=peaksb-1;
newdata1=dat(:,peaksa);
peaksc=peaksb+1;
newdatc1=dat(:,peaksc);
trans=(newdata1+newdatb1+newdatc1); % dataset consists of 50 spectra

% truncate and standardize the 50 spectra
for d=1: size(trans,2);
trans(:,d)=(trans(345:744,d)-(mean(trans(345:744,d))))/std(trans(345:744,d));
end

% next we choose a base-lining method based on the background of the data. All
base-lining procedures were a form of a weighted least-squares polynomial fit to the
fluorescence background signal and then a subtraction of that polynomial from the data
set. The order of the polynomial usually varied from a 3rd to a 7th and was independently
selected for the spectrum collected by each fiber. Below are the three scripts used:

% iterative base-lining procedure based on:
J. Zhao et. al. Automated Autofluorescence Background Subtraction Algorithm for
Biomedical Raman Spectroscopy, Appl. Spectrosc. (2007), 61(11) 1225-1232
for m=1:size(trans,2);[data(:,m),baseline]=giftsv3(trans(:,m)+5,order);end

% or

% iterative base-lining procedure based on:
C. Lieber et. al. Automated Method for Subtraction of Fluorescence from Biological
Raman Spectra, Appl. Spectrosc. (2003), 57(11) 1363-1367
for m=1:size(trans,2);[data(:,m),baseline]=giftsv2(trans(:,m)+5,order);end

% or

% internally written base-lining procedure where points along the spectra suspected not
to be Raman bands are input into the script... a single polynomial is then fit to those
points. The polynomial is then subtracted from the original spectra.

range=[1:40 68:76 110:148 175:240 232:240 280:300 320:350 385:395]; % example
[data,baseline]=polybase(trans+5,range,order);

% normalize the spectra to the phosphate  $\nu_1$  band

```

```

for qq=1:size(trans,2);
    data(phosphate v1,qq)=data(phosphate v1,qq)/max(data(phosphate v1,qq)');
end

dat=data;unspikes_matt;data=dat;clear dat; % despiked the spectra

%% run a number of times and the average result taken as the spectral factor
% random stop and range generator
stop=randperm(9);stop=stop(:,1)*.1;
up=randperm(15);up=up(:,1);
low=randperm(15);low=low(:,1);
[Spectral_Factor,ev]=btem(data,958-low,958+up,40,2.0+stop);

%%BTEM script called above
[Factor,Eigenvectors]=btem(A,LowerlimitBTEM,UpperlimitBTEM,Eigenvectors,thresh)

load cmcut % load the Raman shift
A=A'; % transpose the data
[U S V]=svd(A); % singular value decomposition
V=V'; % transpose
mplot(cmcut,V(1:10,:)); % plot first 10 eigenvectors and inspect
pause
close all

[m,n]=size(A'); % determine size of data

% interpolate wavenumbers to pixels
number_of_pixels=m;
lowerval=Interp1(cmcut,1:number_of_pixels,LowerlimitBTEM,'nearest');
upperval=Interp1(cmcut,1:number_of_pixels,UpperlimitBTEM,'nearest');

% BTEM script
[xopt,f,tim1] = BTEMrev...
(A,U,S,V,1,Eigenvectors,upperval,lowerval,5,[1:number_of_pixels]);

% Fit a polynomial to 'xopt weights' determined by BTEMrev
stop=abs(xopt);
for m=1:size(stop,2);dummy_x(1,m)=m;end;
[P,S,MU]=polyfit(dummy_x,stop,7);
for k=1:size(stop,2);stop_fit(k,1)=polyval(P,dummy_x(k),[],MU);end;

% Stopping criteria finds points outside 2 to 2.9 std outside of average value
Based on E. Widjaja et. al. Band-Target Entropy Minimization Applied to Hyperspectral
Raman Image Data, Appl. Spectrosc. (2003), 57(11) 1353-1362

```

```
Suggested_number_of_EV=  
max(find(xopt>(thresh*std(xopt(:,15:40)))|xopt<(-thresh*std(xopt(:,15:40)))));  
if Suggested_number_of_EV<3;Suggested_number_of_EV=3;end  
  
% Generate output spectra  
[absb,G] = BTEM_plotrev...  
(xopt,A,V,1,Suggested_number_of_EV,upperval,lowerval,5,[1:number_of_pixels]);  
plot(cmcut,absb);
```